

GAS TRACES MEASUREMENT BY PHOTOACOUSTIC SPECTROSCOPY USING HELMHOLTZ RESONATOR-BASED SENSORS

THÈSE N° 4002 (2008)

PRÉSENTÉE LE 18 JANVIER 2008

À LA FACULTÉ DES SCIENCES ET TECHNIQUES DE L'INGÉNIEUR
Laboratoire de nanophotonique et métrologie
SECTION DE GÉNIE ÉLECTRIQUE ET ÉLECTRONIQUE

ÉCOLE POLYTECHNIQUE FÉDÉRALE DE LAUSANNE

POUR L'OBTENTION DU GRADE DE DOCTEUR ÈS SCIENCES

PAR

Mario MATTIELLO

ingénieur électricien diplômé EPF
et de nationalité italienne

acceptée sur proposition du jury:

Prof. J. R. Mosig, président du jury
Dr L. Thévenaz, directeur de thèse
Dr Z. Bozóki, rapporteur
Dr P. Hoffmann, rapporteur
Dr S. Schilt, rapporteur



ÉCOLE POLYTECHNIQUE
FÉDÉRALE DE LAUSANNE

Lausanne, EPFL
2008

Ai miei genitori

Abstract

Photoacoustic spectroscopy is a well-established gas traces optical detection technique, which consists in the generation of an acoustic wave in the investigated gas compound excited by a modulated laser beam, and in the detection of this sound wave with a sensitive microphone. The sensitivity of this technique can be greatly enhanced through the use of acoustic resonators. A wide range of resonant configurations has been developed and reported in the literature in the last decades. Among these, Helmholtz resonators are known for their simplicity of implementation, though with a reduced efficiency. The main goal of this work is to demonstrate that Helmholtz resonators can be successfully applied to photoacoustic spectroscopy, delivering sensitivities in the same order of magnitude as other more common configurations, as well as offering a powerful tool to perform differential measurements.

Two Helmholtz-based sensors are presented within this thesis. The first sensor has been developed for ammonia sensing, taking benefit from the properties of antimonide-based lasers; the final design has been the result of a carefully optimised compromise between high sensitivity, noise reduction, technical constraints, compact size and straightforward use. After several implemented improvements, an ultimate sub-ppm concentration detection limit has been achieved.

The second sensor exploits the intrinsic phase shift existing between the two volumes of a Helmholtz resonator to perform differential measurements. Each of the two volumes of the resonator is filled with a different concentration of the same gas, whereas the exciting laser beam is split in two arms that separately illuminate the volumes, the resulting photoacoustic signal being proportional to the difference between the respective concentrations of the probed gas in the volumes. A particular detection scheme has been implemented to guarantee a linear measurement. The achieved sensitivity is not as high as obtained with the first sensor; nonetheless, the developed sensor offers the possibility to perform measurements that would otherwise require two different sensing devices, resulting in a clear gain in terms of cost and of detection complexity.

Keywords

Photoacoustic spectroscopy, Helmholtz resonators, antimonide laser diode, differential measurements

Version abrégée

La spectroscopie photoacoustique est une technique de détection optique bien établie dans le domaine de la mesure de traces de gaz, qui consiste en la génération d'une onde acoustique dans le mélange gazeux à analyser, excité par un rayon laser, et en la détection de ce son par le biais d'un microphone très sensible. La sensibilité de cette technique peut être fortement améliorée par l'utilisation de résonateurs acoustiques. Une vaste gamme de configurations résonantes a été développée et rapportée dans la littérature scientifique durant les dernières décennies. Parmi celles-ci, les résonateurs de Helmholtz sont connus pour leur simplicité de mise en œuvre, bien que leurs performances ne soient généralement pas considérées comme très efficaces. Le but principal de ce travail est de montrer que les résonateurs de Helmholtz peuvent être utilisés avec succès en spectroscopie photoacoustique, puisque ils démontrent des sensibilités du même ordre de grandeur que d'autres configurations plus classiques, et ils représentent, en outre, un outil puissant pour effectuer des mesures différentielles.

Deux capteurs basés sur les résonateurs de Helmholtz sont présentés dans cette thèse. Le premier a été développé pour la mesure de l'ammoniac, en exploitant les propriétés des lasers à base d'antimoine. Le design final est le résultat d'un judicieux compromis entre grande sensibilité, réduction du bruit, contraintes techniques, dimensions compactes et facilité d'usage. Après l'apport de plusieurs améliorations, une limite de détection inférieure au ppm a été obtenue.

Le deuxième capteur exploite le déphasage intrinsèque qui existe entre les deux volumes d'un résonateur de Helmholtz pour effectuer des mesures différentielles. Chacun des deux volumes est rempli avec une concentration différente du même gaz, alors que le rayon laser est séparé en deux bras qui illuminent chaque volume; le signal photoacoustique qui en résulte est proportionnel à la différence entre les concentrations respectives du gaz à analyser dans chaque volume. Un schéma de détection adapté a été utilisé pour garantir une mesure linéaire. La sensibilité obtenue n'est pas aussi grande que dans le premier cas; cependant, le capteur développé offre la possibilité d'effectuer un type de mesure qui nécessiterait normalement de deux instruments différents, avec un gain considérable en termes de coûts et de complexité de mesure.

Mots-clés

Spectroscopie photoacoustique, résonateurs de Helmholtz, laser à base d'antimoine, mesures différentielles

Remerciements

Ce travail de thèse a été effectué au Laboratoire de Nanophotonique et Métrologie de l'EPFL sous la direction du Dr Luc Thévenaz. Je tiens avant tout à lui exprimer mes profonds sentiments d'amitié et d'estime pour m'avoir accueilli au sein de son groupe de recherche et pour m'avoir accordé sa confiance tout au long de mon parcours scientifique.

Je remercie profondément les membres du jury, Dr Stéphane Schilt, Dr Zoltan Bozóki et Dr Patrick Hoffmann, pour avoir accepté de lire, évaluer et juger ce mémoire. J'adresse un remerciement particulier au Dr Stéphane Schilt, post-doc dans ce laboratoire pendant plusieurs années, qui a guidé mes premiers pas dans la spectroscopie et qui a été une référence continue et toujours disponible pendant toute la durée de mon doctorat.

Mes remerciements s'adressent également à Omnisens (André Bals, Dr Marc Niklès, Florian Sauser, Dr Etienne Rochat) pour avoir financé la première partie de ce projet, ainsi qu'au Dr Marcel Gyger pour les fructueuses collaborations avec l'animalerie de l'EPFL.

Je remercie chaleureusement mes anciens et actuels collègues de bureau Dario Alasia, Jean-Philippe Besson et Sanghoon Chin, qui ont contribué à créer une excellente ambiance de travail au sein du laboratoire, que cela soit autour d'une discussion scientifique, ou d'un souper entre amis, ou encore de l'incontournable café matinal. En particulier, je ne remercierai jamais assez Jean-Philippe Besson pour l'infatigable soutien qu'il m'a apporté pendant la rédaction de ce mémoire et la préparation de l'examen final.

J'aimerais adresser mes remerciements également à Pascal Morel et à Frédo pour leur précieuse aide et savoir-faire, à Danielle Alvarez et Pierrette Paulou pour leur disponibilité continue, à Sébastien Lamy pour avoir réussi à sauver mon ordinateur une semaine avant mon délai de thèse, ainsi qu'à l'entièreté des équipes du NAM, du TCOM et du LMAM, que j'ai cotoyées tout au long de ces cinq dernières années.

Un clin d'oeil va aux deux entités qui m'ont accompagné sur des voies parallèles pendant ce travail, mon groupe de rock Synsòma et mon équipe de foot LUC, qui ont constitué un excellent moyen de défoulement après les longues journées de travail que demande une thèse de doctorat.

J'adresse une pensée particulière à mes amis de longue date Walter, Gianluca, Nora et Evi, qui ne m'ont jamais fait manquer leur soutien moral et leur bonne humeur exceptionnellement contagieuse.

Finalement, je ne pourrais pas oublier de remercier ma famille, et en particulier mes parents, à qui je dédie cette thèse, pour m'avoir longuement, inconditionnellement, constamment encouragé et soutenu depuis le début de mes études.

Contents

1	Introduction	1
	Bibliography	5
2	Photoacoustic spectroscopy	7
2.1	Introduction	7
2.2	Molecular absorption	8
2.2.1	Intensity of absorption lines	9
2.2.2	Shape and width of absorption lines	10
2.3	Photoacoustic signal generation	14
2.3.1	Heat production	15
2.3.2	Generation of the acoustic wave	18
2.4	Acoustic resonators	20
2.4.1	Helmholtz resonators	23
2.4.2	Other photoacoustic detectors	26
	Bibliography	30
3	Helmholtz photoacoustic sensor	35
3.1	Introduction	35
3.2	Desing of the photoacoustic cell	36
3.2.1	Motivation and criteria for cell design	36
3.2.2	Design of the photoacoustic cell	38
3.3	Characterisation of the photoacoustic cell	42
3.3.1	Frequency response and improvements of the cell	42
3.3.2	Noise level	43
3.3.3	Photoacoustic characterisation of the cell	45
3.4	Trace gas detection	51
3.4.1	Laser characteristics	51
3.4.2	Description of the experimental setup	54
3.4.3	Methane detection	55
3.4.4	Ammonia detection	61
	Bibliography	67
4	Differential Helmholtz photoacoustic sensor	71
4.1	Introduction	71
4.2	Design of the differential photoacoustic cell	72
4.2.1	Motivation and criteria for cell design	72
4.2.2	Design of the differential photoacoustic cell	74
4.3	Characterisation of the differential cell	78
4.3.1	Frequency and phase response	78
4.3.2	Influence of the membrane	79

4.3.3	Photoacoustic characterisation of the cell	81
4.3.4	Noise level	82
4.4	Differential measurements	83
4.4.1	Characterisation of the laser sources	83
4.4.2	Description of the experimental setup	88
4.4.3	R - θ and x - y detection schemes	90
4.4.4	Performances of the sensor	91
	Bibliography	93
5	Conclusion	95
A	Differential photoacoustic signal	97
A.1	Influence of the phase shift	97
A.2	In-phase and quadrature components	98
	Nomenclature	103

List of Figures

2.1	Doppler width (HWHM) for CH ₄ , NH ₃ and O ₂	12
2.2	Collision broadening (HWHM) for CH ₄ as a function of pressure	14
2.3	Comparison of Doppler, collisional and Voigt broadenings for O ₂ as a function of pressure	15
2.4	Simulation of PA intensity loss for oxygen sensing in dry and humid air	18
2.5	Hermann von Helmholtz and one of his resonators	24
2.6	Scheme of a Helmholtz resonator and its analogous electrical circuit	24
2.7	Pressure distribution in cylindrical cavities	27
2.8	Multipass configurations	28
2.9	Intracavity configuration using an external cavity laser	29
2.10	Quartz-enhanced configuration	29
3.1	Measured divergence of the laser beam	36
3.2	Scheme of the laser injection in the cell volume	38
3.3	Theoretical dependence of the cell constant as a function of radius and height of the volumes	39
3.4	Theoretical dependence of the cell constant as a function of radius and length of the duct	40
3.5	Theoretical dependence of the resonant frequency as a function of duct and volume dimensions	40
3.6	Three-dimensional and cross-sectional views of the photoacoustic cell	41
3.7	Acoustic response of the cell	43
3.8	Photoacoustic cell setup, including silencers	44
3.9	Acoustic response of the cell with silencers	44
3.10	Acoustic noise as a function of flow rate	45
3.11	Photoacoustic response of the cell	46
3.12	Resonance frequency and photoacoustic signal as a function of duct radius	48
3.13	Resonance frequency and photoacoustic signal as a function of detection volume height	49
3.14	Resonance frequency and photoacoustic signal as a function of excitation volume height	50
3.15	Output power as a function of injection current for laser #1	53
3.16	Output power as a function of injection current for laser #2	53
3.17	Wavelength tuneability of laser #1	54
3.18	Wavelength tuneability of laser #2	54

3.19	Scheme of the experimental setup	55
3.20	Picture of the experimental setup	56
3.21	Methane spectrum measured with square current modulation	56
3.22	Square and ramp modulation currents	57
3.23	Methane spectrum measured with ramp current modulation	58
3.24	Photoacoustic signal as a function of methane concentration using a ramp modulation	59
3.25	Scan of the probed methane absorption line using WM and $2f$ detection	60
3.26	Photoacoustic signal as a function of methane concentration using WM and $2f$ detection	60
3.27	Ammonia spectrum measured with square current modulation	62
3.28	Photoacoustic signal as a function of current modulation depth	62
3.29	Scan of the ammonia absorption line in stainless steel and golden coated cells	63
3.30	Response time of the PA cell measured in different conditions	64
3.31	Photoacoustic signal as a function of ammonia concentration	65
4.1	Scheme of the differential resonator	73
4.2	Electrical analogy of a Helmholtz resonator whose duct has a volume and a surface not negligible compared to the volumes dimensions	75
4.3	Theoretical dependence of the cell constant and of the resonant frequency as a function of duct dimensions	76
4.4	Theoretical dependence of the cell constant and of the resonant frequency as a function of volume dimensions	77
4.5	Silver-coated window located at volumes extremities	77
4.6	Differential photoacoustic cell setup	78
4.7	Simulation of the frequency and phase behaviour of the differential cell	79
4.8	Measured frequency and phase acoustic behaviour of the differential cell without membrane	80
4.9	Measured frequency and phase acoustic behaviour of the differential cell with membrane	81
4.10	Measured frequency and phase photoacoustic behaviour of the differential cell with membrane	82
4.11	Acoustic noise as a function of flow rate	83
4.12	Output power of the VCSEL as a function of injection current	84
4.13	Dependence of the VCSEL power on the temperature	85
4.14	Wavelength tuneability of the VCSEL as a function of temperature	85
4.15	Oxygen spectrum measured with the selected VCSEL	86
4.16	Output power of the DFB laser as a function of injection current	87
4.17	Wavelength tuneability of the DFB laser	87
4.18	Methane absorption line measured with the selected DFB laser	87
4.19	Picture of the experimental setup	89
4.20	Scheme of the experimental setup	89
4.21	Photoacoustic signal as a function of the difference between CH_4 concentrations	89

4.22	x component of the photoacoustic signal as a function of the difference between CH_4 concentrations	91
4.23	Evolution of the x component of the oxygen photoacoustic signal as a function of time	92
A.1	Theoretical dependence of the differential photoacoustic signal resulting from two identical gas concentrations as a function of the phase shift	98
A.2	Theoretical dependence of the differential photoacoustic signal as a function of the two volumes contributions	98

List of Tables

2.1	Intensity and frequency of some absorption lines investigated in the frame of this work	11
3.1	Comparison between absorption coefficients between NIR region and 2 - 2.7 μm region for CH_4 , NH_3 , HF and CO	36
3.2	Measured values for resonance frequency and quality factor . . .	46
3.3	Characteristics of the lasers used for trace gas monitoring . . .	55
3.4	Summary of the photoacoustic sensor performances	66
3.5	Comparison of the sensor performances with other typical photoacoustic sensors	66
4.1	Characteristics of some investigated materials for the membrane	74
4.2	Main characteristics of the VCSEL and of the DFB laser	88
4.3	Summary of the differential photoacoustic sensor performances	92

Chapter 1

Introduction

The detection of gases using laser sources is a constantly evolving research domain. The significant progresses achieved in the last decades concerning optical sources, amplifiers, detectors, etc. have decisively turned laser spectroscopy into a very powerful tool to perform gas measurements at trace level. In purpose to better exploit the availability of new optical devices, there is a growing demand for the optimisation of the various detection techniques, as well as for the design of new types of sensors. The main goal of the present work is to describe into details two fully novel configurations of spectroscopic sensors, adapted to the properties of some recently developed laser sources, and each one designed to suit the particular requirements of a different specific application.

Gas monitoring at trace level is widely implemented in several application fields, including atmospheric pollution control [1, 2, 3], industrial processes [4, 5, 6], medical diagnostics [7, 8], life science studies [9, 10], and many others. All these applications require sensitive measurements, with target concentrations ranging from few parts-per-million (ppm) to less than one part-per-billion (ppb), and a good selectivity, in order to perform the detection of one particular gas species among many others, (e.g. a particular pollutant in the atmosphere). Other typical requirements are continuous and *in situ* measurements, short response time and non-modification of the gaseous compound.

Conventional spectroscopic techniques, such as chromatography, mass spectrometry or chemiluminescence, do not fulfill all the listed requirements; they necessitate the extraction of a gas sample prior to laboratory analyses, which results in a long response time and in the impossibility of a continuous monitoring; chemiluminescence, moreover, involves a chemical reaction in the gas mixture, which induces a detrimental modification of the compound.

Laser spectroscopy provides an efficient tool to perform continuous, quasi-real time, highly sensitive and selective detection of several gaseous species without any irreversible modification in the analysed mixture. Sensitivity and selectivity are guaranteed by the use of single-frequency sources, delivering optical powers ranging from few milliwatts or tens of milliwatts (semiconductor lasers, quantum cascade lasers) to hundreds of milliwatts (external cavity lasers, optical parametric oscillators) up to several watts (gas lasers), and showing a linewidth which is usually smaller than a few megahertz, thus much narrower with respect to any typical absorption line at ambient temperature and pressure (in the gigahertz range [11]).

The most interesting spectral region to perform laser spectroscopy is the so-called mid infrared range (MIR, approximately between 2 and 10 μm), as in this region many gas species show their fundamental, and therefore strongest, absorption bands. The near infrared range (NIR, 0.7 - 2 μm) is very interesting as well, despite the lower intensity of the absorption lines, on account of the widespread availability of high quality and affordable cost sources, detectors, amplifiers and several other optical devices from the telecommunications field. On the contrary, the visible (0.4 - 0.7 μm) and ultraviolet (UV, less than 0.4 μm) ranges are not attractive to perform laser spectroscopy, mainly because of the lack of efficient optical sources as wavelength becomes shorter.

Laser spectroscopic techniques are based on the absorption of an incident light beam by the molecules of the probed gas. The transmitted light intensity is usually measured, providing a direct knowledge of the target gas concentration, as far as absorption coefficient and interaction path length are known, which is generally the case. This basic method suffers from a high background signal, as the percentage of absorbed light is usually very small, resulting in a strong dependence of the detection sensitivity on the laser power fluctuations, and finally in a lower signal-to-noise ratio (SNR). Different techniques have been developed to improve the sensing performances; among others, balanced detection [12], which is an efficient way to suppress the offset signal; frequency [13] or wavelength [14] modulation spectroscopy (FMS, WMS), which, in conjunction with a lock-in detection, allow a significant noise reduction; cavity-enhanced techniques such as cavity ring-down spectroscopy (CRDS) [15, 16], which offers extremely long absorption paths due to the high reflectance of the cavity mirrors, and is independent on laser power fluctuations, as a decaying time is measured instead of an optical intensity.

Photoacoustic spectroscopy (PAS) is a completely different technique, delivering an indirect measurement of the optical energy which is absorbed by the target gas. In fact, PAS is a calorimetric method based on the measurement of the local heating produced by the absorption of the light radiation by the probed gas molecules. When the laser light is modulated, the induced heating gives rise to a pressure wave, which can be detected using a sensitive microphone.

The main advantages of photoacoustic sensing can be summarised as follows:

- PAS is sensitive to the absorbed (and not to the transmitted) intensity, so that the measured signal is equal to zero if the gas concentration is null (*zero-background* technique).
- The detection is wavelength-independent, as it is performed using a microphone instead of a photodetector. Hence PAS is particularly convenient in the MIR region, where photodetectors are costly and poorly efficient.
- A very good linear dependence between measured signal and gas concentration is observed over several orders of magnitude.
- Very low detection limits can be reached thanks to suitable acoustic resonant configurations.
- PA sensors can easily be compact, portable and small-sized.

Since photoacoustic spectroscopy is an indirect technique, a calibration, usually performed using certified gas cylinders, is needed to establish a univocal correspondence between PA signal and gas concentration.

The main limiting factor of photoacoustic measurements is the acoustic noise, which directly affects the ultimate detection limit of a sensor; therefore, PA sensors are usually equipped with efficient noise filtering devices.

A key issue in the design of a photoacoustic sensor is the measurement cell. In conventional optical spectroscopy, the cell has the only purpose to avoid mixing the investigated gas compound with the external air, and in some cases to make low pressure measurements possible. When PAS is considered, the cell is usually designed to act as an acoustic resonator, with the purpose to enhance the generated photoacoustic signal [17].

The most common geometry for PA cells is a cylindrical resonator, excited along one of its eigenmodes. This work will focus on another geometrical configuration, known as Helmholtz resonator; Helmholtz resonators are based on a different physical process, since the resonance is generated by an harmonic movement of the whole volume of fluid inside the cell, and no standing waves are observed. The aim of this thesis is to demonstrate that this kind of resonator can offer a very attractive solution in specific applications, and turns out to be well adapted to the characteristics of new types of laser sources.

In this purpose, two different Helmholtz-based photoacoustic sensors are presented, each one developed for a particular application. The first one has been designed to suit recently developed distributed feedback (DFB) anti-monide lasers emitting above $2\ \mu\text{m}$, in order to perform ammonia detection at ppm level. Helmholtz resonators conveniently fit the highly divergent beam delivered by this type of lasers, since their resonance is equally excited in each point of the cell, regardless of the laser beam position and shape.

The second sensor is intended to measure the difference between two concentrations of the same gas; in this case, the peculiar π phase shift existing between the two volumes of a Helmholtz resonator is exploited, resulting in the possibility to develop an intrinsically differential sensor.

Organisation of the work

This work mainly consists in three chapters.

- Chapter 2 addresses the theoretical bases lying behind photoacoustic spectroscopy; a general explanation of molecular absorption principles will be presented, followed by a detailed description of the photoacoustic effect; an overview of the different existing acoustic configurations, with a major accent on Helmholtz resonators, will conclude the chapter.
- Chapter 3 is dedicated to the first developed PA sensor. Details about motivations, design and characterisation of the cell will be provided. Several implemented improvements are illustrated as well. Photoacoustic measurements performed on methane (CH_4) and ammonia (NH_3) will then be presented, followed by a discussion on the performances of the sensor.
- Chapter 4, in turn, will concern the differential PA sensor, according to a similar structure. The peculiar requirements of a differential mea-

surement will be addressed by proposing a different detection scheme, tested on methane and oxygen (O_2), and the resulting performances will be discussed at the end of the chapter.

Finally, an appendix is included to illustrate some theoretical calculations concerning the generation and the detection of the differential photoacoustic signal.

Bibliography

- [1] S. Schilt, L. Thévenaz, M. Niklès, L. Emmenegger, and C. Hügli, “Ammonia monitoring at trace level using photoacoustic spectroscopy in industrial and environmental applications,” *Spectrochim. Acta A* **60**(14), 3259–3268 (2004).
- [2] D. Marinov and M. W. Sigrist, “Monitoring of road-traffic emissions with a mobile photoacoustic system,” *Photochem. Photobiol. Sci.* **2**(7), 774–778 (2003).
- [3] M. Szakáll, Z. Bozóki, A. Mohácsi, A. Varga, and G. Szabó, “Diode laser based photoacoustic water vapor detection system for atmospheric research,” *Appl. Spectrosc.* **58**(7), 792–798 (2004).
- [4] G. Wysocki, A. A. Kosterev, and F. K. Tittel, “Spectroscopic trace-gas sensor with rapidly scanned wavelengths of a pulsed quantum cascade laser for in situ NO monitoring of industrial exhaust systems,” *Appl. Phys. B* **80**(4-5), 617–625 (2005).
- [5] S. A. MacDonald, W. D. Hinsberg, H. R. Wendt, N. J. Clecak, C. G. Willson, and C. D. Snyder, “Airborne contamination of a chemically amplified resist.1. Identification of problem,” *Chem. Mater.* **5**(3), 348–356 (1993).
- [6] J.-P. Besson, S. Schilt, F. Sauser, E. Rochat, P. Hamel, F. Sandoz, M. Niklès, and L. Thévenaz, “Multi-hydrogenated compounds monitoring in optical fibre manufacturing process by photoacoustic spectroscopy,” *Appl. Phys. B* **85**(2-3), 343–348 (2006).
- [7] L. R. Narasimhan, W. Goodman, and C. K. N. Patel, “Correlation of breath ammonia with blood urea nitrogen and creatinine during hemodialysis,” *PNAS* **98**(8), 4617–4621 (2001).
- [8] Y. A. Bakhirkin, A. A. Kosterev, R. F. Curl, F. K. Tittel, D. A. Yarekha, L. Hvozdar, M. Giovannini, and J. Faist, “Sub-ppbv nitric oxide concentration measurements using cw thermoelectrically cooled quantum cascade laser-based integrated cavity output spectroscopy,” *Appl. Phys. B* **82**(1), 149–154 (2006).
- [9] F. G. C. Bijnen, F. J. M. Harren, J. H. P. Hackstein, and J. Reuss, “Intracavity CO laser photoacoustic trace gas detection: cyclic CH₄, H₂O and CO₂ emission by cockroaches and scarab beetles,” *Appl. Opt.* **35**(27), 5357–5368 (1996).
- [10] J.-P. Besson, “Photoacoustic spectroscopy for multi-gas sensing using near infrared lasers,” Ph.D. thesis, Swiss Federal Institute of Technology (2006).
- [11] F. K. Tittel, D. Richter, and A. Fried, “Mid-infrared laser applications in spectroscopy,” in *Solid-State Mid-Infrared Laser Sources*, vol. 89 of *Topics in Applied Physics*, pp. 445–516 (Springer-Verlag, Berlin Heidelberg, 2003).

- [12] G. D. Houser and E. Garmire, “Balanced detection technique to measure small changes in transmission,” *Appl. Opt.* **33**(6), 1059–1062 (1994).
- [13] G. C. Bjorklund, “Frequency-modulation spectroscopy: new method for measuring weak absorptions and dispersions,” *Opt. Lett.* **5**(1), 15–17 (1980).
- [14] F. S. Pavone and M. Inguscio, “Frequency-modulation and wavelength-modulation spectroscopies: comparison of experimental methods using an AlGaAs diode laser,” *Appl. Phys. B* **56**(2), 118–122 (1993).
- [15] A. O’Keefe and D. A. G. Deacon, “Cavity ring-down optical spectrometer for absorption measurements using pulsed laser sources,” *Rev. Sci. Instrum.* **59**(12), 2544–2551 (1988).
- [16] K. K. Lehmann and D. Romanini, “The superposition principle and cavity ring-down spectroscopy,” *Journal of Chemical Physics* **105**(23), 10,263–10,277 (1996).
- [17] A. Miklós, P. Hess, and Z. Bozóki, “Application of acoustic resonators in photoacoustic trace gas analysis and metrology,” *Rev. Sci. Instrum.* **72**(4), 1937–1955 (2001).

Chapter 2

Photoacoustic spectroscopy

The second chapter of this thesis is dedicated to the theory, the physical processes, and the engineering modeling which lie behind photoacoustic spectroscopy.

After a brief historical introduction of the photoacoustic effect, the principles of molecular absorption and the properties of the absorption lines will be addressed.

Subsequently, a detailed description of the photoacoustic effect will be presented in two steps, concerning the heat production and the generation of the acoustic wave.

Finally, a general theory of acoustic resonator is provided, illustrating into details the peculiar case of the Helmholtz resonator configuration, implemented in the two sensors described within this work.

2.1 Introduction

The photoacoustic effect was discovered, back in 1880, by the Scottish scientist Alexander Graham Bell [1], first in solids and then in gases and liquids. While carrying out experiments on hearing devices, he noticed that a periodically interrupted light beam interacting with a solid body produced an audible sound. Yet, the unavailability of efficient light sources and of sound amplifying and detecting devices (Bell used respectively chopped sun light and conventional hearing tubes) had soon damped the initial excitement about the new discovery. As a result, nearly no further experiments on the topic were performed for half a century.

By the end of the 30s, the photoacoustic effect gained a new interest in spectroscopic applications, thanks to the pioneering work of Viengerov [2], who implemented blackbody infrared sources (such as Nernst glowers) and a microphone to perform spectroscopic gas analyses; approximately 40 years later, the use of the newly developed lasers as light sources [3], delivering high-power, monochromatic and collimated beams, initiated of a new era for gas photoacoustic spectroscopy.

A great variety of laser sources, resonating cell arrangements and detection schemes have been investigated since, making photoacoustic spectroscopy a very common and efficient technique to perform extremely sensitive gas measurements, with detection limits reaching values below the ppb level.

2.2 Molecular absorption

Optical spectroscopic techniques are based on the interaction between light radiation and molecules of the investigated substance; this interaction gives rise to three different physical phenomena which can be exploited to perform gas detection: Raman scattering, fluorescence emission, and absorption processes. Each process features a characteristic cross section, expressing the likelihood for the process to take place.

Raman scattering induces a frequency shift in the incident light, due to its interaction with the illuminated molecules; this shift is different for each probed substance, resulting in the possibility to simultaneously detect several species while working at only one wavelength; on the other hand, the scattering cross sections are significantly small, so that the resulting sensitivity is poor compared to other spectroscopic techniques.

Fluorescence consists in the emission of higher wavelength radiations when the investigated substance is irradiated, due to the subsequent deactivation processes of the excited molecules. The selectivity is given by the different emitted wavelengths, directly depending on the typical probed substance, but the cross sections are very small, in the same order of magnitude as for Raman scattering, resulting, like in the previous case, in a poor efficiency.

Absorption processes are sensibly more important compared to both Raman scattering and fluorescence on account of their cross section ranging from 10^{-22} to 10^{-20} cm^2/mol , typically six to eight orders of magnitude larger than the two other cases [4]. Therefore, molecular absorption is usually regarded as the most efficient process to perform optical spectroscopy.

When a given molecule interacts with a light radiation of frequency ν_{nm} , it may absorb the photons energy, moving from an initial energy state E_n to a higher energy state E_m according to the following relation:

$$\tilde{\nu}_{nm} = \frac{\nu_{nm}}{c} = \frac{E_m - E_n}{hc} \quad [\text{cm}^{-1}] \quad (2.1)$$

where $\tilde{\nu}_{nm}$ is the frequency expressed in *wavenumbers*, or inverse centimetres¹ (cm^{-1}), as widely used in the literature on spectroscopy, h is the Planck constant ($6.62 \cdot 10^{-34}$ J·s) and c the speed of light in vacuum ($\sim 3 \cdot 10^8$ m/s).

According to laws of quantum mechanics, there is a discrete number of allowed energy levels for a given molecule; hence, a light wave is absorbed by the irradiated molecule only when its frequency corresponds to the difference between two energy levels of the molecule, giving rise to an *absorption line* at the related wavelength. The whole set of absorption lines constitutes the *absorption spectrum* of the molecule. Except in some particular cases, the spectrum of a molecule is not continuous and the absorption lines are gathered in *bands*, usually indicated with the frequency of the transition (e.g. $\tilde{\nu}_1$, $\tilde{\nu}_2 + \tilde{\nu}_3$, $2\tilde{\nu}_4$, etc.).

Energy E of a molecule is the result of contributions from both nuclei and electrons. Using the Born-Oppenheimer approximation, which consists in considering that movements of electrons and of nuclei are dissociated [5], the total energy can simply be written as the sum of an electronic energy E_e and a nuclear energy E_N ; in a similar way, nuclear energy can be approximated by

¹Equation (2.1) provides a frequency in m^{-1} , hence a further division by 100 is needed to obtain the desired value in cm^{-1} .

the sum of contributions from respective vibrational movements between the different nuclei (E_v) and from global rotational movements of the molecule (E_r), so that the following expression can be established:

$$E = E_e + E_v + E_r \quad [\text{J}] \quad (2.2)$$

Magnitudes of the three contributions are sensibly different. Electronic energy is generally much larger compared to the vibrational and rotational energies, hence the transitions between two electronic energy levels are excited by high frequency radiations, corresponding to wavelengths in the UV or visible range. On the other side, transitions between vibrational or rotational energy levels are excited by longer wavelengths, located, in most cases, along the whole IR range, or even in the microwave range for pure rotational transitions.

The intensity of the interaction between light and molecules is directly related to the electrical dipolar momentum \mathbf{D} , which can also be expressed as the sum of a nuclear (\mathbf{D}_N) and an electronic (\mathbf{D}_e) contributions, the former being much larger than the latter. Nonetheless, when a molecule is constituted by two identical atoms (*homonuclear molecule*, e.g. O_2), the nuclear contribution to electrical dipole momentum is equal to zero, so that vibrational and rotational transitions are forbidden. In this case, only electronic transitions due to the magnetic dipole are active, resulting in a much weaker absorption [6].

2.2.1 Intensity of absorption lines

Absorption lines are characterised by their absorption cross section $\sigma(\tilde{\nu})$, which express the likelihood of a molecule to absorb a radiation; $\sigma(\tilde{\nu})$ is given by the product of the linestrength S times a normalised function $g(\tilde{\nu})$, representing the line shape, which will be discussed in detail in the next subsection:

$$\sigma(\tilde{\nu}) = Sg(\tilde{\nu}) \quad [\text{cm}^2/\text{mol}] \quad (2.3)$$

The cross section is directly linked to the absorption coefficient $\alpha(\tilde{\nu})$ through the density N of the absorbing gas:

$$\alpha(\tilde{\nu}) = N\sigma(\tilde{\nu}) \quad [\text{cm}^{-1}] \quad (2.4)$$

and the absorption coefficient allows to calculate the absorbed light intensity $I_a(\tilde{\nu})$ in a path of length l_{path} when the intensity of the incident light is I_0 , using the Beer-Lambert law:

$$I_a(\tilde{\nu}) = I_0 \left(1 - e^{-\alpha(\tilde{\nu})l_{path}} \right) \quad [\text{W}/\text{cm}^2] \quad (2.5)$$

Equations (2.3) to (2.5) show that the absorbance $\alpha(\tilde{\nu})l_{path}$ of a gas at a given wavelength is directly proportional to the linestrength S of the corresponding transition. The linestrength, in turn, is determined by taking into account the difference of population ($N_n - N_m$) between levels E_n and E_m , and the Einstein coefficient for absorption B_{nm} , which gives the probability of a transition between these two levels:

$$S = \frac{1}{N} \frac{h\tilde{\nu}_{nm}}{c} B_{nm} (N_n - N_m) \quad [\text{cm}^2 \cdot \text{cm}^{-1} / \text{mol}] \quad (2.6)$$

The Einstein coefficient is proportional to the matrix element \mathbf{R}_{nm} of the electrical dipolar momentum \mathbf{D} :

$$B_{nm} = \frac{8\pi^3}{3h^2c} |\mathbf{R}_{nm}|^2 \quad [\text{cm}^2/(\text{J}\cdot\text{s})] \quad (2.7)$$

On the other side, the difference between populations of the two levels is given by the Boltzmann distribution:

$$N_n - N_m = N_n \left[1 - \exp\left(-\frac{hc\tilde{\nu}_{nm}}{kT}\right) \right] \quad [1/\text{cm}^3] \quad (2.8)$$

where k is the Boltzmann constant ($1.38 \cdot 10^{-23}$ J/K) and T the absolute temperature. The population of the lower state N_n is:

$$N_n = \frac{Ng_n}{Q_{int}} \exp\left(-\frac{E_n}{kT}\right) \quad [1/\text{cm}^3] \quad (2.9)$$

with g_n being the degeneracy of the lower state and Q_{int} the total internal partition function, i.e. the sum of all the internal energy states, weighted by their degeneracy, defined as:

$$Q_{int} = \sum_n g_n \exp\left(-\frac{E_n}{kT}\right) \quad [-] \quad (2.10)$$

Merging (2.8) and (2.10) into (2.6), the expression of linestrength S as a function of the temperature T is obtained:

$$S(T) = \frac{h\tilde{\nu}_{nm}}{c} B_{nm} \frac{g_n}{Q_{int}(T)} \exp\left(-\frac{E_n}{kT}\right) \times \left[1 - \exp\left(-\frac{hc\tilde{\nu}_{nm}}{kT}\right) \right] \quad [\text{cm}^2 \cdot \text{cm}^{-1} / \text{mol}] \quad (2.11)$$

Linestrength values at a reference temperature of 296 K can be found in databases such as HITRAN (High-resolution TRANsmission molecular absorption database) [7]; values at different temperature can be calculated using eq. (2.11), as long as partition function $Q_{int}(T)$ is known.

As an example, Table 2.1 reports intensity and frequency of some absorption lines shown by different molecules addressed in the frame of this work.

2.2.2 Shape and width of absorption lines

Although for historical reasons absorption features are commonly referred to as *lines*, they actually show a well determined shape, described by a normalised function $g(\tilde{\nu})$, which has been introduced in the previous subsection:

$$\int_0^{\infty} g(\tilde{\nu}) d\tilde{\nu} = 1 \quad [-] \quad (2.12)$$

The lineshape broadening, generally expressed by its *half width at half maximum* value (HWHM), is indicated as $\Delta\tilde{\nu}$, and results from the contribution of three main processes: natural line broadening, Doppler broadening and collisional broadening. The nature of these processes, as long as their respective significance, contributes to determine the effective profile of a particular absorption line.

	Type of transition	$\tilde{\nu}$ [cm ⁻¹]	λ [nm]	S [cm ² ·cm ⁻¹ /mol]
CH ₄	V-R	4216.473	2371.6	4.15·10 ⁻²¹
NH ₃	V-R	4522.388	2221.2	5.27·10 ⁻²¹
CH ₄	V-R	6057.098	1651.0	1.28·10 ⁻²¹
O ₂	El	13142.58	760.9	8.83 ·10 ⁻²⁴

Table 2.1: Intensity and frequency of some absorption lines investigated in the frame of this work. V-R stands for vibrational-rotational transition, El for electronic transition. $\tilde{\nu}$ is the frequency in cm⁻¹, λ the corresponding wavelength and S the linestrength. Oxygen line, due to a magnetic dipole transition, is more than 2 orders of magnitude lower than the other reported values.

2.2.2.1 Natural line broadening

Natural line broadening $\Delta\tilde{\nu}_{nat}$ is coupled to the broadening ΔE of the excited energy level E_m , due to the Heisenberg uncertainty principle:

$$\tau_{sp} \cdot \Delta E = \tau_{sp} \cdot hc\Delta\tilde{\nu}_{nat} \geq \hbar \quad [\text{J}\cdot\text{s}] \quad (2.13)$$

where \hbar is the reduced Planck constant (equal to $h/2\pi$) and τ_{sp} is the characteristic lifetime of the energy state E_m , corresponding to the time needed for the population N_m of this state to decay to 1/e of its initial value. This lifetime is directly related to the Einstein coefficient for spontaneous emission A_{nm} :

$$\tau_{sp} = \frac{1}{A_{nm}} \quad [\text{s}] \quad (2.14)$$

Einstein coefficients for absorption and for spontaneous emissions are coupled according to the following equation:

$$A_{nm} = 8\pi hc\tilde{\nu}_{nm}^3 B_{nm} = \frac{64\pi^4 \tilde{\nu}_{nm}^3}{3h} |\mathbf{R}_{nm}|^2 \quad [\text{s}^{-1}] \quad (2.15)$$

so that the final expression for natural line broadening is obtained by merging equations (2.13) to (2.15) together:

$$\Delta\tilde{\nu}_{nat} \geq \frac{32\pi^3 \tilde{\nu}_{nm}^3}{3hc} |\mathbf{R}_{nm}|^2 \quad [\text{cm}^{-1}] \quad (2.16)$$

The dependence of $\Delta\tilde{\nu}_{nat}$ on $\tilde{\nu}_{nm}^3$ results in a low ($\sim 10^{-7}$ cm⁻¹, few kilohertz) or even extremely low ($\sim 10^{-14}$ cm⁻¹, i.e. 10⁻⁴ Hz) broadening when vibrational or rotational transitions are respectively considered, hence this process is usually negligible with respect to Doppler and collisional broadenings. In the case of an electronic transition, natural line broadening raises up to values in the order of magnitude of 10⁻³ cm⁻¹ (approximately 30 MHz), thus becoming closer to the other processes, though at atmospheric pressure it can still be neglected in the majority of cases.

Natural line broadening is a homogeneous process, as it affects all the molecules in the same way, and the resulting lineshape can be described by a lorentzian profile.

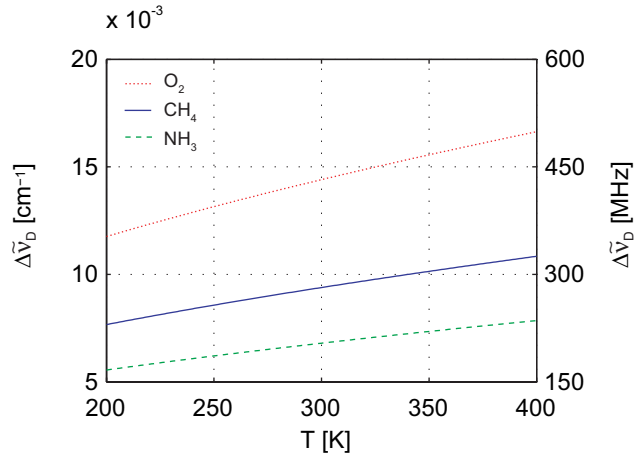


Figure 2.1: Doppler width (HWHM) for CH₄ at 6057.098 cm⁻¹ (1651.0 nm, *solid line*), for NH₃ at 4522.388 cm⁻¹ (2211.2 nm, *dashed line*) and O₂ at 13142.58 cm⁻¹ (760.9 nm, *dotted line*) as a function of temperature.

2.2.2.2 Doppler broadening

The exact frequency of a molecular transition is influenced by the actual velocity v of the molecule with respect to the light beam direction. This relative velocity produces a shift (called Doppler shift) in the transition frequency $\tilde{\nu}$, according to the following equation:

$$\tilde{\nu} = \tilde{\nu}_0 \left(1 \pm \frac{v}{c}\right) \quad [\text{cm}^{-1}] \quad (2.17)$$

given that $\tilde{\nu}_0$ is the transition frequency in a stationary molecule.

Unlike in the case of natural line broadening, the Doppler effect does not concern all the molecules in the same way, as each molecule produces its own shift according to its velocity, thus giving rise to an inhomogeneous process. The resulting lineshape can be described by a Gaussian distribution, and the related characteristic broadening $\Delta\tilde{\nu}_D$ is given by the following relation:

$$\Delta\tilde{\nu}_D = \frac{\tilde{\nu}_0}{c} \sqrt{\frac{2RT \ln 2}{M}} \quad [\text{cm}^{-1}] \quad (2.18)$$

where R is the perfect gas constant (8.3144 J·mol⁻¹K⁻¹), T the gas temperature, and M the molar mass.

Equation (2.18) shows that Doppler broadening depends on the transition frequency, though to a less significant extent with respect to natural broadening, and on the molar mass of the molecule. Fig. 2.1 depicts the calculated dependence of this broadening on temperature in the case of some molecules addressed within this work: CH₄ (at 1651.0 nm), NH₃ (at 2211.2 nm) and O₂ (at 760.9 nm). For a typical molar mass of 20 g/mol, values for $\Delta\tilde{\nu}_D$ at ambient temperature range approximately from 0.005 cm⁻¹ (150 MHz) at 2 μm to 0.02 cm⁻¹ (600 MHz) at 760 nm. Hence, despite its larger molar mass, oxygen suffers from a wider broadening on account of the much higher frequency of its transitions.

2.2.2.3 Collisional broadening

Collisional broadening is produced by the energy exchanges which take place between the different molecules when they collide; it is sometimes also referred to as pressure broadening, as the probability of collisions increases with higher pressure, and it is related to the mean time between collisions τ_{coll} , according to the Heisenberg principle (see eq. (2.13)):

$$\Delta\tilde{\nu}_{coll} = \frac{1}{2\pi\tau_{coll}} \quad [\text{cm}^{-1}] \quad (2.19)$$

Unlike the other broadening processes, collisional broadening is totally independent from transition frequency. The collision process is homogeneous, and the resulting broadening can be described by a lorentzian lineshape whose characteristic width $\Delta\tilde{\nu}_L$ depends linearly on pressure; a less significant influence of the temperature is observed as well:

$$\Delta\tilde{\nu}_L = gp \left(\frac{T_0}{T} \right)^{n_T} \quad [\text{cm}^{-1}] \quad (2.20)$$

where p is the pressure, T_0 is usually fixed at 296 K, n_T is a temperature coefficient usually ranging between 0.5 and 0.8 [7], and g is a broadening coefficient depending on the nature of the surrounding molecules in the specific gas compound. Databases usually provide two coefficients, one for collisions with other molecules of the same species (coefficient of self-broadening, g_{self}) and one for collisions with air molecules (coefficient of air-broadening, g_{air}). The resulting broadening depends on the partial pressure p_{self} of the excited substance in the mixture:

$$\Delta\tilde{\nu}_L = [g_{self}p_{self} + g_{air}(p - p_{self})] \left(\frac{T_0}{T} \right)^{n_T} \quad [\text{cm}^{-1}] \quad (2.21)$$

Collisional broadening at ambient pressure and temperature is usually in the range of 0.1 cm^{-1} (2-3 GHz), thus approximately one order of magnitude higher than Doppler broadening; nonetheless, it can be easily and efficiently reduced by decreasing the operating pressure. Pressure decrease induces a second advantage in terms of cross section: as the product between the cross section peak value σ_{peak} and $\Delta\tilde{\nu}_L$ is fixed in the case of a lorentzian profile, a narrower broadening results in a larger cross section peak value, and eventually in a stronger absorbance:

$$\sigma_{peak} = \frac{S}{\pi\Delta\tilde{\nu}_L} \quad [\text{cm}^2/\text{mol}] \quad (2.22)$$

Pressure dependence of a typical collisional broadening is illustrated in Fig. 2.2 for a methane absorption line, in the case of a pure methane compound and of 5000 ppm of methane in air. The divergence between the two curves has its origin in the difference between the broadening coefficients g_{self} and g_{air} .

2.2.2.4 Voigt profile

As it results from the previous section, collisional broadening at atmospheric pressure and room temperature is larger enough with respect to the other

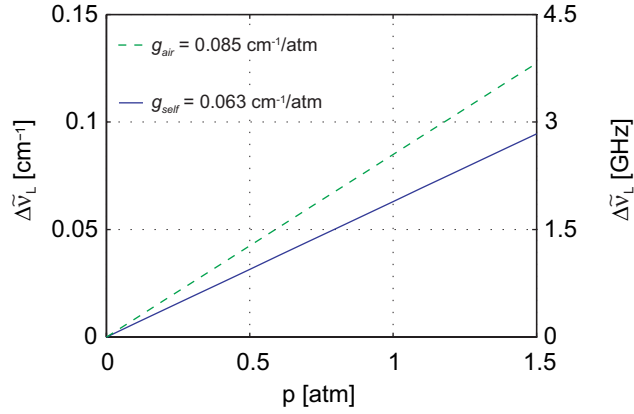


Figure 2.2: Collision broadening (HWHM) for CH_4 at 4216.473 cm^{-1} (2371.6 nm) as a function of pressure, in the case of a pure methane compound (*solid line*) and of 5000 ppm of methane in air (*dashed line*).

processes to make them negligible, so that the absorption lineshape can be efficiently approximated by a lorentzian profile, especially in the case of low frequency transitions. Nevertheless, in order to take into account the effect of Doppler shift, it is common to describe the lineshape by a Voigt profile. The Voigt profile (g_V) results from a convolution between lorentzian (g_L) and gaussian (g_D) distributions, representing respectively the collisional and the Doppler broadening:

$$g_V(\tilde{\nu}) = \int_0^{\infty} g_L(\tilde{\nu}') g_D(\tilde{\nu} - \tilde{\nu}') d\tilde{\nu}' \quad [1/\text{cm}^{-1}] \quad (2.23)$$

The resulting HWHM width $\Delta\tilde{\nu}_V$ is related to Doppler and collisional broadenings through the following approximation, proposed in [8] and showing an accuracy of $\pm 0.02\%$:

$$\Delta\tilde{\nu}_V \approx 0.5346\Delta\tilde{\nu}_L + \sqrt{0.2166\Delta\tilde{\nu}_L^2 + \Delta\tilde{\nu}_D^2} \quad [\text{cm}^{-1}] \quad (2.24)$$

Fig. 2.3 illustrates the Doppler, collisional and Voigt broadenings of the 760.9 nm oxygen transition, calculated for a pure oxygen compound, at a temperature of 296 K and as a function of pressure. The influence of Doppler broadening is clearly visible and becomes more important at lower pressures. At $p = 1 \text{ atm}$, the difference between Voigt and collisional broadenings is approximately $4.1 \cdot 10^{-3} \text{ cm}^{-1}$ ($\sim 120 \text{ MHz}$), resulting in a relative error of 8.3% if the Doppler broadening is neglected.

2.3 Photoacoustic signal generation

Once an absorbing molecule is excited by a light wave to an energy level E_m , it eventually falls down to its initial energy E_n through several processes, including radiation (stimulated or spontaneous emission of a photon), chemical reactions, and non-radiative deactivation, which consists in an energy transfer towards surrounding molecules through collisions [9]. When the latter process

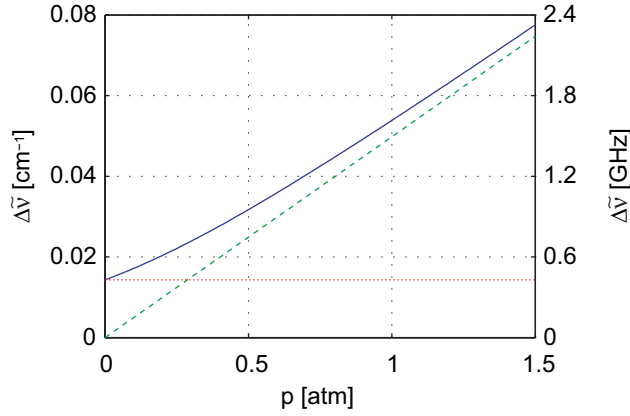


Figure 2.3: Comparison of Doppler (*dotted line*), collisional (*dashed line*) and Voigt (*solid line*) broadenings for pure O₂ at 13142.58 cm⁻¹ (760.9 nm) as a function of pressure. Temperature is 296 K. Neglecting the Doppler broadening results in a relative error of 8.3% at atmospheric pressure, corresponding to 4.1·10⁻³ cm⁻¹ (~ 120 MHz).

is considered, the resulting increase in the kinetic energy of the molecules causes a local heating, and subsequently a thermal expansion in the medium. If the intensity of light radiation is modulated at a given frequency, the induced periodical thermal expansion gives rise to a sound wave of the same frequency. This process takes the name of photoacoustic effect.

Photoacoustic spectroscopy exploits the property that the intensity of the generated wave, under certain conditions, is directly proportional to the number of excited molecules; hence the concentration of the probed substance can be derived from the measurement of the induced pressure variation through a sensitive microphone.

Description of the photoacoustic effect can be divided in a two-steps process; first step consists in determining the local heating induced by the absorbed light radiation, second step concerns the sound wave generation due to the medium thermal expansion. The two steps are detailed in the following sections.

2.3.1 Heat production

Heat production due to light absorption in a molecule can be described by the analysis of the respective populations N_m and $N - N_m$ of the excited and the ground energy levels E_m and E_n [10]. Rate equation for the excited level can be expressed as follows:

$$\frac{dN_m}{dt} = (N - N_m) \sigma \phi - N_m \left(\sigma \phi + \frac{1}{\tau_m} \right) \quad [1/(\text{s} \cdot \text{cm}^3)] \quad (2.25)$$

where σ is the absorption cross section of the transition, ϕ the incident photon flux and τ_m the global lifetime of the excited state, depending on combined contributions from radiative and non-radiative deactivation processes:

$$\tau_m = \frac{1}{\tau_{mr}^{-1} + \tau_{mnr}^{-1}} \quad [\text{s}] \quad (2.26)$$

In typical atmospheric conditions, the radiative lifetime τ_{mr} is much longer than the non-radiative contribution τ_{mnr} (typically between 10^{-1} and 10^{-3} s, and between 10^{-6} and 10^{-9} s [11]), so that τ_m can simply be approximated by its non-radiative component².

The incident excitation rate $\sigma\phi$ is usually small enough to consider that N_m is negligible with respect to N ; hence the rate equation can be approximated by the following expression:

$$\frac{dN_m}{dt} = N\sigma\phi - N_m \frac{1}{\tau_m} \quad [1/(\text{s}\cdot\text{cm}^3)] \quad (2.27)$$

Incident photon flux ϕ in the case of a sine-modulated laser beam can be expressed as:

$$\phi = \phi_0 (1 + e^{j\omega t}) \quad [1/(\text{s}\cdot\text{cm}^2)] \quad (2.28)$$

the two terms within brackets corresponding respectively to the average value and to the modulated component of the light radiation, whereas ω is the modulation angular frequency.

When considering the time-dependent term of the photon flux, which is the only concerned component within the photoacoustic signal generation process, the solution of equation (2.27) is:

$$N_m = \frac{N\phi_0\sigma\tau_m}{\sqrt{1 + (\omega\tau_m)^2}} e^{j(\omega t - \varphi)} \quad [1/\text{cm}^3] \quad (2.29)$$

where $\varphi = \arctan(\omega\tau_m)$ is the phase shift between N_m and ϕ .

The resulting heat production rate H is related to the population of the excited state, to the energy gap of the transition and to the non-radiative component of the level lifetime:

$$H = N_m \frac{hc\Delta\tilde{\nu}}{\tau_{mnr}} \quad [\text{J}/(\text{s}\cdot\text{cm}^3)] \quad (2.30)$$

As in the two-levels used model the lower state corresponds to the ground energy level of the molecule, the quantity $\Delta\tilde{\nu}$ is assumed to be equivalent to the laser frequency $\tilde{\nu}_{las}$. Therefore, taking into account the previously introduced approximation $\tau_m \approx \tau_{mnr}$, the heat production rate becomes:

$$H = N_m \frac{hc\tilde{\nu}_{las}}{\tau_m} \quad [\text{J}/(\text{s}\cdot\text{cm}^3)] \quad (2.31)$$

Time dependence of the heat production rate is obtained combining eq. (2.29) and (2.31):

$$H = H_0 e^{j(\omega t - \varphi)} \quad [\text{J}/(\text{s}\cdot\text{cm}^3)] \quad (2.32)$$

where

$$H_0 = \frac{N\sigma I_0}{\sqrt{1 + (\omega\tau_m)^2}} \quad [\text{J}/(\text{s}\cdot\text{cm}^3)] \quad (2.33)$$

²This approximation is only valid in the case of vibrational and rotational transitions, whereas in the case of electronic transitions radiative component cannot be neglected.

and

$$I_0 = \phi_0 h c \tilde{\nu} l_{as} \quad [\text{W}/\text{cm}^2] \quad (2.34)$$

I_0 being the intensity of the incident beam.

A further simplification is brought in when the product $\omega\tau_m$ is much smaller than 1, which is generally the case when the modulation frequency $f = \omega/(2\pi)$ is in the kilohertz range. Denominator of eq. (2.33) can then be neglected, and magnitude of the heat production rate is simply reduced as follows:

$$H_0 = N\sigma I_0 = \alpha I_0 = \alpha_0 I_0 C_{gas} \quad [\text{J}/(\text{s}\cdot\text{cm}^3)] \quad (2.35)$$

where α_0 is a normalised absorption coefficient calculated for a gas concentration of 1000 ppm and an interaction path of 10 m, while C_{gas} is the effective gas concentration, so that³:

$$\alpha = \alpha_0 C_{gas} \quad [\text{cm}^{-1}] \quad (2.36)$$

In these conditions, medium heating is perfectly linear with probed gas concentration (as long as $\sigma\phi$ is small), as well as being in phase with optical modulated intensity, since φ tends to 0° .

2.3.1.1 Relaxation effects

In some particular cases, the relaxation lifetime τ_m is not short enough to fulfill the condition $\omega\tau_m \ll 1$. The molecular deactivation process is then too slow to be completed within one modulation period of the laser, resulting in a less efficient medium heating (see eq. (2.33)).

The first and more obvious consequence of this phenomenon is that intensity of the generated photoacoustic signal is sensibly weakened, as it linearly depends on the produced heat; a phase lag between PA signal and laser modulation is furthermore obtained [4].

A second, indirect effect of a slow relaxation process can manifest as a parabolic dependence of the photoacoustic signal on the probed gas concentration [12]. This is due to the fact that the efficiency of molecular relaxation does not depend only on the nature of the measured substance M_j , but also on the different components M_k of the buffer gas mixture. In fact, non-radiative relaxation is achieved through collisions with all the surrounding molecules, and the resulting relaxation lifetime is a combination of the characteristic lifetimes corresponding to collisions with each specific molecule:

$$\tau_{mnr}^{-1} = \sum_{k=1}^n C_k \tau_{M_j-M_k}^{-1} \quad [\text{s}^{-1}] \quad (2.37)$$

where $\tau_{M_j-M_k}^{-1}$ is the relaxation rate (the inverse of the relaxation lifetime) of molecule M_j through collisions with molecule M_k , and C_k is the concentration of M_k .

³The normalized absorption coefficient is not calculated for a gas concentration of 100% and an interaction path of 1 cm because the concentration of the probed gas directly influences the collisional line broadening, and hence the cross section peak value, so that eq. (2.36) would provide an unprecise absorption coefficient for low gas concentrations.

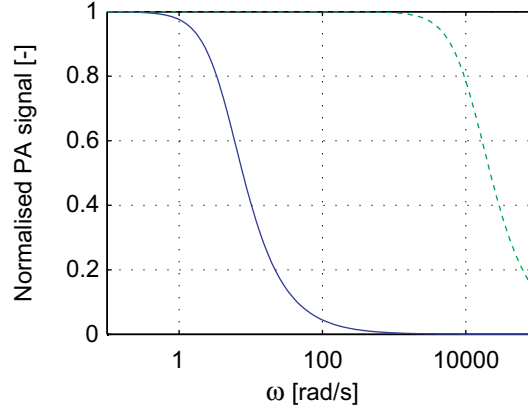


Figure 2.4: Simulation of PA intensity loss for oxygen sensing in dry (*solid line*) and humid (*dashed line*) air. Relaxation lifetime is shortened by a factor of 10^4 .

Eq. (2.37) can be written as the sum of the contribution from collisions with the probed gas itself and of all other contributions:

$$\tau_{mnr}^{-1} = C_j \tau_{M_j - M_j}^{-1} + \tau_{oth}^{-1} \quad [\text{s}^{-1}] \quad (2.38)$$

In the case of a very slow relaxation lifetime, one can assume that $\omega \tau_{mnr} \gg 1$, so that eq. (2.33) becomes:

$$H_0 = \frac{N \sigma I_0}{\omega} \tau_{mnr}^{-1} \quad [\text{J}/(\text{s} \cdot \text{cm}^3)] \quad (2.39)$$

and successively, by introducing eq. (2.38) and by considering $C_j = N/N_{tot}$:

$$H_0 = \frac{N_{tot} \sigma I_0}{\omega} C_j \left(C_j \tau_{M_j - M_j}^{-1} + \tau_{oth}^{-1} \right) \quad [\text{J}/(\text{s} \cdot \text{cm}^3)] \quad (2.40)$$

where the dependence of the PA signal on the gas concentration appears as the sum of a linear and a quadratic term.

One way to reduce the significance of the described negative effects is to add to the investigated gas compound a small percentage of some specific molecules showing the property of catalysing the relaxation processes. Water vapour, for instance, proves to hasten up deactivation of many species [4].

As an example, Fig. 2.4 depicts the calculated relative loss of photoacoustic intensity for oxygen sensing in dry (78% of nitrogen, 21% of oxygen) and humid (same compound, plus 1.15% of water vapour, corresponding to a typical relative humidity of 50% at ambient temperature) air as a function of frequency, according to the relaxation rates values given in [13]. The small percentage of water vapour reduces the relaxation lifetime of oxygen by a factor of 10^4 . This results in a shifted appearance of PA signal intensity loss from an unrealistic value of 0.1 Hz to a more convenient frequency of few hundreds hertz.

2.3.2 Generation of the acoustic wave

The generation of an acoustic signal due to the periodic heating of a medium is a complex physical process concerning several quantities, including density

ρ , pressure p , temperature T and fluid velocity \mathbf{v} . The governing laws are the Navier-Stokes equation, describing the fluid motion, the thermal diffusion equation, the mass-density continuity equation, and a thermodynamic equation of state [14].

The complexity of the problem results in the concrete impossibility to find an exact solution to it, unless some approximations are introduced. The first approximation consists in considering that variations of the concerned physical quantities are small with respect to their absolute values:

$$p(\mathbf{r}, t) = p_0 + p_a(\mathbf{r}, t) \quad [\text{Pa}] \quad (2.41)$$

$$T(\mathbf{r}, t) = T_0 + T_a(\mathbf{r}, t) \quad [\text{K}] \quad (2.42)$$

$$\rho(\mathbf{r}, t) = \rho_0 + \rho_a(\mathbf{r}, t) \quad [\text{kg/m}^3] \quad (2.43)$$

with p_0 , T_0 and ρ_0 being the steady state values and p_a , T_a and ρ_a the small variations of the respective quantities. This approximation allows to neglect all cross products of the variation terms, so that a linearised Navier-Stokes equation is obtained, linking velocity to density and pressure:

$$\frac{\partial \mathbf{v}}{\partial t} = -\frac{1}{\rho_0} \nabla p_a(\mathbf{r}, t) + D_v \nabla (\nabla \cdot \mathbf{v}_l) \quad [\text{m/s}^2] \quad (2.44)$$

where $D_v = 4\eta/3\rho_0 + \eta_b/\rho_0$ is a coefficient taking into account sheer (η) and bulk (η_b) viscosity. The subscript l on velocity \mathbf{v}_l in the right term of the equation refers to the longitudinal component of the fluid velocity, which is the only responsible component for pressure variation, as long as boundary conditions are not concerned.

Thermal diffusion is also related to density and pressure through the following equation:

$$\begin{aligned} \frac{K_T}{\rho_0 C_p} \nabla^2 T_a(\mathbf{r}, t) = \frac{\partial}{\partial t} \left(T_a(\mathbf{r}, t) - \frac{\gamma - 1}{\gamma \beta_T} \kappa_T p_a(\mathbf{r}, t) \right) \\ - \frac{H(\mathbf{r}, t)}{\rho_0 C_p} \quad [\text{K/s}] \quad (2.45) \end{aligned}$$

K_T being the thermal conductivity, C_p the heat capacity at constant pressure, $\gamma = C_p/C_v$ the ratio of specific heats at constant pressure and volume, β_T a coefficient of thermal expansion, κ_T the isothermal compressibility and H the heat production rate, as defined in eq. (2.31).

Equation of mass-density continuity can be expressed as:

$$\frac{\partial \rho_a(\mathbf{r}, t)}{\partial t} + \rho_0 \nabla \cdot \mathbf{v}_l = 0 \quad [\text{kg}/(\text{m}^3\text{s})] \quad (2.46)$$

Finally, a thermodynamic equation of state interrelates density, pressure and temperature of the medium:

$$\begin{aligned} \rho_a(\mathbf{r}, t) = \left(\frac{\partial \rho}{\partial P} \right)_{T_0} p_a(\mathbf{r}, t) + \left(\frac{\partial \rho}{\partial T} \right)_{p_0} T_a(\mathbf{r}, t) = \\ = \frac{\gamma}{c_s^2} \left(p_a(\mathbf{r}, t) - \frac{\beta_T}{\kappa_T} T_a(\mathbf{r}, t) \right) \quad [\text{kg/m}^3] \quad (2.47) \end{aligned}$$

where c_s is the sound velocity in the medium.

The four described relations can be combined together to finally obtain a wave equation. The velocity \mathbf{v}_l is eliminated by merging the divergence of eq. (2.44) into eq. (2.46):

$$\nabla^2 p_a(\mathbf{r}, t) = \frac{\partial^2 \rho_a(\mathbf{r}, t)}{\partial t^2} - D_v \nabla^2 \left(\frac{\partial \rho_a(\mathbf{r}, t)}{\partial t} \right) \quad [\text{Pa/m}^2] \quad (2.48)$$

Including the thermodynamic state equation (2.47) allows to obtain a relation depending only on pressure and temperature:

$$\begin{aligned} \nabla^2 p_a(\mathbf{r}, t) &= \frac{\gamma}{c_s^2} \left[\frac{\partial^2}{\partial t^2} - D_v \nabla^2 \frac{\partial}{\partial t} \right] \\ &\times \left(p_a(\mathbf{r}, t) - \frac{\beta_T}{\kappa_T} T_a(\mathbf{r}, t) \right) \quad [\text{Pa/m}^2] \end{aligned} \quad (2.49)$$

The couple of equations (2.45) and (2.49) shows two independent plane wave solutions: a very strongly damped thermal wave with submillimetre wavelength, and a slightly damped sound wave with a wavelength ranging from few centimetres to few metres. The thermal wave is usually only observed in the neighbourhood of the exciting light beam, due to the significant damping factor; hence, its distribution is generally small with respect to cell dimensions, leading to the possibility to neglect the second spatial derivatives of $T_a(\mathbf{r}, t)$.

A unique equation is then derived by the combination of the two relations:

$$\begin{aligned} \nabla^2 p_a(\mathbf{r}, t) - \frac{1}{c_s^2} \frac{\partial^2 p_a(\mathbf{r}, t)}{\partial t^2} + \frac{1}{c_s^2} D_v \frac{\partial}{\partial t} \nabla^2 p_a(\mathbf{r}, t) &= \\ = -\frac{\gamma - 1}{c_s^2} \frac{\partial H(\mathbf{r}, t)}{\partial t} \quad [\text{Pa/m}^2] \end{aligned} \quad (2.50)$$

corresponding to a damped wave equation with a source term on the right side. The damping contribution, related to viscosity losses (third term on the left side), makes it impossible to solve this equation analytically. Therefore, in a first time, a solution will be found for the undamped equation, and influence of the losses will be taken into account successively:

$$\nabla^2 p_a(\mathbf{r}, t) - \frac{1}{c_s^2} \frac{\partial^2 p_a(\mathbf{r}, t)}{\partial t^2} = -\frac{\gamma - 1}{c_s^2} \frac{\partial H(\mathbf{r}, t)}{\partial t} \quad [\text{Pa/m}^2] \quad (2.51)$$

2.4 Acoustic resonators

Solutions of the inhomogeneous wave equation (2.51) directly depend on the shape and the dimensions of the measurement cell. In the most general case, the resonances of an acoustic cell are given by the solutions of the following homogeneous wave equation:

$$\nabla^2 p_a(\mathbf{r}, t) - \frac{1}{c_s^2} \frac{\partial^2 p_a(\mathbf{r}, t)}{\partial t^2} = 0 \quad [\text{Pa/m}^2] \quad (2.52)$$

so that the pressure wave can be expressed as the sum of all the resonant modes of the cell:

$$p_a(\mathbf{r}, t) = A_0(t) + \sum_n A_n(t) p_n(\mathbf{r}) \quad [\text{Pa}] \quad (2.53)$$

where $A_n(t)$ is the amplitude of the n^{th} mode and $p_n(\mathbf{r})$ its dimensionless spatial distribution.

Taking into account the harmonic time dependence $e^{j\omega t}$ of the sound wave, the inhomogeneous wave equation can be written as:

$$-\omega^2 A_0 + \sum_n (\omega_n^2 - \omega^2) A_n p_n(\mathbf{r}) = j\omega(\gamma - 1)H(\mathbf{r}) \quad [\text{Pa/s}^2] \quad (2.54)$$

ω_n being the resonant frequency corresponding to the n^{th} mode.

Respective mode amplitudes A_n are derived assuming that each mode is orthogonal with respect to the others, hence the spatial integral of the cross product between any two different modes is zero:

$$A_n = \frac{j\omega(\gamma - 1)}{\omega_n^2 - \omega^2 + j\frac{\omega\omega_n}{Q_n}} \frac{\int_{V_{res}} H(\mathbf{r})p_n(\mathbf{r})dV}{\int_{V_{res}} |p_n(\mathbf{r})|^2 dV} \quad [\text{Pa}] \quad (2.55)$$

where V_{res} is the volume of the resonator and Q_n is the quality factor of the n^{th} resonant mode. This latter quantity is introduced to take into account the previously neglected acoustic losses (see § 2.3.2). The physical meaning of the Q factor is the ratio between the energy that a resonant mode can accumulate during one period and the energy which is lost, due to various dissipation processes, during the same period. Loss mechanisms concretely result in a broadening $\Delta\omega_n$ of the resonant mode, so that Q factor can be defined as follows:

$$Q_n = \frac{\omega_n}{\Delta\omega_n} \quad [-] \quad (2.56)$$

Mode broadening $\Delta\omega_n$ is measured between the points where the mode amplitude is worth $1/\sqrt{2}$ of its peak value.

According to eq. (2.35), heat production rate H can be expressed as a function of light intensity I_0 , which, in turn, depends on incident optical power P_0 :

$$H(\mathbf{r}) = \alpha I_0(\mathbf{r}) = \alpha P_0 g(\mathbf{r}) \quad [\text{J}/(\text{s}\cdot\text{cm}^3)] \quad (2.57)$$

where $g(\mathbf{r})$ is the normalised spatial distribution of the light beam intensity.

Mode amplitude can then be written as:

$$A_n = \frac{j\omega(\gamma - 1) \alpha P_0 l_{path}}{\left(\omega_n^2 - \omega^2 + j\frac{\omega\omega_n}{Q_n}\right) V_{res}} \frac{\frac{1}{l_{path}} \int_{V_{res}} g(\mathbf{r})p_n(\mathbf{r})dV}{\frac{1}{V_{res}} \int_{V_{res}} |p_n(\mathbf{r})|^2 dV} \quad [\text{Pa}] \quad (2.58)$$

l_{path} being the length of effective interaction between light and gas.

The two spatial integrals on right side of this equation represent respectively the overlap between the distributions of light beam and pressure mode along the resonator, and a normalisation factor of the pressure mode. The resulting ratio, indicated as F_n , is usually referred to as *normalised overlap integral*.

The pressure wave then becomes:

$$p_a(\mathbf{r}, \omega) = \frac{(\gamma - 1) \alpha P_0 l_{path}}{V_{res}} \times \left(\frac{1}{j\omega} + \sum_n \frac{j\omega F_n p_n(\mathbf{r})}{\omega_n^2 - \omega^2 + j\frac{\omega\omega_n}{Q_n}} \right) \quad [\text{Pa}] \quad (2.59)$$

A closer examination of eq. (2.59) reveals that an analogy can be established between the acoustic and electrical domains, so that the induced pressure wave is assimilated to a voltage U and the volume flow to a current I [15]:

$$U(\mathbf{r}, \omega) = p_a(\mathbf{r}, \omega) \quad [\text{Pa}] \quad (2.60)$$

$$I = \frac{(\gamma - 1)}{\rho c_s^2} \alpha P_0 l_{path} \quad [\text{m}^3/\text{s}] \quad (2.61)$$

The acoustic impedance resulting from the ratio of $U(\mathbf{r}, \omega)$ and I , is then derived:

$$Z(\mathbf{r}, \omega) = \frac{\rho c_s^2}{V_{res}} \left(\frac{1}{j\omega} + \sum_n \frac{j\omega F_n p_n(\mathbf{r})}{\omega_n^2 - \omega^2 + j\frac{\omega\omega_n}{Q_n}} \right) \quad [\text{Pa}\cdot\text{s}/\text{m}^3] \quad (2.62)$$

The first term within brackets refers to the non-resonant operating mode of the cell⁴. Generated photoacoustic signal in a non-resonant situation is inversely proportional to volume and frequency, and it is uniformly distributed along the cell:

$$p_a(\mathbf{r}, \omega) = p_a(\omega) = \frac{(\gamma - 1) \alpha P_0 l_{path}}{j\omega V_{res}} \quad [\text{Pa}] \quad (2.63)$$

The resulting sound enhancement is poorer than in resonant modes, and the sensitivity to the $1/f$ acoustic noise is significantly high, due to the fact that, in order to increase the magnitude of the photoacoustic signal, typical operating frequencies are very low (~ 100 Hz [16]).

On the other side, as already mentioned, the sum term in right side of eq. (2.62) is related to the resonant modes of the photoacoustic cell. A distinction can be made between two types of resonators, depending on the comparison between the dimensions of the cell and the acoustic wavelength Λ , defined as:

$$\Lambda = \frac{2\pi c_s}{\omega} \quad [\text{m}] \quad (2.64)$$

When the dimensions of the cell have the same order of magnitude than the acoustic wavelength, each resonant mode $p_n(\mathbf{r})$ is linked to an eigenmode of the cell; in the very common case of a cylindrical cell, for example, longitudinal, radial, azimuthal or hybrid resonances can be excited and used for sound amplification. The resulting resonant modes show the presence of nodes (points where the sound amplitude is equal to zero) and anti-nodes (points where the sound enhancement is highest) along their geometric distribution.

⁴The phrase “non-resonant cell” is widely used in literature in this case, but it is ambiguous and can lead to confusion, as the same cell can be used in a resonant or a non-resonant mode according to the operating frequency.

Hence, to efficiently excite a given mode, the normalised overlap integral F_n has to be as high as possible.

When the dimensions of the cell are much smaller than the acoustic wavelength, the sound wave is approximately the same in each point of the cell [17]; in fact, the pressure distribution along the resonator is ruled by the following relation:

$$p_a(\mathbf{r}) \propto e^{-jK\mathbf{r}} \quad [\text{Pa}] \quad (2.65)$$

where $K = 2\pi/\Lambda$ is the acoustic wave number and \mathbf{r} is the spacial propagation vector, bounded by the cell dimensions; if these are much smaller than the wavelength, the condition $Kr \ll 1$ is obtained, and the propagation inside the cell can be neglected. As a consequence, no eigenmode can be excited inside the cell.

In this case, ducts and openings of the cell can be considered as lumped-circuit impedances, and the acoustic impedance Z can be derived using these approximations. Under certain conditions, this acoustic impedance can show a resonance which is not linked to the geometric modes of the cell, and thus does not require any overlap with the light beam.

Helmholtz resonators are a typical example of this kind of systems; since they have been used to design the two photoacoustic cells developed in the frame of this work, a detailed description of their working principles is presented in the following section.

2.4.1 Helmholtz resonators

Helmholtz resonators owe their name to the German physicist Hermann von Helmholtz (1821 - 1894, Fig. 2.5 a), who dedicated part of his scientific activity to physiology of music; in his 1863 work “*Die Lehre der Tonempfindungen als physiologische Grundlage für die Theorie der Musik*”⁵ [18] Helmholtz demonstrated the importance of the harmonics of a sound for its perception; to achieve this purpose, he designed a series of spherical cavities with two small openings (Fig. 2.5 b), resonating at different frequencies.

Quoting from [18], “*these resonators are hollow spheres, with two openings. [...] One of these openings has straight edges, the other is funnel-shaped, in order to be introduced into the ear. [...] The air mass of this resonator forms an elastic system; [...] the fundamental sound of the sphere is considerably increased. The ear, in direct communication with the air inside the sphere, perceives immediately the increased sound. [...] Each person is then able to distinguish the considered sound among a great number of other sounds, even if it is weakly produced.*” Photoacoustic cells based on Helmholtz resonator have been investigated since early 80s [19], and have been more recently used with success to detect various gas species [20, 21, 22, 23].

More generally, a Helmholtz resonator is composed by a volume, whose shape has no relevance, and an open duct leading to free space. The air inside the volume forms an acoustic compliance, while the air inside the open duct acts as an acoustic mass. When the dimensions of the resonator are much smaller compared to the acoustic wavelength, an analogy with electrical circuits can be used [24], and the system corresponds to a capacitor (representing

⁵English edition was issued with the following title: “*On the sensations of tone as a physiological basis for the theory of music*”.

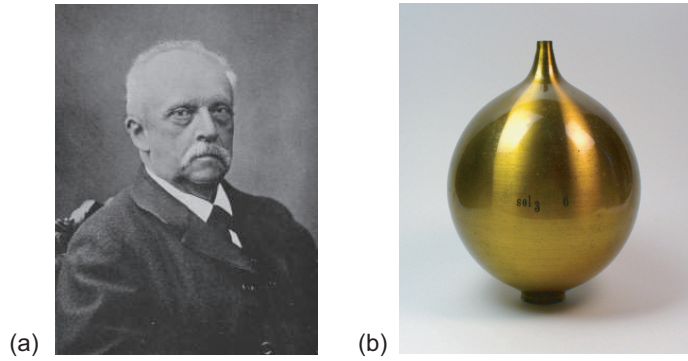


Figure 2.5: German physicist Hermann von Helmholtz (a) and an example of the resonators he used for his experiments on physiology of music (b).

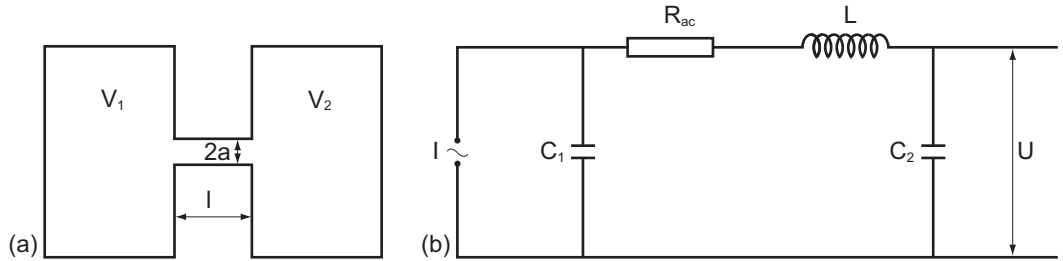


Figure 2.6: Scheme of a 2-volumes Helmholtz resonator (a) and its analogous electrical circuit (b). Capacitors correspond to the volumes, resistor and inductor to the duct, current to volume flow and voltage to sound pressure.

the volume), an inductor (representing the open duct) and a resistor (representing the viscous and thermal energy losses) in series. Such a circuit shows a resonance when the capacitive and the inductive part of the impedance compensate reciprocally.

This kind of Helmholtz resonator cannot be used directly as a photoacoustic cell because it is not closed. Indeed, despite the fact that photoacoustic detection with open cells has been demonstrated [25, 26], closed cells are generally preferred, as they provide a higher SNR, allow low pressure measurements, and mainly avoid mixing between ambient atmosphere and investigated gas, which can be very dangerous according to the gas compound.

To overcome this problem, a second volume can be added at the duct outlet, resulting in a system which is slightly more complex, but shows the advantage of being perfectly closed. Such a system can be described by the scheme illustrated in Fig. 2.6 along with its analogous electrical circuit. The equivalences between acoustic and electric domains are ruled by eq. (2.60) and (2.61), and by the following expressions [24]:

$$C_i = \frac{V_i}{\rho c_s^2} \quad i = 1, 2 \quad [\text{m}^3/\text{Pa}] \quad (2.66)$$

$$L = \frac{\rho l'}{\pi a^2} \quad [\text{Pa}\cdot\text{s}^2/\text{m}^3] \quad (2.67)$$

$$R_{ac} = \frac{\rho l' \omega}{\pi a^3} \left[\sqrt{\frac{2\eta}{\rho\omega}} + (\gamma - 1) \sqrt{\frac{2\kappa_T}{\rho\omega C_p}} \right] \quad [\text{Pa}\cdot\text{s}/\text{m}^3] \quad (2.68)$$

given that V_1 and V_2 are the volumes, l the duct length and a its radius. The effective length l' appearing in the inductance and resistance formulas is equal to the actual length of the connecting duct increased by an open-end correction factor, related to the duct radius a and to whether the duct outlet is flanged or not; in the case of a two volumes resonator, the effective duct length is given by [27]:

$$l' = l + \frac{16}{3\pi} a \quad [\text{m}] \quad (2.69)$$

It is important to note that accuracy of eq. (2.67) and (2.68) is fine for a limited frequency and duct radius range [28]; outside this range, other analytic expressions, or numerical approximations, must be used. More generally, when the dimensions of the resonator cannot be considered much smaller than the acoustic wavelength, a more complex and accurate model, based on distributed elements, have to be applied to predict the resonator behaviour [19].

The efficiency of a photoacoustic cell is usually described by the so-called *cell constant*, defined as the ratio between generated sound pressure and absorbed optical power per unit length, and related to the previously introduced acoustic impedance $Z(\omega)$:

$$C_{cell} = \frac{p}{\alpha_0 P_0 C_{gas}} = \frac{(\gamma - 1)}{\rho c_s^2} Z(\omega) l_{path} \quad [\text{Pa}\cdot\text{cm}/\text{W}] \quad (2.70)$$

The acoustic impedance of the Helmholtz resonator equivalent circuit can be calculated using the theory of electrical circuits:

$$\begin{aligned} Z(\omega) &= \frac{U}{I} = \\ &= \frac{-1}{\omega^2 R_{ac} C_1 C_2 - j\omega(C_1 + C_2 - \omega^2 L C_1 C_2)} \quad [\text{Pa}\cdot\text{s}/\text{m}^3] \end{aligned} \quad (2.71)$$

Resonant angular frequency ω_{res} in the case of a lossless circuit ($R = 0$) is given by:

$$\omega_{res} |_{R_{ac}=0} = \omega_0 = \sqrt{\frac{C_1 + C_2}{L C_1 C_2}} \quad [\text{rad}/\text{s}] \quad (2.72)$$

while quality factor Q is defined by:

$$Q = \frac{1}{R_{ac}} \sqrt{\frac{L(C_1 + C_2)}{C_1 C_2}} = \omega_0 \frac{L}{R_{ac}} \quad [-] \quad (2.73)$$

Merging eq. (2.72) and (2.73) into eq. (2.71) the acoustic impedance becomes:

$$Z(\omega) = \frac{1}{j\omega L C_1 C_2 [(\omega_0^2 - \omega^2) + j\omega_0 \omega / Q]} \quad [\text{Pa}\cdot\text{s}/\text{m}^3] \quad (2.74)$$

Resonant angular frequency ω_{res} is then derived:

$$\omega_{res} = \omega_0 \sqrt{1 - \frac{1}{2Q^2}} \quad [\text{rad}/\text{s}] \quad (2.75)$$

In the case of a high quality factor ($Q > 10$), condition which is easily obtained for an accurately designed resonator, the losses impact on resonant frequency can be neglected and $\omega_{res} \approx \omega_0$ [20].

At this resonant frequency, the modulus of eq. (2.71) merged into eq. (2.70) gives the following cell constant:

$$C_{cell} = \frac{(\gamma - 1)}{\rho c_s^2} \frac{L}{R_{ac}(C_1 + C_2)} l_{path} \quad [\text{Pa}\cdot\text{m}/\text{W}] \quad (2.76)$$

Finally, using eq. (2.66) to (2.69) into eq. (2.76), the cell constant as a function of the geometric dimensions of the resonator is obtained:

$$C_{cell} = \frac{(\gamma - 1)}{\pi^{1/4} c_s^{1/2}} \frac{1}{\sqrt{\frac{2\eta}{\rho}} + (\gamma - 1) \sqrt{\frac{2\kappa_T}{\rho C_p}}} \\ \times a^{1/2} \left(l + \frac{16}{3\pi} a \right)^{1/4} \frac{(V_1 V_2)^{1/4}}{(V_1 + V_2)^{5/4}} l_{path} \quad [\text{Pa}\cdot\text{m}/\text{W}] \quad (2.77)$$

Design and optimisation of the two Helmholtz resonator photoacoustic cells has been performed using this expression (see § 3.2 and 4.2).

In order to compare the theoretical cell constants with experimental results, it can be helpful to introduce in eq. (2.77) a factor that takes into account the influence of the microphone used for the detection, and, in case, of the preamplifier used to enhance microphone signal:

$$C_{mic} = G_m \cdot M_m \cdot C_{cell} \quad [\text{mV}\cdot\text{m}/\text{W}] \quad (2.78)$$

where G_m is the preamplifier gain and M_m the microphone sensitivity, expressed in mV/Pa.

2.4.2 Other photoacoustic detectors

To conclude the chapter, an overview of other photoacoustic systems is presented.

2.4.2.1 Cylindrical cavities

Cylindrical cavities are among the most common cells used in photoacoustic spectroscopy. This is due to their simple geometry, their intrinsic symmetry, the easy overlap between their resonant modes and the laser beam, and their high sensitivity and quality factor.

Spatial dependence in a cylindrical cavity, i.e. the positioning of nodes and anti-nodes along the modes, depends on whether the cavity is closed or open at its ends (Fig. 2.7). In particular, azimuthal and radial modes do not change, while longitudinal modes show a node at the cavity end when this end is open (sound pressure equal to zero), respectively an anti-node when the end is closed (sound speed equal to zero). As photoacoustic cylindrical cells are generally either closed at both ends, or open at both ends, only these two cases will be considered. In both cases, resonant frequencies are derived from eq. (2.59), using the appropriate boundary conditions [17]:

$$f_{kmn} = \frac{c_s}{2} \sqrt{\left(\frac{k}{l'}\right)^2 + \left(\frac{\gamma_{mn}}{\pi a}\right)^2} \quad [\text{Hz}] \quad (2.79)$$

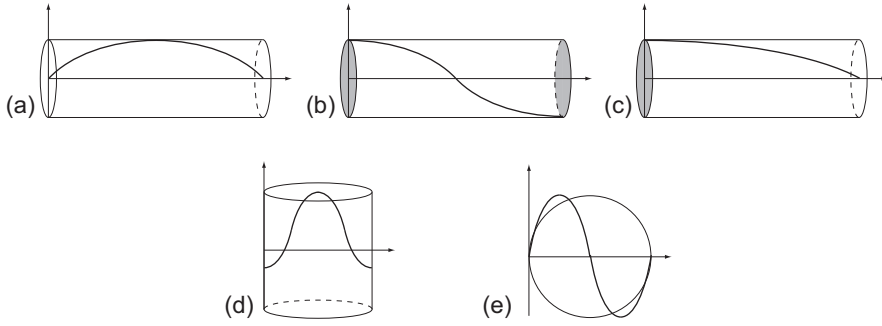


Figure 2.7: Pressure distribution in cylindrical cavities: longitudinal for an open-open (a) a closed-closed (b) and an open-closed (c) cell, radial (d) and azimuthal (e).

where l' and a are the cavity effective length and radius, k , m , and n are respectively the longitudinal, azimuthal and radial indices, and γ_{mn} is the n^{th} extremum of first order Bessel function J_m . For instance, first longitudinal ($k = 1$, $m = n = 0$) and radial ($k = m = 0$, $n = 1$) modes show a respective resonant frequency of:

$$f_{100} = \frac{c_s}{2l'}; \quad f_{001} = \frac{c_s}{2} \cdot \frac{3.832}{\pi a} \quad [\text{Hz}] \quad (2.80)$$

All the three resonant modes of a cylindrical cavity can be efficiently implemented to perform photoacoustic measurements, though their characteristics and performances are sensibly different.

Cells designed to be used in radial modes [4, 29, 30, 31, 32] show very high quality factors, up to several hundreds; a very efficient noise reduction is obtained, especially if the laser axis is misaligned with respect of the cell, so that inlet and outlet windows, where some photoacoustic noise is generated, coincide with mode nodes. They generally operate at high frequencies (~ 10 kHz), which is an advantage in terms of noise susceptibility, but on the other hand they are more sensible to relaxation effects, which tend to increase with frequency [12]. The size of a radial cell is usually not very compact (typical dimensions: $2a \sim 5$ -10 cm, $l \sim 10$ -20 cm). High power CO/CO₂ lasers are the most common light sources used in conjunction with radial resonators. Flow measurements up to several litres per minutes are generally allowed with no negative effect on the SNR.

Longitudinal cells [33, 34, 35, 36, 37, 38] show the most natural and efficient overlap with laser beam; they can achieve better cell constants with respect to radial cells, despite their smaller dimensions, specially concerning the diameter (~ 1 cm); this makes them particularly suitable to be used along with DFB semiconductor lasers. They generally operate in the kilohertz range, therefore they need an efficient acoustic filtering, easily achieved adding quarter-wavelength long buffer volumes at cell extremities; their main shortcomings are represented by a lower quality factor (~ 20 -50), higher noise susceptibility, and lower flow measurements (~ 1 l/min).

Azimuthal modes are less commonly implemented in PAS, mainly because of their poor quality factor (viscous losses for azimuthal resonances are very high) and their required off-axis excitation, though several applications can be found in literature [25, 31, 39, 40, 41, 42].

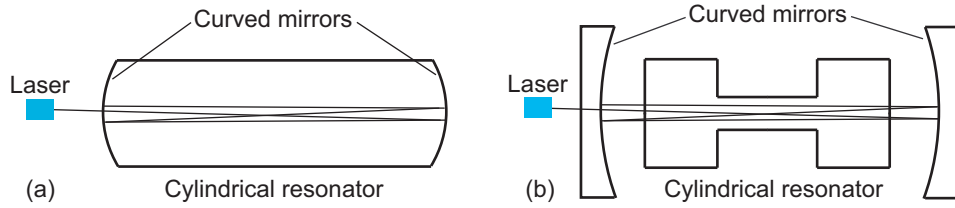


Figure 2.8: Multipass configuration with internal (a) or external (b) mirrors. The use of curved mirror increases the interaction length between light and gas.

2.4.2.2 Multipass resonant cells

Multipass resonant cells are based on the principle that increasing the interaction length between laser beam and probed gas (l_{path} in eq. (2.76)) results in a proportional increase of the photoacoustic signal. Multipass configurations have been investigated since mid 70s [43, 44, 45], using high quality mirrors (plane or curved) at the edges of the cells (Fig. 2.8 a). More recently, external mirrors have been used to achieve the multipass effect (Fig. 2.8 b), either in Herriott [46, 47, 48] or in Fabry-Perot [49] configuration. Herriott arrangement simply consists in the augmentation of light-gas interaction path by means of two curved external mirrors suitably aligned to obtain multiple reflections (up to 80 passes in a 70 cm cell have been demonstrated); Fabry-Perot setup produces light amplification at the exact laser wavelength by optical resonance inside the cavity formed by the 2 concave mirrors, with a resulting optical gain reaching values as high as 100, according to the cavity finesse. Both Herriott and Fabry-Perot configuration are generally coupled with cylindrical cells, whose resonances are efficiently excited by the multiple passes of the laser beam; moreover, compared to internal mirrors configurations, they show the advantage of dramatically reducing wall noise, as the photoacoustic noise produced by light absorption in the mirrors is not coupled inside the cell.

Multipass cells' main shortcoming is their intrinsic setup complexity; mechanical stability of the mirrors is a parameter of utmost importance, and has to be carefully controlled; in addition, in Fabry-Perot configuration a piezo-electric based regulation system is required in order to lock the cavity length to the laser wavelength, which implies a regulation sensitivity in the μm range (the distance between the mirrors has to be a semi-integer multiple of the wavelength).

2.4.2.3 Intracavity resonant cells

Intracavity resonant cells (Fig. 2.9) are very similar in their principle to multipass cells, the concrete difference being the use of an external cavity laser instead of a standard laser diode. Photoacoustic cell (usually a longitudinal cylindrical resonator) is then placed inside the external cavity, thus taking benefit of a very high optical power.

Different external cavity lasers have been utilised to perform intracavity photoacoustic detection, such as CO_2 [50, 51] or semiconductor sources [42].

Intracavity resonant cells can provide high sensitivity, but as in the case of multipass cells, the main drawback is their complexity and their required

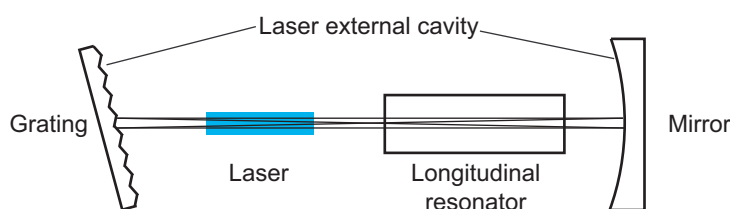


Figure 2.9: Intracavity configuration using an external cavity laser. A very high power is coupled into the acoustic resonator thanks to the multiple reflections of the laser beam.

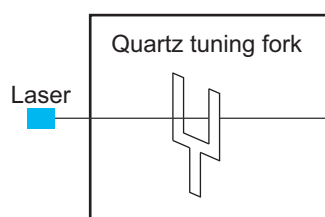


Figure 2.10: Quartz-enhanced configuration. The tuning fork substitutes both the resonator and the microphone of a conventional photoacoustic setup.

extremely precise alignment and stabilisation.

2.4.2.4 Quartz-enhanced resonant cells

A very peculiar recently developed detection technique, denominated quartz-enhanced photoacoustic spectroscopy (QEPAS), consists in the use of a conventional clock quartz tuning fork (Fig. 2.10) in the double role of acoustic resonator and sound detection element [52].

Photoacoustic signal generated in the area between the prongs of the tuning fork is first amplified by the very high quality factor ($Q > 10000$) fork resonance and then transformed into an electrical signal through the piezoelectric transducer formed by the fork itself. Such a system shows several advantages: beside the very high quality factor, a very low ambient noise susceptibility is obtained, because of the high fork resonance frequency (32.8 kHz) and because sound generated far from the fork does not excite its resonant mode; the system is very small and compact, a cell is only needed to separate investigated gas compound from ambient atmosphere, but there are no restrictions concerning its volume and shape. Further enhancement of the photoacoustic signal can be achieved adding longitudinal resonators on both sides of the fork [53]. On the other hand, main drawbacks consist in a very short interaction path length between light and gas (approximately equivalent to the tuning fork thickness), and in the relaxation effects which can arise due to the very high operation frequency [12], both resulting in a loss of sensitivity. For this reason, to increase sensitivity, quartz-enhanced photoacoustic systems generally operate at very low pressure (~ 50 torr) [54, 55].

Bibliography

- [1] A. G. Bell, "On the production and reproduction of sound by light," *Am. J. Sci.* **20**(118), 305–324 (1880).
- [2] M. L. Viengerov, "New method of gas analysis based on Tyndall-Roentgen opto-acoustic effect," *Dokl. Akad. Nauk SSSR* **19**, 687 (1938).
- [3] E. L. Kerr and J. G. Atwood, "Laser illuminated absorptivity spectrophone: a method for measurement of weak absorptivity in gases at laser wavelengths," *Appl. Opt.* **7**(5), 915–922 (1968).
- [4] P. L. Meyer and M. W. Sigrist, "Atmospheric pollution monitoring using CO₂-laser photoacoustic spectroscopy and other techniques," *Rev. Sci. Instrum.* **61**(7), 1779–1807 (1990).
- [5] J. M. Hollas, *Modern spectroscopy* (John Wiley & Sons, Chichester, 1999).
- [6] G. Herzberg, *Molecular spectra and molecular structure*, vol. vol. I - Spectra of diatomic molecules (Malabar, Krieger, 1950).
- [7] L. S. Rothman, D. Jacquemart, A. Barbe, D. C. Benner, M. Birk, L. R. Brown, M. R. Carleer, C. Chackerian, K. Chance, L. H. Coudert, V. Dana, V. M. Devi, J. M. Flaud, R. R. Gamache, A. Goldman, J. M. Hartmann, K. W. Jucks, A. G. Maki, J. Y. Mandin, S. T. Massie, J. Orphal, A. Perrin, C. P. Rinsland, M. A. H. Smith, J. Tennyson, R. N. Tolchenov, R. A. Toth, J. Vander Auwera, P. Varanasi, and G. Wagner, "The HITRAN 2004 molecular spectroscopic database," *J. Quant. Spectrosc. Radiat. Transf.* **96**(2), 139–204 (2005).
- [8] J. J. Olivero and R. L. Longbothum, "Empirical fits to Voigt linewidth: a brief review," *J. Quant. Spectrosc. Radiat. Transfer* **17**(2), 233–236 (1977).
- [9] A. Miklós, S. Schäfer, and P. Hess, *Photoacoustic spectroscopy, theory*, Encyclopedia of spectroscopy and spectrometry (Academic, New York, 1999).
- [10] A. C. Tam, *Ultra sensitive laser spectroscopy* (Academic press, New York, 1983).
- [11] P. Hess, "Resonant photoacoustic spectroscopy," *Top. Curr. Chem.* **111**, 1–32 (1983).
- [12] S. Schilt, J. P. Besson, and L. Thévenaz, "Near-infrared laser photoacoustic detection of methane: the impact of molecular relaxation," *Appl. Phys. B* **82**(2), 319–328 (2006).
- [13] H. E. Bass and H. J. Bauer, "Kinetic model for thermal blooming in atmosphere," *Appl. Opt.* **12**(7), 1506–1510 (1973).
- [14] J. P. M. Trusler, *Physical acoustics and metrology of fluids*, The Adam Hilger series on measurement science and technology (Adam Hilger, Bristol, 1991).

-
- [15] A. Miklós, P. Hess, and Z. Bozóki, “Application of acoustic resonators in photoacoustic trace gas analysis and metrology,” *Rev. Sci. Instrum.* **72**(4), 1937–1955 (2001).
- [16] J. Henningsen and N. Melander, “Sensitive measurement of adsorption dynamics with nonresonant gas phase photoacoustics,” *Appl. Opt.* **36**(27), 7037–7045 (1997).
- [17] M. Rossi, *Electroacoustique*, Traité d’électricité (Presses polytechniques romandes, Lausanne, 1986).
- [18] H. v. Helmholtz, *Die lehre von den tonempfindungen als physiologische grundlage für die theorie der musik* (Vieweg, Braunschweig, 1863).
- [19] O. Nordhaus and J. Pelzl, “Frequency dependence of resonant photoacoustic cells: the extended Helmholtz resonator,” *Appl. Phys.* **25**(3), 221–229 (1981).
- [20] R. Kästle and M. W. Sigrist, “Temperature-dependent photoacoustic spectroscopy with a Helmholtz resonator,” *Appl. Phys. B* **63**(4), 389–397 (1996).
- [21] V. Zéninari, V. A. Kapitanov, D. Courtois, and Y. N. Ponomarev, “Design and characteristics of a differential Helmholtz resonant photoacoustic cell for infrared gas detection,” *Infrared Phys. Technol.* **40**(1), 1–23 (1999).
- [22] S. Barbieri, J. P. Pellaux, E. Studemann, and D. Rosset, “Gas detection with quantum cascade lasers: An adapted photoacoustic sensor based on Helmholtz resonance,” *Rev. Sci. Instrum.* **73**(6), 2458–2461 (2002).
- [23] V. Zéninari, B. Parvitte, D. Courtois, V. A. Kapitanov, and Y. N. Ponomarev, “Methane detection on the sub-ppm level with a near-infrared diode laser photoacoustic sensor,” *Infrared Phys. Technol.* **44**(4), 253–261 (2003).
- [24] P. M. Morse and K. U. Ingard, *Theoretical acoustics* (Princeton University Press, Princeton, 1968).
- [25] A. Miklós and A. Lorincz, “Windowless resonant acoustic chamber for laser photoacoustic applications,” *Appl. Phys. B* **48**(3), 213–218 (1989).
- [26] A. Keller, M. Rüegg, M. Forster, M. Loepfe, R. Pleisch, P. Nebiker, and H. Burtscher, “Open photoacoustic sensor as smoke detector,” *Sens. Actuators B* **104**(1), 1–7 (2005).
- [27] L. E. Kinsler, A. R. Frey, A. B. Coppens, and J. V. Sanders, *Fundamentals of acoustics* (Wiley, New York, 2001).
- [28] A. H. Benade, “On propagation of sound waves in a cylindrical conduit,” *J. Acoust. Soc. Am.* **44**(2), 616–623 (1968).
- [29] S. Schilt, L. Thévenaz, M. Niklès, L. Emmenegger, and C. Hüglin, “Ammonia monitoring at trace level using photoacoustic spectroscopy in industrial and environmental applications,” *Spectrochim. Acta A* **60**(14), 3259–3268 (2004).

- [30] A. Thöny and M. W. Sigrist, “New developments in CO₂-laser photoacoustic monitoring of trace gases,” *Infrared Phys. Technol.* **36**(2), 585–615 (1995).
- [31] C. Brand, A. Winkler, P. Hess, A. Miklós, Z. Bozóki, and J. Sneider, “Pulsed-laser excitation of acoustic modes in open high-Q photoacoustic resonators for trace gas monitoring: results for C₂H₄,” *Applied Optics* **34**(18), 3257–3266 (1995).
- [32] R. Gerlach and N. M. Amer, “Brewster window and windowless resonant spectrophones for intracavity operation,” *Appl. Phys.* **23**(3), 319–326 (1980).
- [33] J.-P. Besson, S. Schilt, and L. Thévenaz, “Multi-gas sensing based on photoacoustic spectroscopy using tunable laser diodes,” *Spectrochim. Acta A* **60**(14), 3449–3456 (2004).
- [34] F. G. C. Bijnen, J. Reuss, and F. J. M. Harren, “Geometrical optimization of a longitudinal resonant photoacoustic cell for sensitive and fast trace gas detection,” *Rev. Sci. Instrum.* **67**(8), 2914–2923 (1996).
- [35] A. Boschetti, D. Bassi, E. Iacob, S. Iannotta, L. Ricci, and M. Scotoni, “Resonant photoacoustic simultaneous detection of methane and ethylene by means of a 1.63- μ m diode laser,” *Appl. Phys. B* **74**, 273–278 (2002).
- [36] Z. Bozóki, A. Mohácsi, G. Szabó, Z. Bor, M. Erdélyi, W. D. Chen, and F. K. Tittel, “Near-infrared diode laser based spectroscopic detection of ammonia: A comparative study of photoacoustic and direct optical absorption methods,” *Appl. Spectrosc.* **56**(6), 715–719 (2002).
- [37] E. Kritchman, S. Shtrikman, and M. Slatkine, “Resonant optoacoustic cells for trace gas analysis,” *J. Opt. Soc. Am.* **68**(9), 1257–1271 (1978).
- [38] S. Bernegger and M. W. Sigrist, “CO-laser photoacoustic spectroscopy of gases and vapours for trace gas analysis,” *Infrared Phys. Technol.* **30**(5), 375–429 (1990).
- [39] A. Petzold and R. Niessner, “Novel design of a resonant photoacoustic spectrophone for elemental carbon mass monitoring,” *Appl. Phys. Lett.* **66**(10), 1285–1287 (1995).
- [40] M. Wolff and H. Harde, “Photoacoustic spectrometer based on a DFB-diode laser,” *Infrared Phys. Technol.* **41**(5), 283–286 (2000).
- [41] K. M. Adams, “Real-time *in situ* measurements of atmospheric optical absorption in the visible via photoacoustic spectroscopy. 1: Evaluation of photoacoustic cells,” *Appl. Opt.* **27**(19), 4052–4056 (1988).
- [42] Z. Bozóki, J. Sneider, G. Szabó, A. Miklós, M. Serényi, G. Nagy, and M. Fehér, “Intracavity photoacoustic gas detection with an external cavity diode laser,” *Appl. Phys. B* **63**(4), 399–401 (1996).
- [43] P. D. Goldan and K. Goto, “Acoustically resonant system for detection of low-level infrared absorption in atmospheric pollutants,” *J. Appl. Phys.* **45**(10), 4350–4355 (1974).

-
- [44] R. D. Kamm, "Detection of weakly absorbing gases using a resonant optoacoustic method," *J. Appl. Phys.* **47**(8), 3550–3558 (1976).
- [45] K. Veeken, N. Dam, and J. Reuss, "A multipass transverse photoacoustic cell," *Infrared Phys.* **25**(5), 683–696 (1985).
- [46] J. B. McManus, P. L. Keabian, and W. S. Zahniser, "Astigmatic mirror multipass absorption cells for long-path-length spectroscopy," *Appl. Opt.* **34**(18), 3336–3348 (1995).
- [47] M. Nägele and M. W. Sigrist, "Mobile laser spectrometer with novel resonant multipass photoacoustic cell for trace-gas sensing," *Appl. Phys. B* **70**(6), 895–901 (2000).
- [48] J. M. Rey, D. Marinov, D. E. Vogler, and M. W. Sigrist, "Investigation and optimisation of a multipass resonant photoacoustic cell at high absorption levels," *Appl. Phys. B* **80**(2), 261–266 (2005).
- [49] A. Rossi, R. Buffa, M. Scotoni, D. Bassi, S. Iannotta, and A. Boschetti, "Optical enhancement of diode laser-photoacoustic trace gas detection by means of external Fabry-Perot cavity," *Appl. Phys. Lett.* **87**(4), 3 (2005).
- [50] F. J. M. Harren, F. G. C. Bijnen, J. Reuss, L. Voeselek, and C. Blom, "Sensitive intracavity photoacoustic measurements with a CO₂ waveguide laser," *Appl. Phys. B* **50**(2), 137–144 (1990).
- [51] T. Fink, S. Büscher, R. Gäbler, Q. Yu, A. Dax, and W. Urban, "An improved CO₂ laser intracavity photoacoustic spectrometer for trace gas analysis," *Rev. Sci. Instrum.* **67**(11), 4000–4004 (1996).
- [52] A. A. Kosterev, Y. A. Bakirkin, R. F. Curl, and F. K. Tittel, "Quartz-enhanced photoacoustic spectroscopy," *Opt. Lett.* **27**(21), 1902–1904 (2002).
- [53] D. Weidmann, A. A. Kosterev, F. K. Tittel, N. Ryan, and D. McDonald, "Application of a widely electrically tunable diode laser to chemical gas sensing with quartz-enhanced photoacoustic spectroscopy," *Opt. Lett.* **29**(16), 1837–1839 (2004).
- [54] A. A. Kosterev and F. K. Tittel, "Ammonia detection by use of quartz-enhanced photoacoustic spectroscopy with a near-IR telecommunication diode laser," *Appl. Opt.* **43**(33), 6213–6217 (2004).
- [55] A. A. Kosterev, Y. A. Bakirkin, and F. K. Tittel, "Ultrasensitive gas detection by quartz-enhanced photoacoustic spectroscopy in the fundamental molecular absorption bands region," *Appl. Phys. B* **80**(1), 133–138 (2005).

Chapter 3

Helmholtz photoacoustic sensor

This chapter will address the design, the characterisation and the description of the performances of the first Helmholtz-based photoacoustic cell used in the frame of this work.

A general motivation of the target application, along with all the criteria which set the guidelines for the cell design, and the description of the design itself are provided at first.

Subsequently, a characterisation of the acoustic and photoacoustic behaviour of the cell is presented, including the different possible improvements to the setup.

Finally, trace gas sensing using the developed cell is described; results for methane, used for preliminary tests and sensor troubleshooting, are presented first, followed by details on ammonia detection and on the ultimate performances achieved with this photoacoustic setup.

3.1 Introduction

The spectral region between 2 and 2.7 μm is particularly attractive for spectroscopic measurements. Many species of environmental interest (CH_4 , NH_3 , CO , etc.) present stronger absorption lines in this window compared to the NIR region (Table 3.1); furthermore, some molecules, like hydrofluoric acid (HF), show their fundamental absorption lines in the region. Absorption by water vapour and carbon dioxide is weak, which makes this window very attractive for atmospheric and industrial applications. Finally, as it operates without photodetectors, PAS is particularly suitable to be performed in the whole MIR region, since at higher wavelengths photodetectors become costly and show poor performances.

The recent development of room-temperature antimonide-based semiconductor lasers emitting in this spectral window, operating in continuous wave (CW) mode, and supplied with a DFB structure (which guarantees a good spectral purity and a tuneability over several nm [1]), has made spectroscopic measurements in this region more efficient and convenient.

The photoacoustic cell described in this chapter has been opportunely conceived to suit the properties of these newly developed lasers, with the purpose to perform ammonia detection at ppm level.

Molecule	Absorption coefficient [cm^{-1}]		Improvement
	NIR region	2 - 2.7 μm region	
CH ₄	0.62 (@ 1.65 μm)	0.93 (@ 2.35 μm)	1.5
NH ₃	0.27 (@ 1.53 μm)	0.92 (@ 2.24 μm)	3.4
HF	7.64 (@ 1.27 μm)	251.7 (@ 2.45 μm)	33
CO	$3.01 \cdot 10^{-3}$ (@ 1.57 μm)	0.47 (@ 2.33 μm)	156

Table 3.1: Comparison between absorption coefficients at ambient temperature ($T = 296$ K) and pressure ($p = 1$ atm) between NIR region and 2 - 2.7 μm region for CH₄, NH₃, HF and CO, along with corresponding wavelengths.

3.2 Desing of the photoacoustic cell

3.2.1 Motivation and criteria for cell design

The design of the PA cell depends on many parameters, mainly determined by the requirements of the application. In this case, the guidelines for the design of the cell have been fixed by the characteristics of the laser diodes to be used, along with the properties of ammonia. The requirement of a compact, small-sized, portable instrument has played an important role on the sensor development as well.

The main peculiarity of the selected laser sources is their highly elliptical divergent beam. The typical spatial distribution of the laser emission was measured using a small surface photodetector mounted on a motorised translation stage directly in front of the laser, i.e. with no collecting optics. The detected power was measured in both directions as a function of the detector position, which gave the horizontal and vertical profiles of the laser beam. The measured profiles were then fitted in order to determine the beam waist in both directions (half width at $1/e^2$). The divergence angles of the laser emission were determined by measuring the beam waists at different distances from the laser. Divergences of 22° horizontally and 46° vertically (half angle at $1/e^2$) were obtained (see Fig. 3.1).

To efficiently exploit this divergence, the decision was taken to use the laser beam directly as emitted by the diodes, with no collimating optics, and with as few bulk optic elements as possible, in order to benefit from all the optical power without losses that standard glass elements could induce at this wavelength.

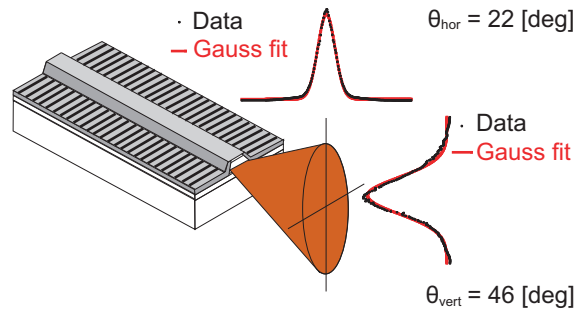


Figure 3.1: Measured divergence of the laser beam. *Black dots* represent the measured profile, *grey lines* the gaussian fit.

A Helmholtz resonator configuration suits such a non-collimated beam much better than a cylindrical cavity; in fact, on one side the overlap between any resonant mode in a cylindrical cell and a non-collimated beam would be poor, and on the other, as the Helmholtz resonance is equally excited in each point of the cell, photoacoustic signal generation by a non-collimated beam would be highly efficient. Moreover, the signal generation can be enhanced by implementing multiple beam reflections inside the photoacoustic cell, in order to increase the interaction path between light and gas.

Choice of the resonator dimensions must aim at the optimisation of the cell constant, given in eq. (2.77); this expression shows no local maximum with respect to any of the dimensions, so that the resonator should ideally consist of very small volumes and a very large and long duct, which is not realistic. Hence, design and optimisation have to take into account some physical and technical constraints, including:

- Absolute limitations on the cell dimensions in order to respect the condition $Kr \ll 1$ (see § 2.4)
- Mutual limitations between duct and volumes dimensions (duct surface and volume have to be much smaller compared to the two volumes, in order to ensure the resonant behaviour)
- Technical constraints, including available space for positioning of the gas inlet/outlet, the detecting microphone, a window to let the laser enter the cell, etc.
- Overall compact and reduced dimensions.

The resonant frequency, also determined by the cell dimensions, has to be kept in a range going from approximately 1 to 15 kHz. In fact, at frequencies below 1 kHz influence of the acoustic $1/f$ noise becomes very considerable, while 15 kHz is the typical upper limit of a microphone detection bandwidth.

Additional constraints on the shape of the cell are given by the laser beam profile: the window must permit the laser beam to completely enter the cell despite its divergence, given that the diode is positioned at a certain distance from it; moreover, a relatively long path between reflections inside the cell has to be guaranteed, as each succeeding reflected beam will have a lower power and generate a weaker signal.

For this last reason, the volume dedicated to generation of the photoacoustic signal (to be called excitation volume from now on), will contain as few external elements as possible, in order to maximise the available surface for laser beam reflection; hence, the microphone will be located in the other volume (detection volume); also, the choice of the material and of the surface quality is very important, as the number of useful reflections has to be maximised in order to increase the interaction path between light and gas.

Finally, choice of the material is also influenced by the nature of the investigated gas; for instance, ammonia is a strongly polar molecule, which tends to stick on the cell walls, resulting in an important reduction of the cell response time [2]; this effect can be minimised by a judicious choice of the cell material, or, more often, by a suitable coating on the cell walls [3]. For this reason, stainless steel has been selected as primary cell material, while the use

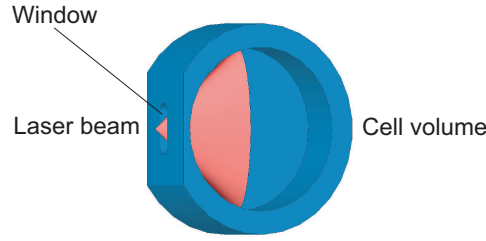


Figure 3.2: Scheme of the laser injection in the cell volume. The divergent beam enters from the side of the cylinder, so that the beam path between the walls is increased.

of a second cell made of aluminium and coated with a thin gold layer will be detailed in § 3.4.4.2.

3.2.2 Design of the photoacoustic cell

Helmholtz-based photoacoustic detectors reported in literature are generally composed of long cylindrical volumes connected by a thin tube [4, 5], the photoacoustic signal being generated inside one of the two volumes; this choice is motivated by the use of a collimated laser beam, which interacts with the gas along the whole cylinder length.

In this work, due to the high elliptical divergence of the source, a different concept has been implemented: the excitation volume has a cylindrical shape (of radius r_1 and height h_1), but the laser beam is injected from the side, through a thin glass window, so that the major axis of the elliptical beam profile is in the same geometrical plane than the cylinder section (Fig. 3.2).

This configuration maximises the beam path between reflections according to its divergent profile, increases the number of beam reflections thanks to the different incidence angles on the curved surface, and reduces the number of bulk optics element, as a single window is used and no lenses are needed.

Expected theoretical dependence of the cell constant on the geometrical dimensions of the cell, given in (2.77), has been calculated using mathematical simulations. Interaction length l_{path} has been estimated by calculating the optical power distribution as a function of the divergence angle, and by predicting the number of reflections for a certain number of angles, with steps of 5° , considering an average reflection coefficient for stainless steel of 80%. A value corresponding to approximately four times the volume diameter is obtained.

Fig. 3.3 shows the evolution of the cell constant as a function of radius and height of the excitation (a) and detection (b) volumes. The difference between the two charts is due to the fact that dimensions of the excitation volume affect the interaction length as well. In the excitation volume V_1 , a compromise can be found between radius r_1 and height h_1 , as reducing them too much would result in a stronger resonance, but in a lower interaction length, and vice versa if they are too large. The largest constant is obtained for a radius in the 15 - 20 mm range and a height between 2 and 4 mm, resulting in a thin disc shape.

When detection volume V_2 is considered, on the contrary, the cell constant is highest when both radius r_2 and height h_2 are very small. For instance, changing r_2 from 10 to 25 mm and h_2 from 1 to 5 mm results in a cell

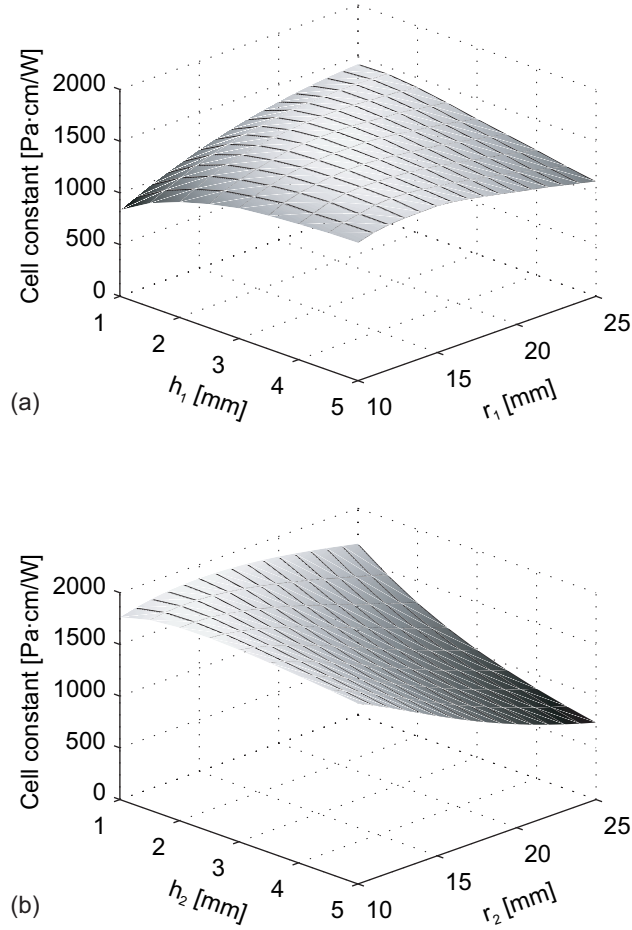


Figure 3.3: Theoretical dependence of the cell constant as a function of radius and height of the excitation (a, with $r_2 = 17.5$ mm, $h_2 = 3$ mm, $a = 4$ mm and $l = 3$ mm) and the detection (b, with $r_1 = 17.5$ mm, $h_1 = 3$ mm, $a = 4$ mm and $l = 3$ mm) volumes. The difference between the two charts is due to the fact that dimensions of the excitation volume affect the interaction length as well.

constant as much as 60% lower. Still, for symmetry reasons and manufacturing simplicity, the decision has been taken to keep the same dimensions for the two volumes.

Concerning the connecting duct, Fig. 3.4 shows clearly that the radius has a higher influence on the cell constant compared to the length; changing the radius from 2 to 6 mm, for instance, results in a 3-fold constant enhancement, while the same variation on the length induces an improvement of only 10%. Therefore, as the surface and volume of the duct have to be much smaller compared to the volumes, the duct will have a disc shape too, with both radius and height of few millimetres.

Mathematical simulation of resonant frequency f_0 as a function of the cell geometry, performed using eq. (2.72), is depicted in Fig. 3.5; within the selected range of values for duct and volumes dimensions, f_0 varies between 2 and 3 kHz, well above the lower boundary of 1 kHz set in the previous paragraph to reduce the influence of acoustic noise.

Final design must take into account the several external elements needed

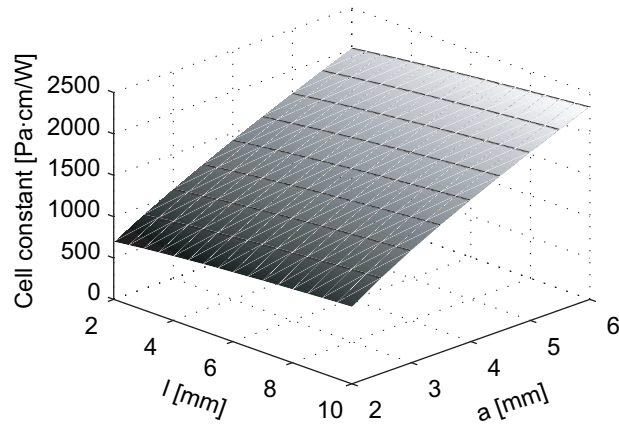


Figure 3.4: Theoretical dependence of the cell constant as a function of radius and length of the duct, considering $r_1 = r_2 = 17.5$ mm and $h_1 = h_2 = 3$ mm. The radius has a much bigger influence on the constant compared to the length.

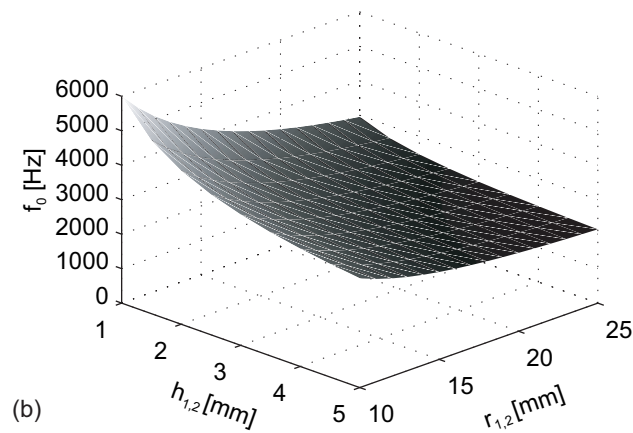
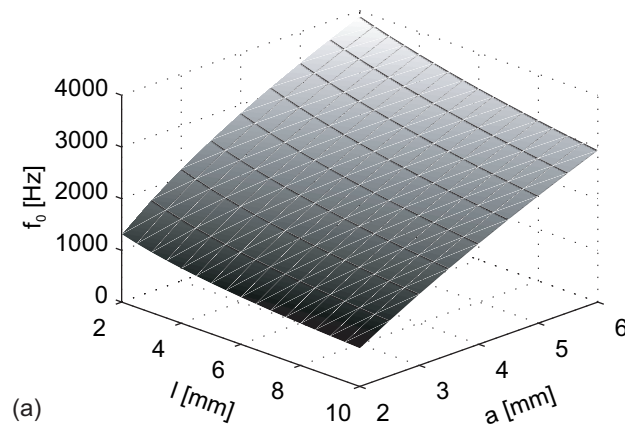


Figure 3.5: Theoretical dependence of the resonant frequency as a function of duct (a, with $r_1 = r_2 = 17.5$ mm and $h_1 = h_2 = 3$ mm) and volumes (b, with $a = 4$ mm and $l = 3$ mm) dimensions. The most influential dimension is observed to be the duct radius.

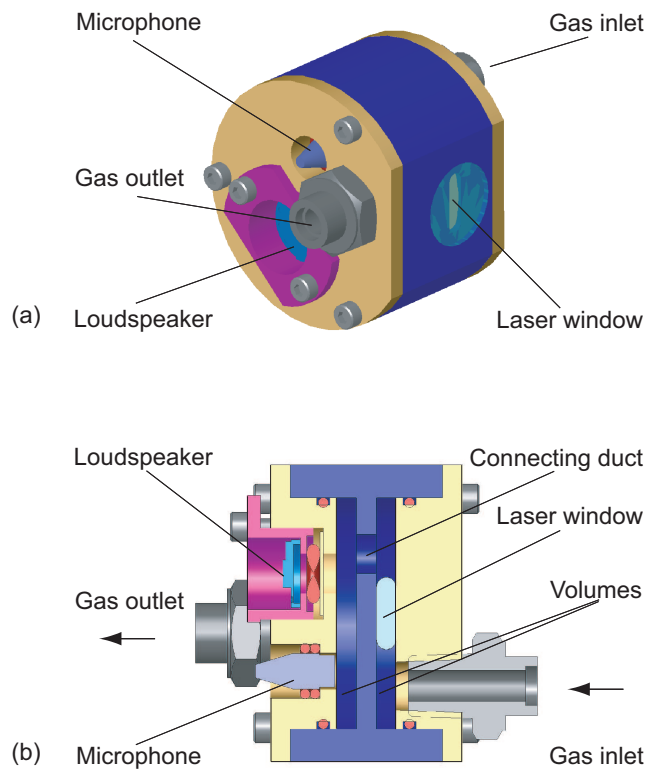


Figure 3.6: Three-dimensional (a) and cross-sectional (b) views of the photoacoustic cell setup. All the external elements are visible in both views, volumes and connecting tube are shown in the cross-sectional view.

in a photoacoustic sensor; the presence of a thin window allowing laser beam injection has already been introduced. Other implemented elements are a microphone to detect the photoacoustic signal, gas inlet and outlet to allow continuous flow measurements, and a loudspeaker, useful to track resonant frequency changes and to perform acoustical characterisation of the cell.

All these elements must be carefully positioned in order to correctly perform their task without affecting the acoustic properties of the resonator and the photoacoustic signal generation. As in the case of the microphone, the loudspeaker will be placed into the detection volume, in order to maximise the available surface for multiple reflection inside the excitation volume, increasing the interaction length between light and gas. Concerning gas inlet and outlet, they are located one per volume, to ensure that the investigated gas passes through the whole cell. In this perspective, position of duct is also very important; it will be shifted with respect to the volumes centre, and this asymmetrically compared to the gas inlet, so that the gas will traverse a path as long as possible inside the excitation volume. The final setup is shown in Fig. 3.6.

Dimensions of the resonator have been chosen taking into account all the described constraints, and with the help of numerical simulations. Following values have been selected:

- Volumes radii r_1 and r_2 : 17.5 mm
- Volumes heights h_1 and h_2 : 3 mm (hence $V_1 = V_2 \sim 2886 \text{ mm}^3$)
- Duct radius a : 4 mm
- Duct length l : 3 mm

In order to leave the possibility to analyse experimentally the influence of the geometrical dimensions on the cell behaviour, the mechanical parts that compose the cell have been designed in order to allow the modification of some dimensions (see § 3.3.3).

According to numerical simulations, the selected values result in the following theoretical cell performances, in air and at room temperature:

- Cell constant C_{cell} : $\sim 1469 \text{ Pa}\cdot\text{cm}/\text{W}$
- Resonant frequency f_0 : $\sim 2661 \text{ Hz}$
- Quality factor Q : ~ 49.8

The chosen dimensions fulfill the physical conditions described in § 3.2.1; in fact, acoustic wavelength at resonance is around 128 mm, hence much bigger compared to the cell size, and the ratio between surfaces and volumes of the duct and of the two volumes is as small as 0.05.

3.3 Characterisation of the photoacoustic cell

3.3.1 Frequency response and improvements of the cell

The initial acoustic cell tests, performed using a loudspeaker excitation, have immediately revealed a strong dependence of the cell performances on some parasitic volumes inside the cell, such as the gas inlet and outlet and the loudspeaker duct. In addition, the cell behaviour is strongly influenced by boundary conditions at gas connections, depending on whether these are open to free space, closed with nuts or connected to pipes. As illustrated in Fig. 3.7, the Helmholtz resonance (a), located as expected in the 2.6 kHz range, is efficiently excited in the case of plugged gas connections, slightly weaker but still at the same frequency for open connections, and eventually very poorly excited and sensibly shifted when pipes are connected to the cell. Furthermore, a second spurious resonance (b), due to the coupling between the cell and the loudspeaker case, is shown in the 1.8 kHz range, and even a third peak (c) appears in the case of open gas connections, resulting from an acoustic coupling between volumes, gas connections and the outer space¹.

While the spurious peaks are far enough from the Helmholtz resonance to not affect its behaviour, the different efficiency of excitation according to the boundary conditions is a serious issue and has to be solved. A good solution is the implementation of silencers at the resonator extremities. Silencers consist in a pipe followed by a buffer volume, to be connected to the gas inlet and outlet; length of both elements must be equal to an odd multiple of a quarter wavelength, the reason being the need of a high acoustic impedance mismatch

¹A cell volume and the duct of a gas connection form a Helmholtz resonator as well.

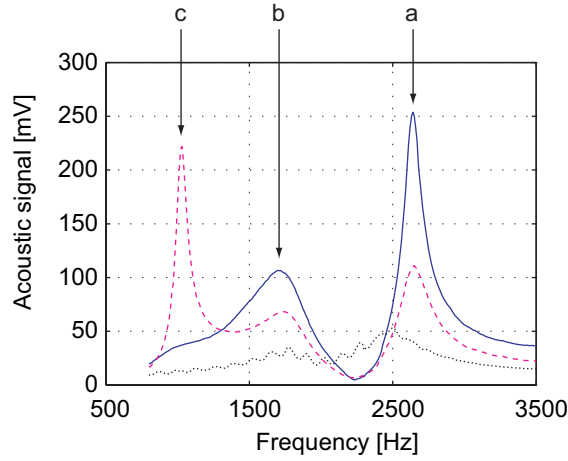


Figure 3.7: Acoustic response of the cell when gas connections are plugged (*solid curve*), open (*dashed curve*) or connected to pipes (*dotted curve*). Arrows designate the Helmholtz resonance (a), a spurious peak due to the loudspeaker case (b), and another spurious peak due to the open gas connections (c).

between cell, pipes and buffer volumes; in this way, acoustic impedance at the junction between cell and gas connections is virtually infinite, and acoustic coupling between them is highly reduced [6]:

$$l_{sil} = (2n + 1) \frac{\Lambda}{4} \quad n = 0, 1, 2, \text{ etc.} \quad [\text{m}] \quad (3.1)$$

As the gas connectors used in the sensor are intrinsically longer than the quarter wavelength (~ 30 mm in this case), pipes have been designed to provide a total length (connection plus pipe) equal to three quarters wavelength, while buffer volumes length is simply equal to a quarter wavelength; finally, pipes internal diameter matches exactly the diameter of the gas connectors (4 mm) in order to simulate a unique regular duct between resonator and buffer volumes, while buffer volumes diameter results from a trade-off between the guarantee of a step impedance change with respect to the pipes and a short response time of the system; a value of 30 mm has been eventually selected (Fig. 3.8).

The effect of silencers is depicted in Fig. 3.9; the boundary conditions at gas connections have no longer any influence on the frequency behaviour of the cell, and curves for plugged, open, or connected gas inlets perfectly overlap. Helmholtz resonance is efficiently excited in all cases and it is well isolated from other spurious resonance peaks; these peaks, appearing at approximately 1.8 and 3.6 kHz, correspond to the two first longitudinal modes of the silencer pipes; additional peak around 1.8 kHz is still due to a parasitic coupling between the loudspeaker case and the cell.

3.3.2 Noise level

Ultimate detection limit of photoacoustic sensors is determined by the lowest detectable pressure change, i.e. by the noise measured by the microphone. This noise results from several contributions, including intrinsic microphone noise, preamplifier noise and ambient acoustic noise. This last contribution

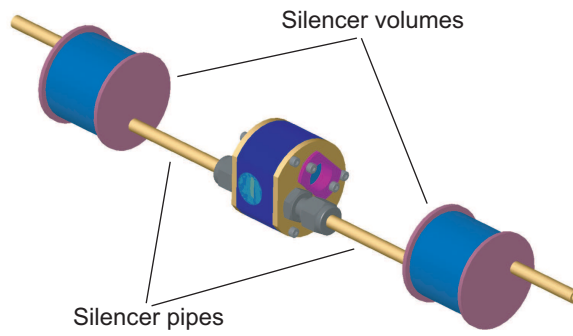


Figure 3.8: Photoacoustic cell setup, including silencers. Pipes length is equal to $3/4 \Lambda$, buffer volumes length is $1/4 \Lambda$.

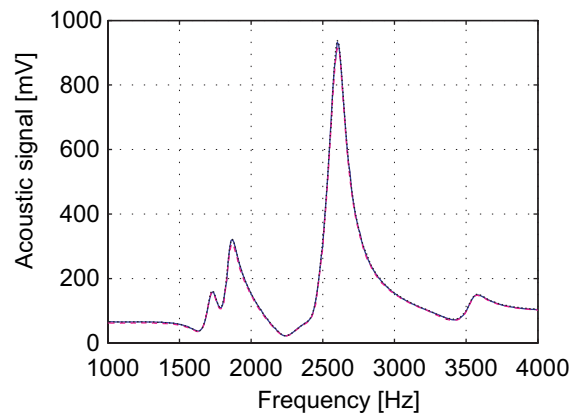


Figure 3.9: Acoustic response of the cell with silencers when gas connections are plugged (*solid curve*), open (*gray dashed curve*) or connected to pipes (*dotted curve*). The three curves perfectly overlap, and the Helmholtz resonance is efficiently excited and isolated from other peaks.

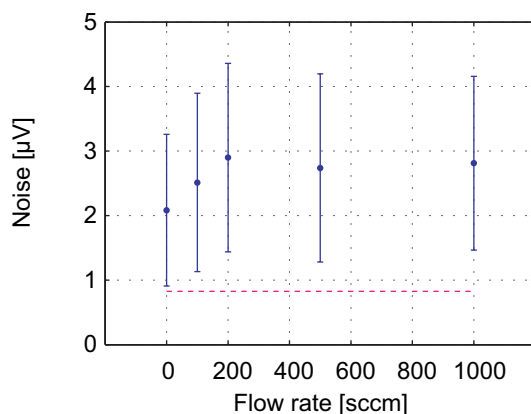


Figure 3.10: Acoustic noise as a function of flow rate. *Circles* represent the measured noise value averaged over 20 minutes with 10 s integration time, *errorbars* correspond to standard deviation of measured signal; *dashed line* represents the microphone and preamplifier noise level, measured in an anechoic room and averaged over 1000 points, with the same integration time. Flow rates up to 1000 sccm have been tested without major effects on the overall noise.

takes into account the noise caused by gas flow inside the cell, usually increasing with higher flows.

In order to ensure a good acoustic isolation from external environment, the photoacoustic cell has been placed inside a wooden chamber, with 22 mm thick walls, whose internal and external surfaces are respectively covered with a wavy absorbing foam (to reduce internal sound reflections), and with a 5 mm layer of Idikell, a lead-based coating, to increase the acoustic isolation. The chamber itself is fixed on four silent blocks (rubber feet with a known stiffness), forming a low-pass mechanical filter with a very low cut-off frequency, so that both ambient acoustic noise and external mechanical vibrations are efficiently filtered out of the chamber.

Contributions from the microphone and the preamplifier were measured in a special anechoic room showing an extremely low ambient noise; subsequently, total noise has been measured as a function of gas flow rate inside the cell, and results are reported in Fig. 3.10; measurements were performed at the resonant frequency, with an integration time of 10 s.

Gas flow seems not to have a large impact on the acoustic noise, which varies from $\sim 2 \mu\text{V}$ to $\sim 3 \mu\text{V}$ when flow increases from 0 to 1000 sccm (standard cubic centimetres per minutes), with a standard deviation slightly lower than $1.5 \mu\text{V}$; contribution from the microphone and the preamplifier is approximately $0.8 \mu\text{V}$.

Noise standard deviation σ_N is a fundamental parameter for photoacoustic sensors characterisation, as the detection limit of a sensor is usually considered to be equivalent to 3 times σ_N .

3.3.3 Photoacoustic characterisation of the cell

First photoacoustic measurements have been performed using methane as test substance, as several properties of this gas make its detection easy and straightforward. In fact, methane shows no problems of adsorption/desorption

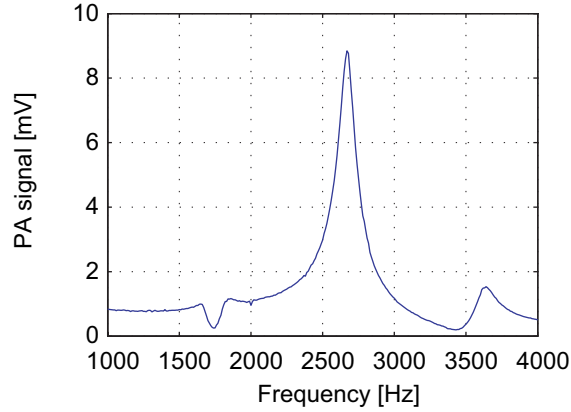


Figure 3.11: Photoacoustic response of the cell filled with 5000 ppm of methane.

Type of excitation	f_0 [Hz]	Q [-]
Acoustic	2611	25.3
Photoacoustic	2668	23.9
Numerical simulation	2661	49.8

Table 3.2: Measured values for resonance frequency and quality factor, in the case of acoustic and photoacoustic excitation, compared with simulations. Values for acoustic measurements and for numerical simulations are obtained in air, values for photoacoustic excitation are obtained in nitrogen.

on cell walls and it is unaffected by relaxation effects, as long as a small percentage of water is present in the buffer gas [7], condition which can be easily achieved in laboratory tests. In addition, CH_4 concentrations as high as 10000 ppm can be used without any risk for human health.

Frequency response of the cell filled with 5000 ppm of CH_4 in N_2 and excited with a suitable laser ($\lambda = 2.37 \mu\text{m}$, $P_0 = 2 \text{ mW}$) has been measured and is illustrated in Fig. 3.11. The modulated laser beam excites the Helmholtz resonance as efficiently as the loudspeaker; longitudinal modes of the silencer pipes are still visible at 1.8 and 3.6 kHz, while the parasitic coupling with the loudspeaker case, observed in the case of a loudspeaker excitation (Fig. 3.9) seems not to be excited in this case, due to the fact that the photoacoustic signal is generated in the opposite volume.

Measured values for resonance frequency (Table 3.2) are in good agreement with simulation values, while quality factor is approximately 2 times lower. This can be explained by the fact that losses inside the volumes are supposed to be negligible compared to losses inside the duct, according to the electrical analogy model used to perform the numerical simulation; this condition is not fulfilled by the designed cell, due to the thin disc shape of the volumes, resulting in an overall increase of viscous and thermal losses.

3.3.3.1 Influence of the variable dimensions

Thanks to a suitable mechanical design, it has been possible to change some dimensions of the cell and analyse the effect on the photoacoustic efficiency

of the sensor. Modifications of duct radius and of volumes height have been accomplished, and the resulting influence on resonance frequency and photoacoustic signal generation has been analysed.

Measured resonant frequencies are in good agreement with theoretical calculations in all cases (Fig. 3.12-3.14 a).

Photoacoustic signal, generated in the same conditions as for frequency response, has been compared to the theoretical cell constant, as it is supposed to be proportional to it. Experimental values trend agrees or differs from the cell constant according to the cases. For instance, when duct radius is increased (Fig. 3.12 b), PA signal follows the same tendency as the cell constant up to a value of 4 mm, then it decreases, most probably because a too large radius does not fulfill anymore the mutual acoustic conditions, described in § 3.2.1, which guarantee the resonant behaviour. When considering the volumes height, in the case of the detection volume (Fig. 3.13 b) there is a good agreement between experimental and theoretical values, while for the excitation volume (Fig. 3.14 b) the trend is similar, but the experimental optimum value is slightly shifted compared to calculations (4.5 mm instead of ~ 3.7 mm); this divergence is probably due to an unprecise estimation of the interaction length l_{path} inside the volume.

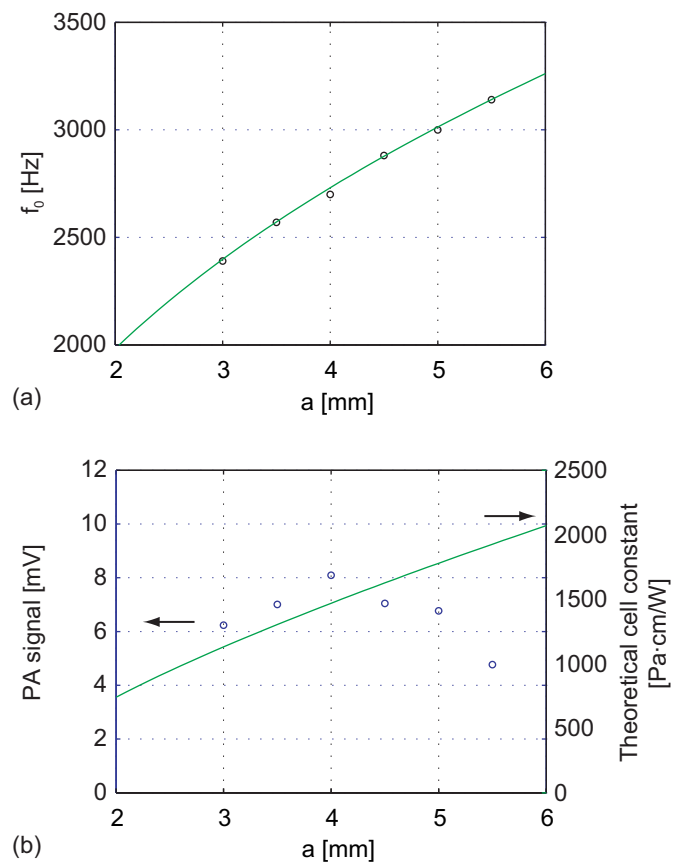


Figure 3.12: Resonance frequency (a) and photoacoustic signal (b) as a function of duct radius a . Circles (left vertical axis in b) are experimental points, solid lines (right vertical axis in b) represent theoretical values. Photoacoustic signal is compared to the simulated cell constant.

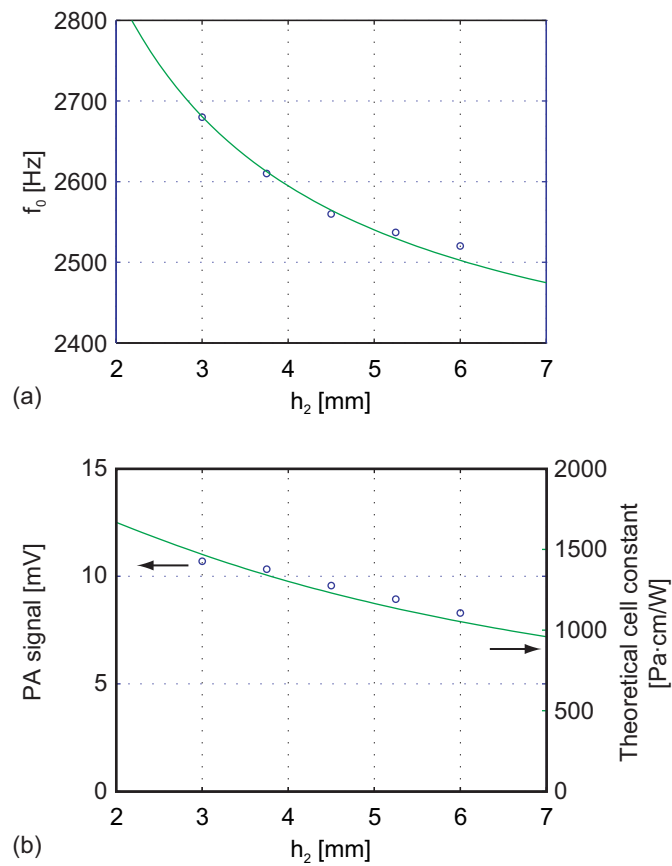


Figure 3.13: Resonance frequency (a) and photoacoustic signal (b) as a function of detection volume height h_2 . *Circles* (left vertical axis in b) are experimental points, *solid lines* (right vertical axis in b) represent theoretical values. Photoacoustic signal is compared to the simulated cell constant.

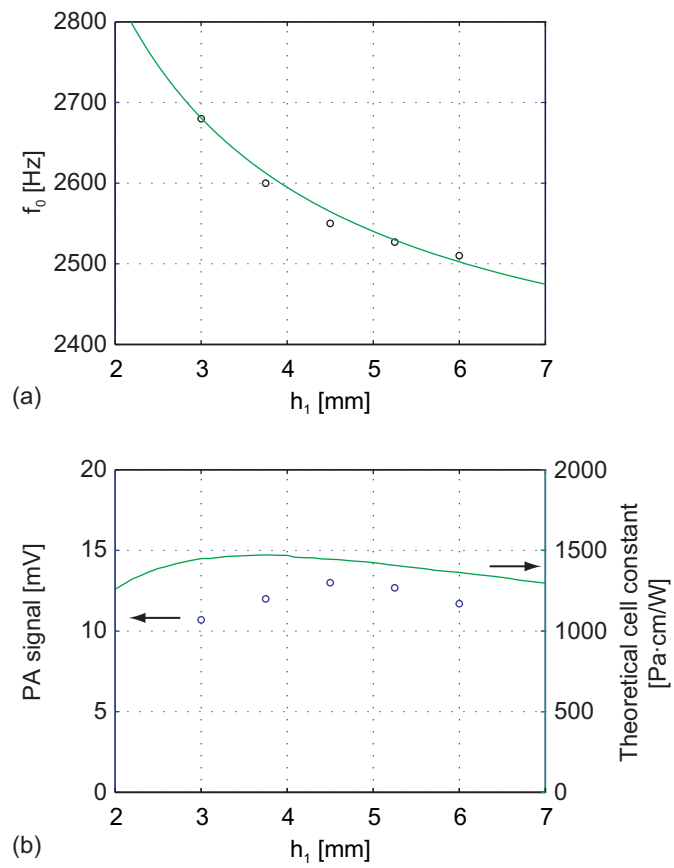


Figure 3.14: Resonance frequency (a) and photoacoustic signal (b) as a function of excitation volume height h_1 . Circles (left vertical axis in b) are experimental points, solid lines (right vertical axis in b) represent theoretical values. Photoacoustic signal is compared to the simulated cell constant.

3.4 Trace gas detection

The developed photoacoustic sensor has been first tested with methane, then optimised to perform ammonia detection at ppm level. In both cases, the following procedure has been applied:

1. Scan of the laser wavelength to measure gas spectrum, and location of the most efficient absorption line.²
2. Optimisation of the modulation scheme in order to maximise the photoacoustic signal.
3. Measurement of the photoacoustic signal as a function of gas concentration, and determination of the detection limit.

Before proceeding to the details of the two measurements, a description of the laser diodes utilised to perform the detection is presented.

3.4.1 Laser characteristics

Sensitive gas analysis involves high requirements on laser properties. First of all, in order to guarantee a good sensing selectivity, a pure single-mode emission is needed, with a high side mode suppression ratio (SMSR). Linewidth of the laser has to be narrow enough to address a single absorption line of the probed gas; as the typical absorption linewidth at ambient pressure and temperature is approximately 2 - 3 GHz (see § 2.2.2), laser linewidth should be at least one order of magnitude lower. Mode hopping-free tuneability is also an important parameter, in order to be able to address several absorption lines, to perform background measurements outside the lines, or to analyse the presence of other gases absorbing in the same region. Finally, when PAS is considered, output power is of the utmost importance as well, as the generated photoacoustic signal is directly proportional to it.

3.4.1.1 Overview of the available sources in the selected spectral region

As introduced in § 3.1, the photoacoustic cell has been designed to suit recently developed antimonide-based semiconductor DFB lasers emitting in the 2 - 2.7 μm region. This spectral window is not reachable using standard semiconductor laser materials (GaAs, InP, etc.), and despite its attractive spectroscopic properties, only few other types of laser sources emit in this wavelength range:

- Chromium-doped chalcogenide lasers ($\text{Cr}^{2+}:\text{ZnSe}$, $\text{Cr}^{2+}:\text{ZnS}$, $\text{Cr}^{2+}:\text{CdSe}$, etc) have been demonstrated to emit in the 2.1 - 2.8 μm range [8, 9], with a considerably high power (several hundreds of milliwatts) and a large tuneability (up to 600 nm); they are optically pumped, therefore they need a high mechanical stability, hence a low technical noise environment, and their linewidth is in the order of few GHz (thus comparable with gases absorption lines), unless frequency selective optical elements

²The most efficient line does not necessarily correspond to the strongest line, as the laser power is not constant all over the scanned spectrum, and a weaker line can be reached with a higher power, resulting in a stronger signal.

are employed. However, despite the large linewidth, photoacoustic spectroscopy using Cr^{2+} doped lasers has been successfully demonstrated [10].

- Difference frequency generation (DFG) sources and optical parametric oscillators (OPO) exploit the nonlinear properties of some crystals (e.g. PPLN, periodically poled lithium niobate) in conjunction with standard NIR lasers, in order to obtain a resulting emission up to the FIR region [11]; both sources show linewidths in the megahertz range, but OPOs have a much higher power (hundreds of milliwatts) compared to DFG lasers (few milliwatts), therefore they are more attractive for PA applications [12]. Still, their intrinsic complexity and their required precise stabilisation make them not suitable for a compact sensor.

None of the other typical MIR sources, such as CO/CO₂ lasers (emitting respectively at 5 - 6 and 9 - 11 μm), quantum cascade lasers (QCL, 4 - 24 μm), or lead salt lasers (4 - 30 μm), can reach the target spectral region [13, 14], making antimonide-based lasers a very interesting source for the development of a compact and portable sensor in the 2 - 2.7 μm range.

3.4.1.2 Characterisation of the antimonide lasers

DFB antimonide-based lasers are very similar to standard semiconductor lasers concerning their spectral properties; a SMSR as high as 30 dB can easily be obtained, and typical linewidths do not exceed 10 MHz [15, 16].

Two different laser diodes have been used in the frame of this work. The first one (laser #1 from now on) was a prototype developed by the Electronics and Microoptoelectronics Lab of University of Montpellier (France) jointly with Nanoplus GmbH (Gebrunn, Germany), while the second (laser #2) was a fully functional diode, provided by Nanoplus GmbH as well; both lasers were obtained within the European project “Gas laser analysis by infrared spectroscopy” (GLADIS³).

The two diodes were housed in standard TO 5.6 windowless packages, with no Peltier cooling, hence temperature stabilisation had to be performed using an external commercial TE-cooled laser mount.

Lasers output power was measured as a function of the injection current at different temperatures ranging from 15°C to 40°C using a thermal powermeter directly mounted in front of the laser, without any collecting optics. The observed threshold current was in the range of 30 - 40 mA for laser #1 and of 20 - 30 mA for laser #2, whereas maximum measured optical powers were respectively 2.6 and 3.4 mW (@ T = 15°C and I = 100 mA), as shown in Fig. 3.15 - 3.16.

Wavelength and tuneability of the lasers were measured as a function of injection current and temperature as well, using a wavemeter with a picometer resolution. Performances of the two lasers were extremely different. Laser #1 (Fig. 3.17) suffered from multimode emission and mode hops, except for a limited range of temperature (30 - 40°C) and current (80 - 100 mA), where a continuous tuneability of approximately 3 nm (2371.2 - 2374.3 nm) was observed, with tuning coefficients of -2.6 GHz/mA (0.048 nm/mA) and -11.2 GHz/°C (0.21 nm/°C).

³Contract IST-2001-35178

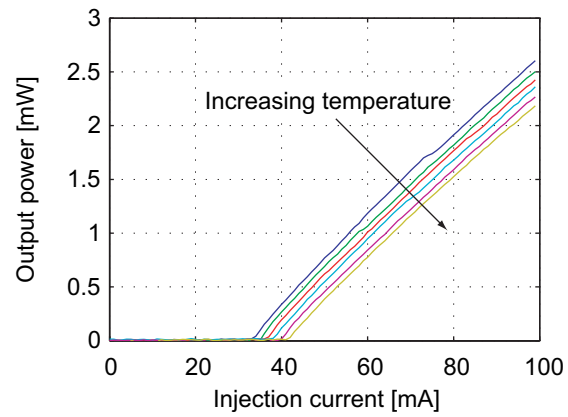


Figure 3.15: Output power as a function of injection current for laser #1 measured at temperatures between 15°C and 40°C with a 5°C step.

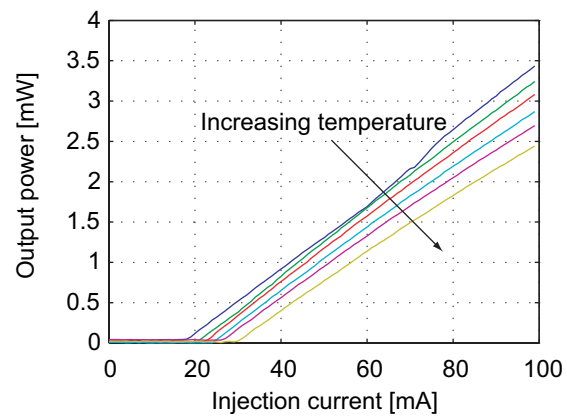


Figure 3.16: Output power as a function of injection current for laser #2 measured at temperatures between 15°C and 40°C with a 5°C step.

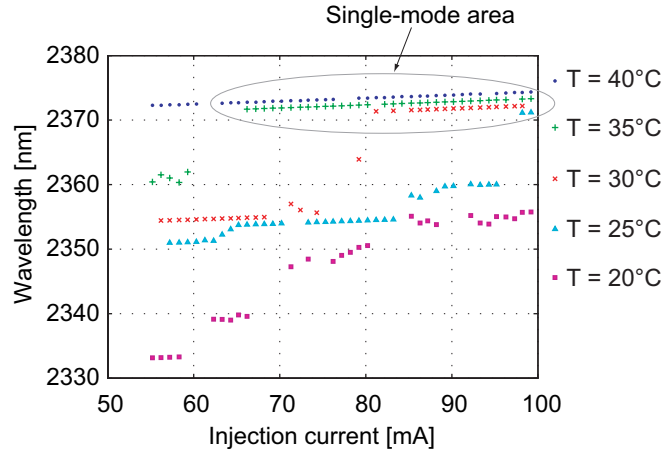


Figure 3.17: Wavelength tuneability of laser #1 measured at different temperatures. Single-mode continuous tuneable emission is observed for temperatures between 30°C and 40°C and currents between 80 and 100 mA

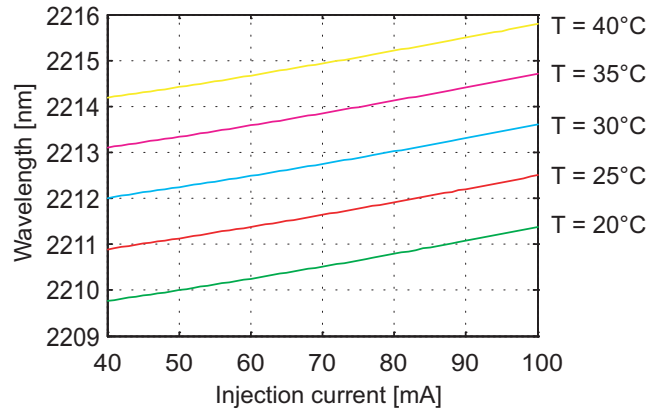


Figure 3.18: Wavelength tuneability of laser #2 measured at different temperatures. Single-mode continuous tuneable emission is observed for the whole range of current and temperature.

Laser #2, on the contrary, showed a nicely continuous tuneability in the whole range of current and temperature, as illustrated in Fig. 3.18. Wavelength could be tuned over 6 nm (2209.8 - 2215.8 nm), with tuning coefficients of -2 GHz/mA (0.032 nm/mA) and -13.5 GHz/°C (0.22 nm/°C). Characteristics of both lasers are summarised in Table 3.3.

3.4.2 Description of the experimental setup

To obtain an efficient coupling of the laser beam inside the photoacoustic cell, this one is mounted on a 3-axes micro-displacement stage and positioned as close as possible to the laser diode, mounted on its external TE-cooling device. Due to the high divergence of the used lasers, alignment of the cell turns out to be uncritical, and the observed photoacoustic signal is independent on the exact relative positions of the cell and the laser diode in a range of approximately 1 mm for both horizontal and vertical directions.

Gas	CH ₄	NH ₃
Operating wavelength [nm]	2371.6	2211.2
Spectral range [nm]	2371 - 2374	2210 - 2216
Temp. tuning [GHz/°C]	-11.2	-13.5
Current tuning [GHz/mA]	-2.6	-2.0
T _{set} [°C]	31.8	15.6
I _{set} [mA]	90	100
Average power [mW]	2	3.4

Table 3.3: Characteristics of the lasers used for trace gas monitoring. T_{set} and I_{set} are the temperature and current operating point of the corresponding laser, respectively. The average power is obtained for the operating conditions at T_{set} and I_{set}.

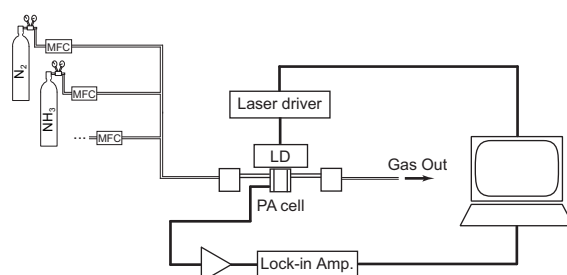


Figure 3.19: Scheme of the experimental setup. Gas concentration is determined by certified gas cylinders connected to mass-flow controllers (MFC). Laser diode (LD) is temperature- and current-controlled through a laser driver. Microphone signal is preamplified and detected with a lock-in amplifier.

Laser temperature and current are controlled through the external mount by a commercial laser driver with respective resolutions of 0.1°C and 0.01 mA, and providing an external modulation input.

Microphone signal is preamplified and detected through a lock-in amplifier with a variable integration time.

Finally, the cell is connected through teflon pipes to a system of mass-flow controllers, which, in turn, are connected to certified cylinders of different gas mixtures, in order to modify the concentration of investigated gases. For instance, when performing ammonia detection, flow from a cylinder of 100 ppm of ammonia buffered in nitrogen is diluted with pure nitrogen from another cylinder, resulting in ammonia concentrations down to few ppm or tenths of ppm.

The experimental setup is illustrated in Fig. 3.19, while Fig. 3.20 shows a picture of the photoacoustic cell positioned in front of the laser mount.

3.4.3 Methane detection

Methane presents its strongest absorption lines in the 3.3 μm region (fundamental $\tilde{\nu}_3$ band), with absorption coefficients higher than 50 cm^{-1} at ambient pressure and temperature; PAS at ppb level has been successfully demonstrated in this band, using an OPO as light source [17]. Second harmonic of this band ($2\tilde{\nu}_3$), located in the 1.65 μm range, is of some interest too, despite its absorption approximately 2 orders of magnitude lower, mainly thanks to

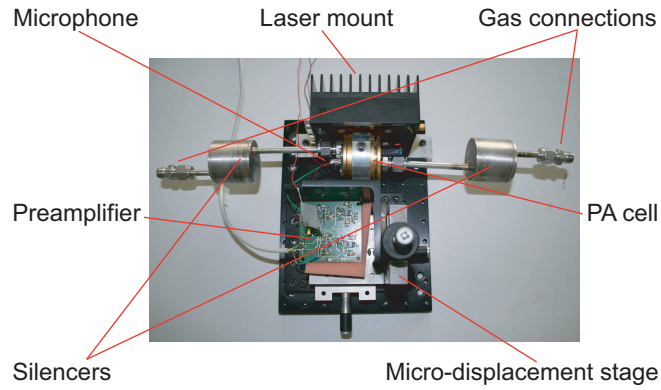


Figure 3.20: Picture of the experimental setup. The cell is positioned as close as possible to the laser diode mount using a micro-displacement stage.

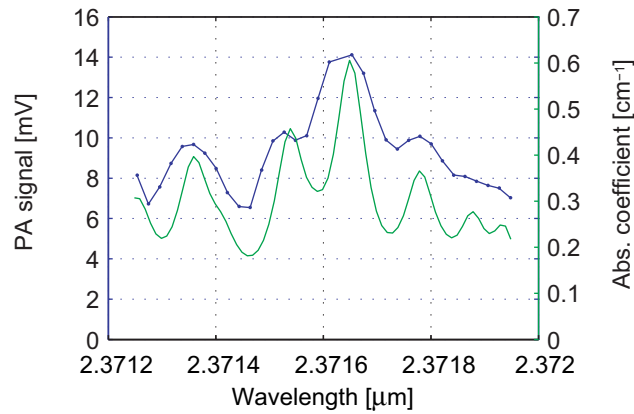


Figure 3.21: Methane spectrum measured with square current modulation (70 ± 30 mA, *solid curve with dots*), for temperatures between 26°C and 30°C , along with calculated spectra from HITRAN database (*solid curve*). Methane concentration is 5000 ppm buffered in nitrogen.

the availability of DFB semiconductor lasers, and absorption lines in this region have been widely used to perform PA detection at sub-ppm level [18, 19].

A third band ($\tilde{\nu}_1 + \tilde{\nu}_4$), whose absorption lines are approximately 50% stronger than at $1.65 \mu\text{m}$, is located around $2.3 \mu\text{m}$, and some lines belonging to this band can be probed by laser #1.

Fig. 3.21 depicts the spectrum of methane obtained by scanning laser temperature between 26°C and 30°C , and by modulating injection current with a square signal of 60 mA around a 70 mA operating setpoint, compared with the spectrum calculated from the HITRAN database [20]. A good qualitative agreement is observed, but the measured spectrum has a slightly reduced spectral resolution. Origin of this problem is to be found in the external temperature stabilisation, which leads to an inefficient heat dissipation in the laser diode, resulting in a slight wavelength shift during the current modulation, and finally in an apparent linewidth broadening and in a poor spectral resolution when performing photoacoustic measurements.

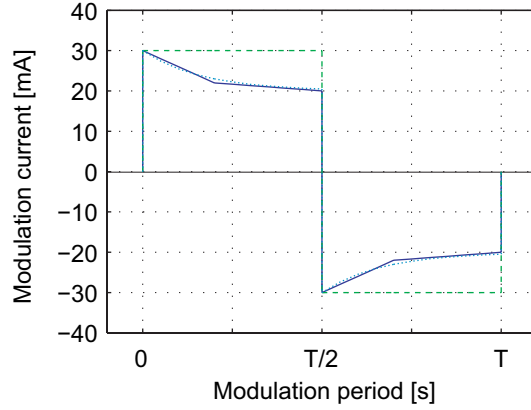


Figure 3.22: Square (*dashed line*) and ramp (*solid line*) modulation currents. Ramp modulation compensates the supposed exponential temperature drift during modulation period (*dotted line*).

3.4.3.1 Improvement of the modulation scheme

The temperature drift during modulation period being supposed to follow an exponential trend, a solution to this problem could be given by a modulation scheme which could compensate the increasing exponential temperature evolution in the laser diode, thus improving the measurement spectral resolution.

Several attempts were tried, and the best results were obtained using an experimentally determined two-slopes ramp (Fig. 3.22), obtained with linear interpolation of the following points:

$$I_{mod} = \begin{cases} 30 \text{ mA} & \text{at } t = 0 & -30 \text{ mA} & \text{at } t = T/2 \\ 22 \text{ mA} & \text{at } t = T/5 & -22 \text{ mA} & \text{at } t = 7T/10 \\ 20 \text{ mA} & \text{at } t = T/2 & -20 \text{ mA} & \text{at } t = T \end{cases} \quad (3.2)$$

Methane spectrum obtained using the described ramp modulation is illustrated in Fig. 3.23. Advantages of this modulation scheme are clearly visible; methane lines are better resolved, and furthermore the corresponding photoacoustic signal is approximately 20% higher, due to the more efficient interaction between laser linewidth and absorption line.

3.4.3.2 Wall noise suppression

Measurement of the photoacoustic signal as a function of the methane concentration is shown in Fig. 3.24. Laser temperature and operating current were set to address the strongest line, selected from measured spectrum, and gas concentration was changed by dilution of methane in nitrogen.

Concentrations down to 5 ppm could be detected, with a perfect linear correspondence between photoacoustic signal and gas concentration, but a strong residual signal was present when methane concentrations fell down to zero.

Origin of this signal is to be found in the interaction between laser light and the cell walls. In fact, as the cell geometry is designed to exploit multiple

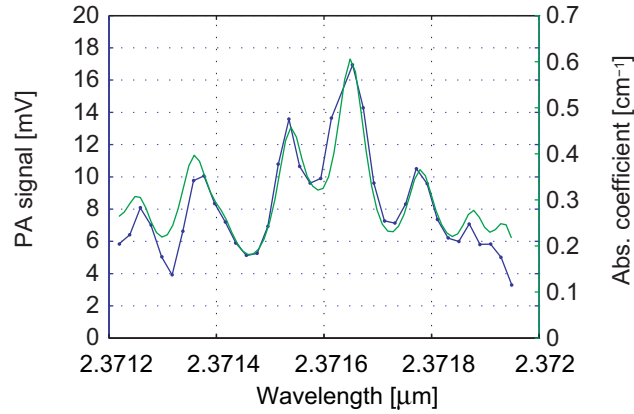


Figure 3.23: Methane spectrum measured with described ramp current modulation, $I_{set} = 70$ mA, for temperatures between 26°C and 30°C (solid curve with dots), compared with calculated spectra from HITRAN database (solid curve). Methane concentration is 5000 ppm buffered in nitrogen.

reflections of the laser beam inside the excitation volume, the light is eventually absorbed by the cell walls after a certain number of reflections; as a consequence, walls are heated and also generate an acoustic wave at the laser modulation frequency. This parasitic sound acts as a noise that induces an offset in the measured acoustic signal.

One way to reduce the importance of this noise is to use appropriate wavelength modulation (WM) instead of intensity modulation (IM). Semiconductor lasers may be intensity- or wavelength-modulated depending on the comparison between operating current and modulation depth [21]. When modulation depth is comparable to operating current, as it is the case in the used ramp modulation (respectively 60 and 70 mA), intensity modulation is dominating; when modulation depth is much smaller than operating current, wavelength modulation becomes prevailing.

The use of WM enables to reduce the effect of wall noise, since wall absorption is wavelength-independent (on a narrow spectral range comparable to the width of a molecular absorption line) and is thus not able to induce an acoustic wave in case of pure laser WM. However, pure WM cannot be achieved when modulating the injection current of a semiconductor laser and residual IM is always present [22], which prevents a total suppression of wall noise.

Still, higher suppression rate may be achieved by combining WM and harmonic detection. In the WM-dominated regime, the generated PA signal is essentially proportional to the derivative of the target absorption line, whereas it is directly proportional to the absorption coefficient in the IM-dominated regime. Furthermore, n^{th} harmonic detection may be performed with WM, which gives rise to an n^{th} derivative of the absorption line. Since IM essentially occurs at the fundamental modulation frequency in a semiconductor laser, second harmonic ($2f$) detection enables to efficiently suppress wall noise, while maintaining a strong PA signal. To efficiently exploit the acoustic properties of the cell, when performing second harmonic detection laser current has to be modulated at half the cell resonant frequency, so that $2f$ signal is matched to the Helmholtz resonance and enhanced by the resonator properties.

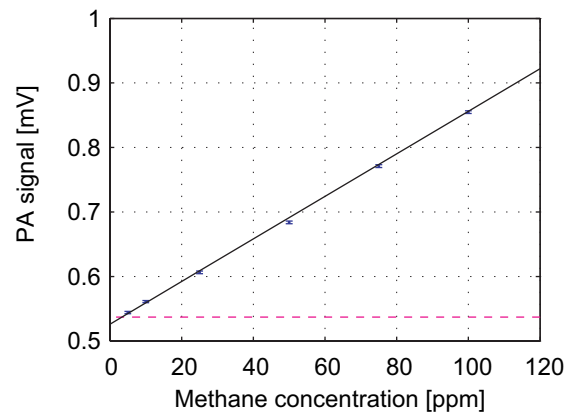


Figure 3.24: Photoacoustic signal as a function of methane concentration using a ramp modulation; *dots* represent measured points, *errorbars* correspond to uncertainty on PA signal, *solid line* is a linear fit, *dashed line* shows the average noise level (photoacoustic signal when gas concentration is equal to zero), which is very high due to walls absorption.

A scan of the probed methane absorption line obtained with wavelength modulation and $2f$ detection is depicted in Fig. 3.25, showing the typical second derivative shape. The measurement is performed using a 10 mV sine signal, with the temperature set at 31.8°C and varying the operating current between 93 and 100 mA, for a total wavelength scan range of 0.3 nm. The effective suppression of wall noise is illustrated in Fig. 3.26, where PA signal obtained with WM and $2f$ detection is shown as a function of methane concentration. Concentrations down to 10 ppm were effectively measured, and a detection limit of 5 ppm (corresponding to average plus 3 times the standard deviation σ_N of the measured signal when gas concentration is equal to zero) with a 10 s integration time is achieved.

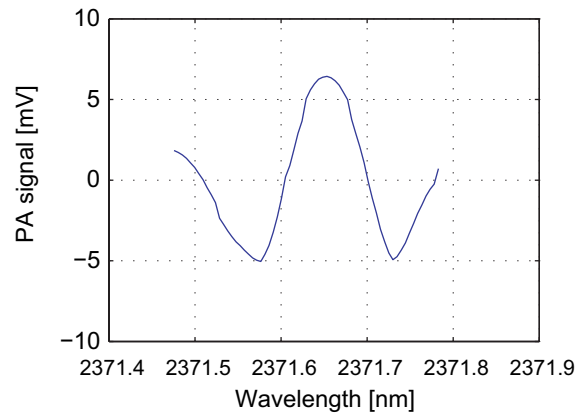


Figure 3.25: Scan of the probed methane absorption line using WM and $2f$ detection. Methane concentration is 100 ppm, modulation depth is 10 mA, laser temperature is 31.8°C , and injection current is scanned between 93 and 100 mA. The typical second derivative shape is observed.

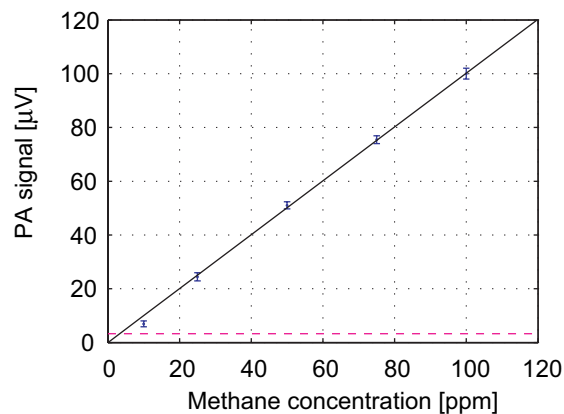


Figure 3.26: Photoacoustic signal as a function of methane concentration using WM and $2f$ detection; *dots* represent measured points, *errorbars* correspond to uncertainty on PA signal, *solid line* is a linear fit, *dashed line* shows the noise level, illustrating the strong reduction of wall noise. A detection limit of 5 ppm ($\text{SNR} = 3$) with a 10 s integration time is achieved.

3.4.4 Ammonia detection

Ammonia sensing at ppm level is the main objective of the first part of this work. Sensing of this molecule is widely implemented in different fields, such as industrial DeNO_x processes [23], clean-rooms [24] or environmental [25] monitoring, or medical breath analysis [26]. Required sensitivity is often in the ppb level, which can be achieved using PAS in conjunction with high power CO₂ lasers [27] or, in the telecom range, with the use of erbium-doped fibre amplifiers [28, 29]. However, for some applications, such as DeNO_x processes, which are widely used in power plants and incinerators to reduce NO_x emissions, a sensitivity in the ppm range is sufficient.

Ammonia strongest absorption lines, due to transitions in the fundamental $\tilde{\nu}_2$ band, are located in the 10 μm region, showing absorption coefficients as high as 80 cm^{-1} at ambient pressure and temperature. Some lines within this region turn out to match emission wavelength of CO₂ lasers, making them a suitable source to perform highly sensitive NH₃ detection [27].

Lines in the telecoms range are mainly due to transitions in the combined $\tilde{\nu}_1 + \tilde{\nu}_3$ and the overtone $2\tilde{\nu}_3$ bands [30], and their absorption coefficients are lower than 0.5 cm^{-1} .

The combined $\tilde{\nu}_2 + \tilde{\nu}_3$ band, whose lines intensity is approximately twice as large as in the telecoms window, is located between 2.1 and 2.4 μm , hence within laser #2 wavelength range.

Fig. 3.27 depicts the spectrum of ammonia obtained by scanning laser temperature between 15°C and 40°C, and by modulating injection current with a 100 mA on-off square signal, compared with the spectrum calculated from the HITRAN database. Two absorption lines, respectively located at 2211.2 and 2213.9 nm, are valid candidates for ammonia sensing. The former has a slightly lower absorption coefficient (0.55 cm^{-1} versus 0.63 cm^{-1} at atmospheric pressure), but it can be reached at a lower laser temperature (for the same injection current), thus with an optical power approximately 20% higher compared to the latter. As the PA signal linearly depends on optical power, the 2211.2 μm line has been finally selected for ammonia detection.

3.4.4.1 Selection of an optimal modulation scheme

As during tests on methane, a strong background wall noise is observed during measurements, and can be seen on Fig. 3.27 between the different detected lines. Effective suppression of this noise has been already demonstrated using wavelength modulation and $2f$ detection in § 3.4.3.2, and the same modulation scheme has been implemented for ammonia sensing.

Laser wavelength is fixed at 2211.2 nm by setting the operating current at 85 mA and the temperature at 21.1°C, and different modulation depths have been tested in order to select an optimum value. Photoacoustic signals obtained for modulation currents from 2.5 to 10 mA are reported in Fig. 3.28, and the highest signal is achieved with a modulation depth of 7.5 mA, corresponding to a ~ 30 GHz scan if considering the tuning coefficient illustrated in Table 3.3.

Theoretical description of photoacoustic $2f$ signal generation with wavelength modulation predicts an optimum modulation depth equal to 2.2 times the absorption linewidth [21], whose typical values at atmospheric pressure and temperature are in the 2-3 GHz range, so that optimum modulation

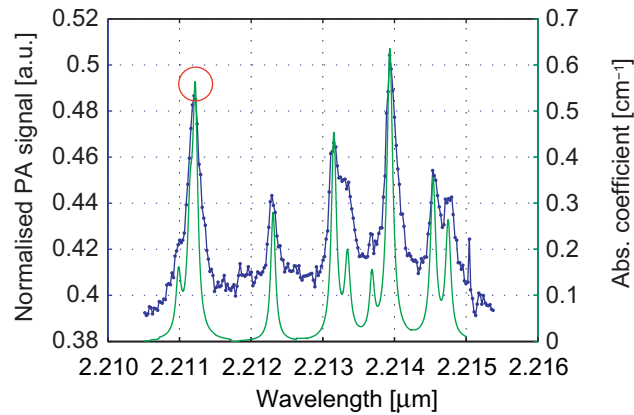


Figure 3.27: Ammonia spectrum measured with square current modulation (between 0 and 100 mA, *solid curve with dots*), for temperatures between 15°C and 40°C, compared with calculated spectra from HITRAN database (*solid curve*). Photoacoustic signal is normalised with respect to laser power. The *circle* indicates the selected line for ammonia sensing. Ammonia concentration is 100 ppm buffered in nitrogen.

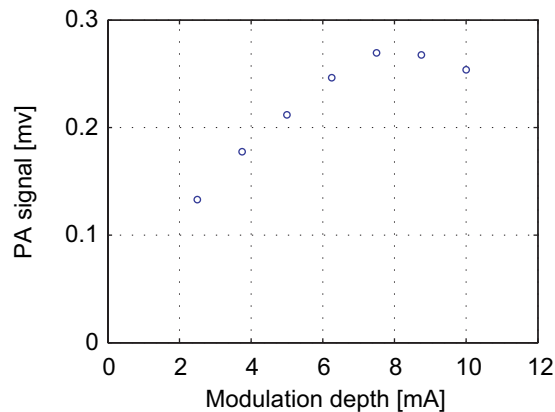


Figure 3.28: Photoacoustic signal for 100 ppm of NH_3 buffered in N_2 as a function of current modulation depth. A maximum value of 0.27 mV for a 7.5 mA modulation current is observed.

depth should not exceed 6 - 7 GHz. Nonetheless, a closer examination of ammonia spectrum reveals that at the selected wavelength two different lines, spaced by 4.5 GHz, are present; these lines are unresolved at ambient temperature and pressure, resulting in a broader line whose total width is approximately 9 GHz, thus requiring a modulation depth around 20 GHz, much closer to the 30 GHz experimentally determined value. The remaining disagreement can be explained by the fact that the laser current tuning coefficient has been measured in static conditions, i.e. changing the operating current step by step; in a dynamic situation, such as when the laser is modulated, this coefficient generally turns out to be smaller, so that the effective wavelength scan is lower than the expected 30 GHz.

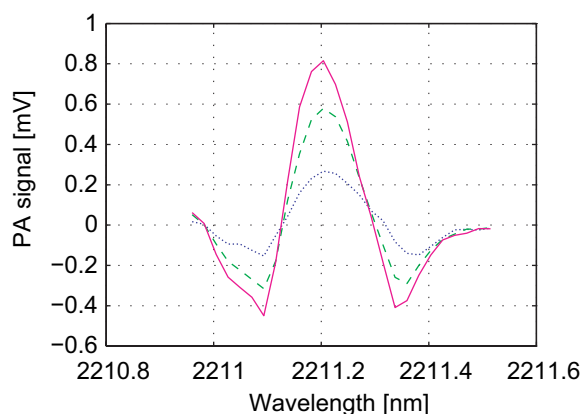


Figure 3.29: Scan of the ammonia absorption line in the stainless steel cell (*dotted curve*), in the golden coated cell (*dashed curve*), and in the same golden coated cell with optimised volume height (*solid curve*). A maximum signal of 0.82 mV is obtained for 100 ppm of NH_3 .

3.4.4.2 Additional improvements of the sensor

All the measurements discussed until this point of the work have been performed using a first cell, made of stainless steel. To improve the efficiency of the photoacoustic sensor, a second cell, made of aluminium and coated with a $5 \mu\text{m}$ thin gold layer, has been implemented, and its performances are discussed in this section.

The use of a gold coating is expected to have a double impact on ammonia detection. On one side, gold has a higher reflection coefficient with respect to stainless steel ($\sim 95\%$ compared to $\sim 80\%$), thus increasing the effective interaction path between light and gas inside the excitation volume; on the other, adsorption/desorption of ammonia molecules on gold is less important than on steel [3], resulting in an improvement of the cell response time.

Fig. 3.29 shows three different scans of the probed ammonia absorption line obtained under different conditions. The use of gold coatings (*dashed curve*) induces an improvement of more than a factor of 2 with respect to the signal generated in the stainless steel cell (*dotted curve*). A further improvement (*solid curve*) is obtained optimising the height of excitation volume, whose influence has already been discussed in § 3.3.3.1, resulting in an overall gain of a factor of 3 when volume height is changed from 3 to 4.5 mm.

The second positive effect of gold coating is illustrated in Fig. 3.30. Response time of the two cells is measured for a 25 ppm change of ammonia concentration and a 1000 sccm flow rate, and results are fitted with an exponential decay. When considering a gas renewal of 95% ($1-1/e^3$), the response time is equal to 3 times the exponential decay constant τ . A decay constant of 37.7 s (i.e. a response time of 113.1 s) is obtained for stainless steel cell, whereas this value is reduced to 19.8 s (59.4 s) for gold-coated cell, showing a 2-fold improvement. Yet, the effect of ammonia adsorption/desorption on the cell walls is not completely suppressed, as decay constant constant obtained for a concentration step of methane, immune from any wall adsorption effect, is 5.4 s (response time of 16.2 s), resulting in a response time 4 times shorter. A coating made of a different material, such as teflon or paraffin [3],

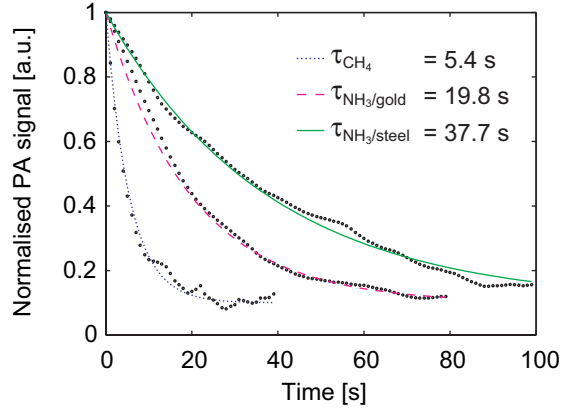


Figure 3.30: Response times of the PA cell to a NH_3 or CH_4 concentration change. Circles represent measured points, solid line and dashed line are the exponential fit for NH_3 concentration respectively in the stainless steel and in the gold-coated cell, dotted line is the fit for CH_4 concentration. Gold coating improves response time for ammonia by a factor of 2, but resulting response time is still 4 times longer compared to methane.

would dramatically reduce this spurious effect, but a sensible loss in terms of photoacoustic signal generation would be obtained as well, as efficiency of multiple beam reflections inside the excitation volume coated with such materials would be extremely lower than in the case of a gold coating.

3.4.4.3 Performances of the sensor

The best performances in ammonia detection have been achieved combining the described $2f$ -WM scheme along with the gold-coated, volume-optimised cell. Photoacoustic signal as a function of NH_3 concentration buffered in nitrogen is illustrated in Fig. 3.31. A photoacoustic calibration coefficient of $8.74 \mu\text{V}/\text{ppm}$ is obtained, and the lowest detectable concentration with an integration time of 10 s is 0.5 ppm. It must be pointed out that the average noise signal (i.e. PA signal with a zero-value gas concentration) is not equal to zero as it would be expected, mainly because the lock-in amplifier used to process the microphone signal operates with an $R - \theta$ detection scheme. This detection scheme delivers separately the magnitude and the phase of the signal, so that the averaged magnitude value is always higher than zero. This value, averaged and evaluated at $2.8 \mu\text{V}$, is summed up to 3 times the noise standard deviation σ_N to obtain the ultimate noise-equivalent signal, quantified at $6.7 \mu\text{V}$, corresponding to the 0.5 ppm detection limit given above.

These results have been obtained using a Knowles EK3132 miniature electret microphone, whose sensitivity M_m , measured in an anechoic room, is evaluated at $70 \text{ mV}/\text{Pa}$, in conjunction with a 100-fold gain (G_m) preamplifier. Taking into account these values, the experimental cell constant C_{cell} can be calculated:

$$C_{cell} = \frac{p}{\alpha_0 P_0 C_{gas}} = \frac{U}{\alpha_0 P_0 C_{gas} G_m M_m} = 853.4 \text{ Pa}\cdot\text{cm}/\text{W}$$

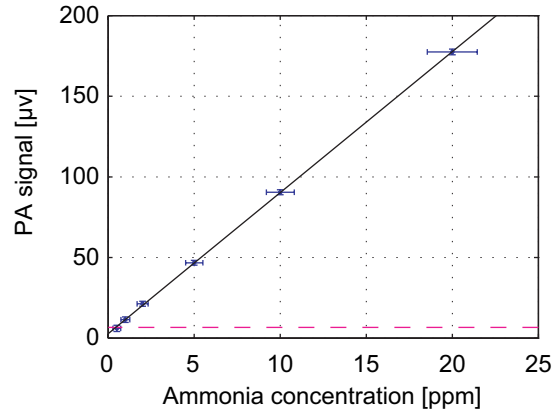


Figure 3.31: Photoacoustic signal as a function of ammonia concentration; *dots* represent measured points, *errorbars* correspond to uncertainty on PA signal (*vertical axis*) and on ammonia concentration (*horizontal axis*), *solid line* is a linear fit, *dashed line* shows the noise level. A detection limit of 0.5 ppm (SNR = 3) with a 10 s integration time is achieved.

This value is approximately 40% lower compared to the theoretical value of 1469 Pa·cm/W given in § 3.2.2, which can be explained by several facts, including the divergence between theoretical and experimental quality factor Q , and the uncertainties on the interaction length l_{path} and on the microphone sensitivity M_m . Moreover, the theoretical calculation of the cell constant considers an intensity-modulated laser power, whereas a wavelength modulation has been used to perform the measurements, furthermore in conjunction with a $2f$ detection scheme.

Sensor performances can be more efficiently described by the ultimate detection sensitivity D , which is defined as follows:

$$D = \frac{\alpha_0 P_0 C_{lim}}{\sqrt{\Delta f}} \quad [\text{W}\cdot\text{cm}^{-1}\text{Hz}^{-1/2}] \quad (3.3)$$

where α_0 is the normalized absorption coefficient of the probed line, P_0 the optical power, C_{lim} the lowest detectable concentration, and Δf the equivalent noise bandwidth, which, according to the lock-in specifications, depends on the integration time τ_{int} and on the slope of the lock-in internal filter. For a 6 dB/octave slope, the following relation is obtained:

$$\Delta f = \frac{1}{4\tau_{int}} \quad [\text{Hz}] \quad (3.4)$$

A lower sensitivity value indicates higher sensor performances. In this case, considering $\alpha_0 = 0.55 \text{ cm}^{-1}$, $P_0 = 2.66 \text{ mW}$, $C_{lim} = 0.5 \text{ ppm}$ and $\tau_{int} = 10 \text{ s}$, a detection sensitivity of $4.62 \cdot 10^{-9} \text{ W}\cdot\text{cm}^{-1}\text{Hz}^{-1/2}$ is obtained. Table 3.4 summarises the sensor performances.

The achieved sensitivity is comparable with typical values found in literature for different kinds of photoacoustic sensors [28, 31, 32, 33, 34, 35], as shown in Table 3.5.

Photoacoustic sensor performances	
α_0 [cm^{-1}]	0.55
P_0 [W]	$2.66 \cdot 10^{-3}$
M_m [mV/Pa]	70
G_m [-]	100
τ [s]	10
$3\sigma_N$ [μV]	6.7
C_{lim} [ppm]	0.5
C_{cell} [Pa·cm/W]	853.4
D [$\text{W} \cdot \text{cm}^{-1} \text{Hz}^{-1/2}$]	$4.62 \cdot 10^{-9}$

Table 3.4: Summary of the photoacoustic sensor performances.

Author	Type of sensor	D [$\text{W} \cdot \text{cm}^{-1} \text{Hz}^{-1/2}$]
This work	Helmholtz	$1.54 \cdot 10^{-9}$
Grossel <i>et al.</i> [31]	Helmholtz	$1.31 \cdot 10^{-9}$
Besson [32]	Longitudinal	$1.17 \cdot 10^{-9}$
Webber <i>et al.</i> [28]	Longitudinal	$1.5 \cdot 10^{-9}$
Meyer <i>et al.</i> [33]	Radial	$1.8 \cdot 10^{-8}$
Hao <i>et al.</i> [34]	Multipass	$6.3 \cdot 10^{-9}$
Kosterev <i>et al.</i> [35]	QEPAS	$5.4 \cdot 10^{-9}$

Table 3.5: Comparison of the sensor performances with other typical photoacoustic sensors. Most of the values found in literature are obtained taking into account 1 time σ_N as the lowest detectable concentration instead of 3 times, hence the values for the sensors described in this work and in [32], calculated considering $3\sigma_N$, have been divided by 3, in order to allow a straightforward quantitative comparison.

Bibliography

- [1] D. A. Yarekha, G. Glastre, A. Pérona, Y. Rouillard, F. Genty, E. M. Skouri, G. Boissier, P. Grech, A. Joullie, C. Alibert, and A. N. Baranov, “High temperature GaInSbAs/GaAlSbAs quantum well singlemode continuous wave lasers emitting near $2.3 \mu\text{m}$,” *Electron. Lett.* **36**(6), 537–539 (2000).
- [2] A. Schmohl, A. Miklós, and P. Hess, “Effects of adsorption-desorption processes on the response time and accuracy of photoacoustic detection of ammonia,” *Appl. Opt.* **40**(15), 2571–2578 (2001).
- [3] S. M. Beck, “Cell coatings to minimize sample (NH_3 and N_2H_4) adsorption for low-level photoacoustic detection,” *Appl. Opt.* **24**(12), 1761–1763 (1985).
- [4] R. Kästle and M. W. Sigrist, “Temperature-dependent photoacoustic spectroscopy with a Helmholtz resonator,” *Appl. Phys. B* **63**(4), 389–397 (1996).
- [5] V. Zéninari, V. A. Kapitanov, D. Courtois, and Y. N. Ponomarev, “Design and characteristics of a differential Helmholtz resonant photoacoustic cell for infrared gas detection,” *Infrared Phys. Technol.* **40**(1), 1–23 (1999).
- [6] F. G. C. Bijnen, J. Reuss, and F. J. M. Harren, “Geometrical optimization of a longitudinal resonant photoacoustic cell for sensitive and fast trace gas detection,” *Rev. Sci. Instrum.* **67**(8), 2914–2923 (1996).
- [7] S. Schilt, J. P. Besson, and L. Thévenaz, “Near-infrared laser photoacoustic detection of methane: the impact of molecular relaxation,” *Appl. Phys. B* **82**(2), 319–328 (2006).
- [8] I. T. Sorokina, E. Sorokin, A. Di Lieto, M. Tonelli, R. H. Page, and K. I. Schaffers, “Efficient broadly tunable continuous-wave $\text{Cr}^{2+}:\text{ZnSe}$ laser,” *J. Opt. Soc. Am. B* **18**(7), 926–930 (2001).
- [9] G. J. Wagner, T. J. Carrig, R. H. Page, K. I. Schaffers, J. O. Ndap, X. Y. Ma, and A. Burger, “Continuous-wave broadly tunable $\text{Cr}^{2+}:\text{ZnSe}$ laser,” *Opt. Lett.* **24**(1), 19–21 (1999).
- [10] C. Fischer, E. Sorokin, I. T. Sorokina, and M. W. Sigrist, “Photoacoustic monitoring of gases using a novel laser source tunable around $2.5 \mu\text{m}$,” *Opt. Laser Eng.* **43**, 573–582 (2005).
- [11] W. D. Chen, J. Burie, and D. Boucher, “Investigation on infrared laser absorption spectroscopy measurement of acetylene trace quantities,” *Infrared Phys. Technol.* **41**(6), 339–348 (2000).
- [12] D. Costopoulos, A. Miklós, and P. Hess, “Detection of N_2O by photoacoustic spectroscopy with a compact, pulsed optical parametric oscillator,” *Appl. Phys. B* **75**, 385–389 (2002).

- [13] F. K. Tittel, D. Richter, and A. Fried, "Mid-infrared laser applications in spectroscopy," in *Solid-State Mid-Infrared Laser Sources*, vol. 89 of *Topics in Applied Physics*, pp. 445–516 (Springer-Verlag, Berlin Heidelberg, 2003).
- [14] M. W. Sigrist, "Trace gas monitoring by laser photoacoustic spectroscopy and related techniques (plenary)," *Rev. Sci. Instrum.* **74**(1), 486–490 (2003). Part 2.
- [15] A. Vicet, D. A. Yarekha, A. Pérona, Y. Rouillard, S. Gaillard, and A. N. Baranov, "Trace gas detection with antimonide-based quantum-well diode lasers," *Spectrochim. Acta A* **58**(11), 2405–2412 (2002).
- [16] S. Schilt, A. Vicet, R. Werner, M. Mattiello, L. Thévenaz, A. Salhi, Y. Rouillard, and J. Koeth, "Application of antimonide diode lasers in photoacoustic spectroscopy," *Spectrochim. Acta A* **60**(14), 3431–3436 (2004).
- [17] A. Miklós, C. H. Lim, W. W. Hsiang, G. C. Liang, A. H. Kung, A. Schmohl, and P. Hess, "Photoacoustic measurement of methane concentrations with a compact pulsed optical parametric oscillator," *Appl. Opt.* **41**(15), 2985–2993 (2002).
- [18] J.-P. Besson, S. Schilt, and L. Thévenaz, "Sub-ppm multi-gas photoacoustic sensor," *Spectrochim. Acta A* **63**(5), 899–904 (2006). Sp. Iss. SI.
- [19] V. Zéninari, B. Parvitte, D. Courtois, V. A. Kapitanov, and Y. N. Ponomarev, "Methane detection on the sub-ppm level with a near-infrared diode laser photoacoustic sensor," *Infrared Phys. Technol.* **44**(4), 253–261 (2003).
- [20] L. S. Rothman, D. Jacquemart, A. Barbe, D. C. Benner, M. Birk, L. R. Brown, M. R. Carleer, C. Chackerian, K. Chance, L. H. Coudert, V. Dana, V. M. Devi, J. M. Flaud, R. R. Gamache, A. Goldman, J. M. Hartmann, K. W. Jucks, A. G. Maki, J. Y. Mandin, S. T. Massie, J. Orphal, A. Perrin, C. P. Rinsland, M. A. H. Smith, J. Tennyson, R. N. Tolchenov, R. A. Toth, J. Vander Auwera, P. Varanasi, and G. Wagner, "The HITRAN 2004 molecular spectroscopic database," *J. Quant. Spectrosc. Radiat. Transf.* **96**(2), 139–204 (2005).
- [21] S. Schilt and L. Thévenaz, "Wavelength modulation photoacoustic spectroscopy: Theoretical description and experimental results," *Infrared Phys. Technol.* **48**(2), 154–162 (2006).
- [22] S. Schilt, L. Thévenaz, and P. Robert, "Wavelength modulation spectroscopy: combined frequency and intensity laser modulation," *Appl. Opt.* **42**(33), 6728–6738 (2003).
- [23] G. Ramis, L. Yi, and G. Busca, "Ammonia activation over catalysts for the selective catalytic reduction of NO_x and the selective catalytic oxidation of NH_3 . An FT-IR study," *Catal. Today* **28**(4), 373–380 (1996).
- [24] S. A. MacDonald, W. D. Hinsberg, H. R. Wendt, N. J. Clecak, C. G. Willson, and C. D. Snyder, "Airborne contamination of a chemically

- amplified resist.1. Identification of problem,” *Chem. Mater.* **5**(3), 348–356 (1993).
- [25] D. Marinov and M. W. Sigrist, “Monitoring of road-traffic emissions with a mobile photoacoustic system,” *Photochem. Photobiol. Sci.* **2**(7), 774–778 (2003).
- [26] L. R. Narasimhan, W. Goodman, and C. K. N. Patel, “Correlation of breath ammonia with blood urea nitrogen and creatinine during hemodialysis,” *PNAS* **98**(8), 4617–4621 (2001).
- [27] S. Schilt, L. Thévenaz, M. Niklès, L. Emmenegger, and C. Hügli, “Ammonia monitoring at trace level using photoacoustic spectroscopy in industrial and environmental applications,” *Spectrochim. Acta A* **60**(14), 3259–3268 (2004).
- [28] M. E. Webber, M. Pushkarsky, and C. K. N. Patel, “Fiber-amplifier-enhanced photoacoustic spectroscopy with near-infrared tunable diode lasers,” *Appl. Opt.* **42**(12), 2119–2126 (2003).
- [29] J.-P. Besson, S. Schilt, E. Rochat, and L. Thévenaz, “Ammonia trace measurements at ppb level based on near-IR photoacoustic spectroscopy,” *Appl. Phys. B* **85**(2-3), 323–328 (2006).
- [30] M. E. Webber, D. S. Baer, and R. K. Hanson, “Ammonia monitoring near 1.5 μm with diode-laser absorption sensors,” *Appl. Opt.* **40**(12), 2031–2042 (2001).
- [31] A. Grossel, V. Zéninari, L. Joly, B. Parvitte, D. Courtois, and G. Durry, “New improvements in methane detection using a Helmholtz resonant photoacoustic laser sensor: a comparison between near-IR diode lasers and mid-IR quantum cascade lasers,” *Spectrochim. Acta A* **63**(5), 1021–1028 (2006). Sp. Iss. SI.
- [32] J.-P. Besson, “Photoacoustic spectroscopy for multi-gas sensing using near infrared lasers,” Ph.D. thesis, Swiss Federal Institute of Technology (2006).
- [33] P. L. Meyer and M. W. Sigrist, “Atmospheric pollution monitoring using CO₂-laser photoacoustic spectroscopy and other techniques,” *Rev. Sci. Instrum.* **61**(7), 1779–1807 (1990).
- [34] L. Y. Hao, J. X. Han, Q. Shi, J. H. Zhang, J. J. Zheng, and Q. Q. Zhu, “A highly sensitive photoacoustic spectrometer for near infrared overtone,” *Rev. Sci. Instrum.* **71**(5), 1975–1980 (2000).
- [35] A. A. Kosterev, F. K. Tittel, D. V. Serebryakov, A. L. Malinovsky, and I. V. Morozov, “Applications of quartz tuning forks in spectroscopic gas sensing,” *Rev. Sci. Instrum.* **76**(4) (2005).

Chapter 4

Differential Helmholtz photoacoustic sensor

The coming chapter is dedicated to the development of a second photoacoustic cell, designed to perform differential measurements.

The motivations for a differential sensor and the related peculiar requirements are approached at first.

An accurate description of the photoacoustic cell design will follow, with a particular stress on the intrinsic differences with regard to the previously described Helmholtz sensor.

Acoustic and photoacoustic characterisation of the cell is then presented, illustrating the encountered difficulty to perfectly fulfill the requirements of a differential sensor.

Finally, some differential measurements on methane and on oxygen are presented; different implemented detection schemes are detailed, and a discussion on the performances of the sensor will conclude the chapter.

4.1 Introduction

Differential photoacoustic spectroscopy is widely reported in literature, the use of differential schemes allowing to obtain an efficient noise reduction and thus to improve the SNR performances of a sensor. The term *differential* is generally referred either to the excitation method (i.e. the same laser beam excites two cells or two different parts of the same cell [1, 2]), or to the detection mode (i.e. two microphones are used, and the difference of their signals provides the actual measurement [3, 4]), or even to a combination of both [5]. In all cases, the purpose is to subtract from the main sought signal an unwanted background, which can consist in any kind of noise, or sometimes in a spurious signal induced by other gases absorbing at the same wavelength.

The photoacoustic sensor described in this chapter is meant to be differential in a third sense: it is designed to provide a signal proportional to the difference between two concentrations of the same gas.

Motivations to design a sensor with these features are linked to a collaboration with the Center for Study of Living Systems at EPFL in the frame of a COST action¹, requesting the development of an instrument to analyse energy expenditure of laboratory animals. This requires the determination of

¹COST B24 Action: *Laboratory animals science and welfare*

the oxygen consumption inside the animals cages, which can be realized by measuring the difference of O_2 concentration between cages inlets and outlets; hence, the development of a sensor providing directly the difference between two gas concentrations, rather than the absolute concentration values, would provide a very convenient tool to perform this kind of laboratory analysis, as a single sensor would be sufficient to provide the desired values instead of two separate standard sensors.

The use of a differential sensor is ulteriorly justified by the very high oxygen concentration in ambient atmosphere, which would result in a strong background signal, hence in a lower precision, when performing absolute measurements, and whose effect would be highly reduced in the case of a differential measurement.

4.2 Design of the differential photoacoustic cell

4.2.1 Motivation and criteria for cell design

The design of this second photoacoustic cell is based on the requirement for a simple and compact sensor providing a differential measurement of two gas concentrations. A configuration based on a Helmholtz resonator, similar to the one described in the previous chapter, is proposed for this application. Helmholtz resonators are intrinsically differential, since, under certain conditions, phases of the acoustic signals in the volumes show a reciprocal π shift [5]; therefore, the photoacoustic signal generated in one volume would be in anti-phase with respect to the signal generated in the other volume, and the signal detected by the microphone, resulting from the two contributions, would be equal to their difference; hence, if each volume is filled with a different concentration of a given gas, the resulting photoacoustic signal would be proportional to the difference of the two concentrations, and eventually fall to zero when the concentrations in the volumes are identical.

The main issue of this configuration is to physically separate the two volumes, in order to avoid mixing the gas compounds, without affecting the acoustic behaviour of the cell, in terms of resonance enhancement and of phase shift. The proposed solution consists in a thin stretchable membrane located midway in the connecting duct; this membrane, whose main role is to reciprocally seal the volumes, should be tuned, through stretching, at the same resonant frequency as the cell in order to preserve the resonator gain and not to add any spurious phase shift between the volumes.

The geometric design of the cell depends primarily on the need for an uniform optical power distribution between the two cell volumes, as photoacoustic signals generated separately in each volume have to be of the same intensity; this requirement can only be achieved if the laser beam is collimated and successively split in two arms of the same power, each one illuminating a volume of the cell; therefore, unlike in the first sensor, the laser light will not be coupled directly into the photoacoustic cell, and some bulk optic elements (beam splitters, mirrors, etc.) will be integrated in the experimental setup (Fig. 4.1).

A key point of the sensor design is the choice of the resonant frequency. As described in § 2.3.1.1, intensity, phase and linearity of a photoacoustic signal can be sensibly affected by relaxation effects when deactivation process

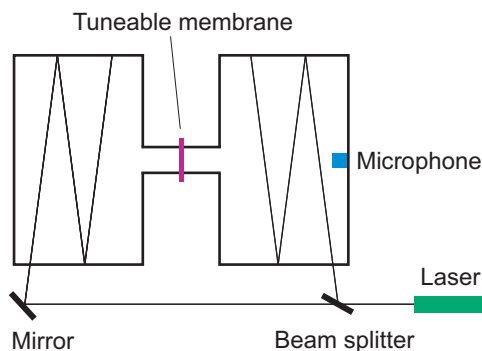


Figure 4.1: Scheme of the differential resonator. Laser light is split in two arms, each one illuminating a volume of the cell. The membrane separates gases in the chambers. Signals generated in the volumes are π -shifted at microphone location.

of excited molecules of the probed gas is slow enough to be comparable with the modulation period of the laser. For instance, when oxygen is considered, relaxation rates through collisions with nitrogen and oxygen itself, the main two components of ambient air, are very low (respectively 40 s^{-1} and 63 s^{-1} at atmospheric pressure), while deactivation process with water vapour is very fast ($1.1 \cdot 10^6 \text{ s}^{-1}$ at atmospheric pressure) [6]. The global oxygen relaxation rate is given by eq. (2.37), where C_k is the concentration of the molecule M_k and $\tau_{M_j-M_k}^{-1}$ the relaxation rate of molecule M_j through collisions with molecule M_k :

$$\tau_{O_2}^{-1} = C_{O_2} \tau_{O_2-O_2}^{-1} + C_{N_2} \tau_{O_2-N_2}^{-1} + C_{H_2O} \tau_{O_2-H_2O}^{-1} \quad [\text{s}^{-1}] \quad (4.1)$$

For typical ambient air concentrations of nitrogen (78%), oxygen (21%) and water vapour (1.15%), the resulting oxygen relaxation rate at $p = 1 \text{ atm}$ is approximately 11000 s^{-1} ; hence, to guarantee enough time for the deactivation process to be completed within one modulation period of the laser², modulation frequency must be kept well below 1 kHz. On the other hand, it is generally unadvised to use a too low operating frequency because of the ambient acoustic noise, which is widely known to be inversely proportional to frequency. A trade-off value range around 500 Hz has been selected.

Finally, the choice of the cell material is of a lesser importance in this second cell, as the target substances are not expected to show problems of wall adsorption, and probed concentrations would in any case be high enough to neglect any adsorption effect. As the quality of the acoustic resonance is directly influenced by the surface roughness of the cell internal walls³, an electrochemically polished quality of stainless steel has been selected.

On the contrary, choice of the membrane material is more critical, as it directly affects the membrane resonant frequency; investigated materials and their properties are discussed in detail in the following section.

²This condition can be written as $\omega\tau \ll 1$, hence $f \ll \tau^{-1}/2\pi = 1.75 \text{ kHz}$.

³A high surface roughness causes an increase of viscous losses, hence a poorer resonance quality factor.

Material	E_Y [MPa]	μ [-]	ρ [kg/m ³]	ϵ_{min} [mm]	f_0 [Hz]
NR/SBR	1.47	0.5	1.01	0.5	309
NBR	9.24	0.5	1.40	0.3	394
LDP	11.7	0.46	0.92	0.5	935

Table 4.1: Characteristics of some investigated materials for the membrane. E_Y is the Young's modulus, μ the Poisson's ratio, ρ the density, ϵ_{min} the thinnest commercially available thickness and f_0 the expected resonant frequency for a membrane of 1 cm of diameter. NR/SBR stands for Natural Rubber/Styrene Butadiene Rubber, NBR for Nitrile Butadiene Rubber, LDP for Low Density Polyethylene.

4.2.2 Design of the differential photoacoustic cell

The design of this second photoacoustic cell results from a trade-off between high cell constant, low resonant frequency, physical limitations and technical constraints, mainly concerning the membrane design. Overall target size is to be kept within 10 - 15 cm to guarantee a small and compact sensor, and geometric dimensions are chosen on account of their influence on the acoustic and photoacoustic behaviour of the cell.

Design of the duct, beside fulfilling the acoustical conditions, has to take into account the availability of a membrane resonating in the 500 Hz range, which is difficult to achieve for diameters in the centimetre range. In fact, given a round plate of diameter d and thickness ϵ , fixed along its circumference, the fundamental resonant mode is [7]:

$$f_{m0} = 1.868 \frac{\epsilon}{d^2} \sqrt{\frac{E_Y}{\rho(1 - \mu^2)}} \quad [\text{Hz}] \quad (4.2)$$

where E_Y is the Young's modulus of the material (a measure of its stiffness), ρ its density, and μ its Poisson's ratio (ratio between normal and axial strain when a load is applied; in most cases its value is between 0 and 0.5). Young's modulus is expressed in Pa, its value ranges from few tens of megapascal (rubber) to few gigapascal (polyethylene, nylon) up to hundreds of gigapascal (metals), and it is generally difficult to estimate its precise value because it strongly depends on the exact composition of the material.

Low density polyethylene and different sorts of rubbers have been investigated, on account of their relatively low Young's modulus and their availability in form of thin films, and their main characteristics are summarised in Table 4.1; a commercially available 0.5 mm film of NR/SBR⁴ rubber ($E_Y = 1.47$ MPa, $\rho = 1010$ kg/m³, $\mu = 0.5$) has been eventually selected. For a membrane made of this material, with a typical diameter of 1 cm, the fundamental resonant mode is predicted at 309 Hz.

The constraint of a relatively large duct radius, needed to achieve a membrane resonant frequency lower than 500 Hz, leads to a duct surface and volumes no longer negligible with respect to cell volumes size; therefore, a slightly more complex model has been used to simulate the cell behaviour, including a supplementary acoustic mass in series with the capacitors (Fig. 4.2).

⁴NR/SBR stands for Natural Rubber/Styrene Butadiene Rubber, the components of the selected material.

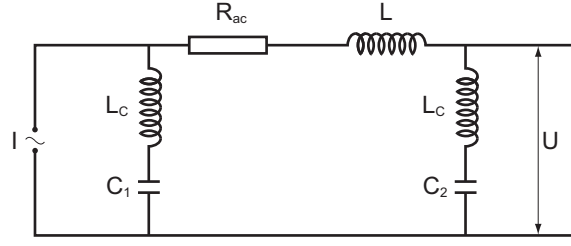


Figure 4.2: Electrical analogy of a Helmholtz resonator whose duct has a volume and a surface not negligible compared to the volumes dimensions.

Value of this acoustic mass, named L_C , is given by [7]:

$$L_C = 0.27 \frac{\rho}{a} \quad [\text{Pa} \cdot \text{s}^2 / \text{m}^3] \quad (4.3)$$

Prediction of the cell constant and of the resonance frequency as functions of the geometrical dimensions of the cell, calculated according to this extended model, are reported in Fig. 4.3 and 4.4. Resonance frequency is directly proportional to the duct radius and slightly inversely proportional to its length (Fig. 4.3 b), whereas the cell constant shows a local maximum for a duct radius of approximately 4-5 mm; for higher radii, the mutual conditions between duct and volumes are no longer respected, and the efficiency of the resonator is lowered (Fig. 4.3 a). Volumes length shows a very light influence on resonance frequency, and no influence at all on the cell constant, as its effects on the interaction path and on the chamber volume compensate reciprocally; finally both the cell constant and the resonance frequency are inversely proportional to volume radius (Fig. 4.4).

As the laser beam is collimated, the most efficient shape for the cell volumes consists in long but narrow cylinders whose longitudinal axis coincides with the propagation axis of the laser light. To increase the interaction path length, multiple beam reflections inside the volumes are implemented: mirrors are located at one extremity of the cylinders, and windows at the other; these windows are suitably silver-coated on most of their internal surface, except on a small opening section to let the laser beam enter the cell (Fig. 4.5); in this way, high quality reflections are obtained on both sides of the volumes, and interaction length is augmented.

Concerning the external elements, the decision has been taken to include two microphones and two loudspeakers (one of each per volume), in order to allow a more detailed characterisation of the cell, and to keep symmetry in the sensor. Volumes are supplied with two gas connectors, in order to be able to inject a different gas flow and mixture in each volume. The final setup is shown in Fig. 4.6. After several simulations, and taking into account all the constraints, the following values have been selected for the cell dimensions:

- Volumes radii r_1 and r_2 : 10 mm
- Volumes heights h_1 and h_2 : 80 mm (hence $V_1 = V_2 \sim 25133 \text{ mm}^3$)
- Duct radius a : 5 mm
- Duct height l : 80 mm

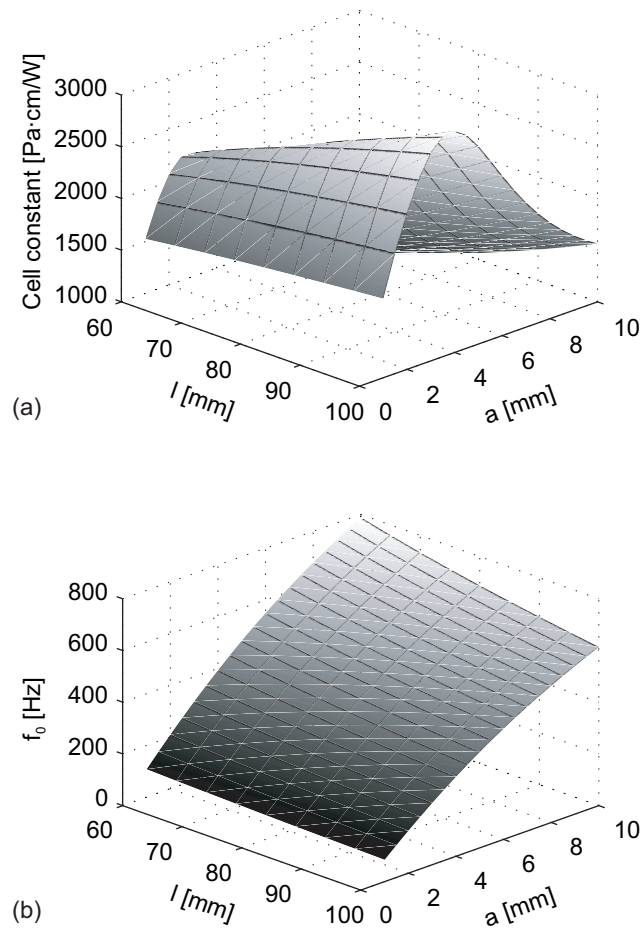


Figure 4.3: Theoretical dependence of the cell constant (a) and of the resonant frequency (b) as a function of duct dimensions, considering $r_1 = r_2 = 10$ mm and $h_1 = h_2 = 80$ mm. The cell constant shows optimum values for a radius of 4-5 mm.

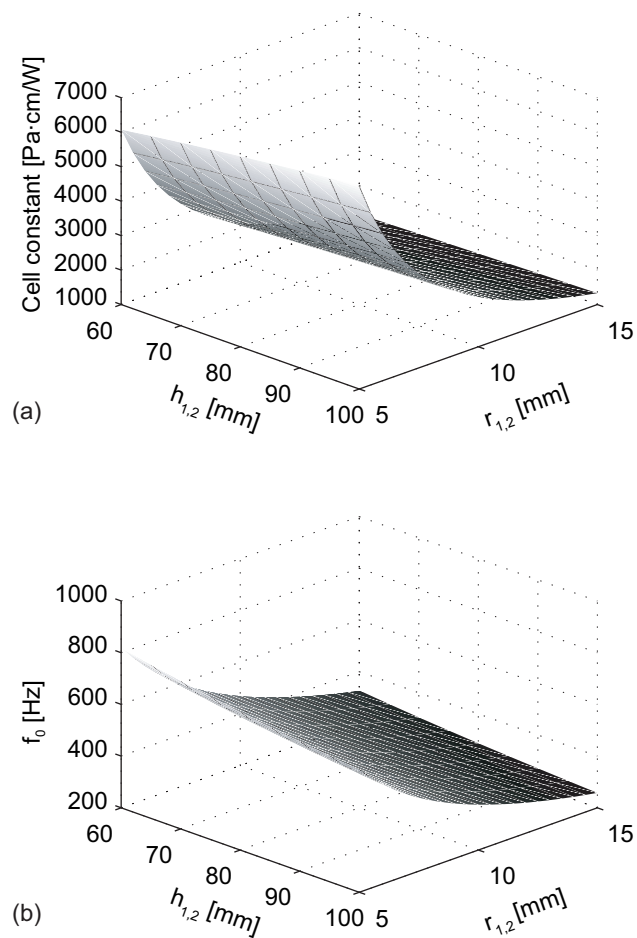


Figure 4.4: Theoretical dependence of the cell constant (a) and of the resonant frequency (b) as a function of volume dimensions, considering $a = 5$ mm and $l = 80$ mm. Both quantities decrease with higher volume radii and are less affected by volume length.

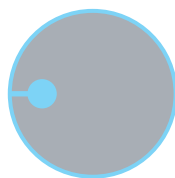


Figure 4.5: Silver-coated window located at volumes extremities. The windows has a 22.4 mm diameter, the laser inlet section a 5 mm diameter. The small uncoated segment beside this section results from coating process.

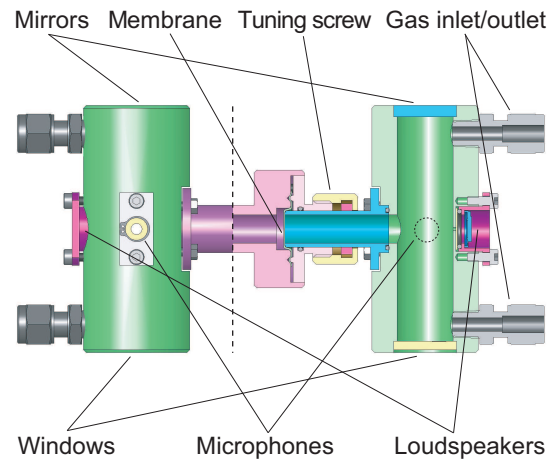


Figure 4.6: Differential photoacoustic cell setup. *Left side* of the dashed line is a top view of the cell, *right side* is a cross-sectional view. All the external elements of the cell are visible. The membrane can be tuned by adjusting the apposite screw.

The resulting mutual condition between duct and volumes are taken into account by the extended model; all other physical conditions are fulfilled, as acoustic wavelength at resonance is above 0.8 m, hence more than 10 times higher than any dimension of the cell.

Simulations provide a Helmholtz resonance frequency of 409 Hz, and a membrane fundamental resonance of 309 Hz. This value will be shifted towards higher frequencies until it matches the resonance of the cell by tightening the membrane through a suitable tuning system, consisting in a screw that induces a longitudinal movement in a pipe to stretch the membrane. A cell constant of 1461 Pa·cm/W and a quality factor of 37.8 are simulated, although these value do not take into account the effect of the membrane.

Further simulations have been performed to predict the frequency and phase behaviour of the cell in both volumes, and calculated curves are depicted in Fig. 4.7. The simulated acoustic signals in the volumes show the same trend around the resonance, though their behaviour is slightly different for lower and higher frequencies; phase shift between the signals at the resonance is estimated at approximately 170° .

The reason for not reaching an exact π shift is to be found in the presence of thermal and viscous losses inside the cell; these losses smooth the phase steps observed inside the volumes at resonance, hence the difference between phases tends to an asymptotic value of π , but it concretely reaches it only at higher frequencies, far from the resonance.

4.3 Characterisation of the differential cell

4.3.1 Frequency and phase response

Frequency and phase behaviour of the sensor excited by the loudspeakers have been measured in the same and in the opposite volume with respect to the excitation. Loudspeakers have been alternatively frequency-scanned between 200 and 600 Hz, and magnitude and phase of the resulting microphone signals

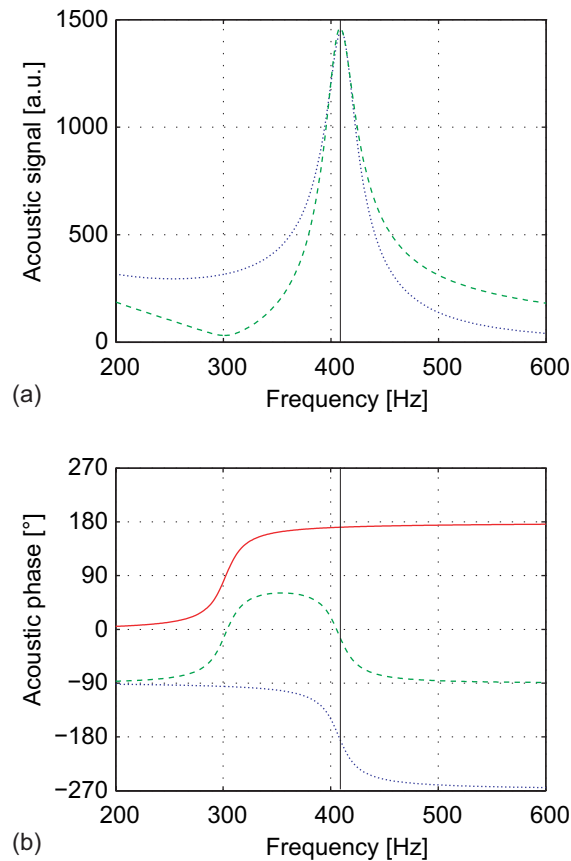


Figure 4.7: Simulation of the frequency (a) and phase (b) behaviour of the differential cell. *Dashed curves* represent calculations for an excitation in the *same* volume as the detection, *dotted curves* the calculations for an excitation in the *opposite* volume. *Solid line* in the phase graph illustrates the phase difference between the two volumes, which tends to π . The *vertical line* shows the resonant frequency location.

are reported in Fig. 4.8. Measured magnitudes follow the same trend as the theoretical simulations shown in Fig. 4.7 a, the slight difference between the two peaks values being due to the fact that the two loudspeakers are not exactly identical. Observed resonance frequencies are respectively 421 and 419 Hz, suggesting the presence of small asymmetries between the volumes, whereas quality factors Q are evaluated at 19.6 and 19.5, approximately 50% of the theoretical value of 37.8, indicating an apparent under-estimation of the losses in the model used for simulations.

When phases are considered, a qualitative agreement with expected trends is observed as well, but the reached phase shift at the resonance frequency is far from the expected π value, reaching only 140° , owing to losses inside the cell, as explained in the previous section.

4.3.2 Influence of the membrane

Measurements illustrated in § 4.3.1 have been repeated, in the same conditions, with the membrane mounted midway in the connecting duct and properly tuned. Observed curves are shown in Fig. 4.9. The main difference with measurements obtained without membrane concerns the signal magnitudes,

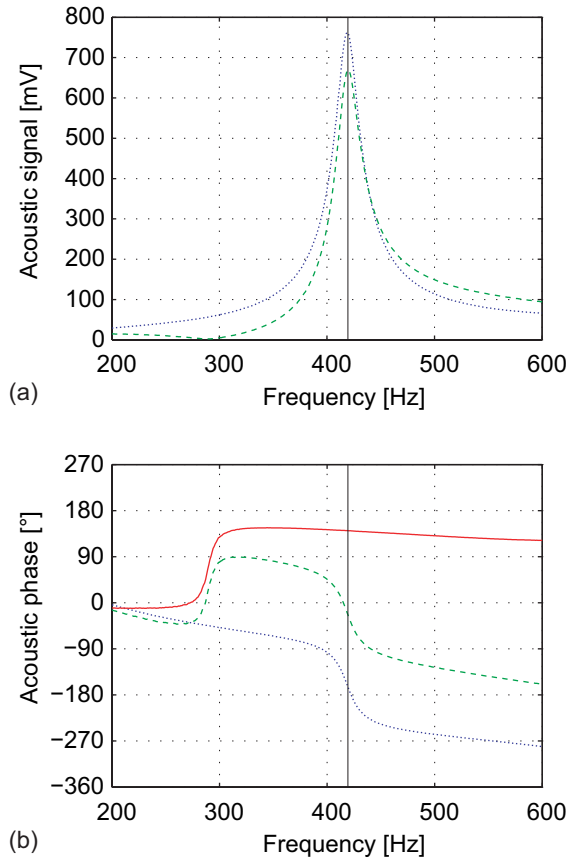


Figure 4.8: Measured frequency (a) and phase (b) behaviour of the differential cell without membrane in the case of an acoustic excitation. *Dashed curves* represent measurements for an excitation in the *same* volume as the detection, *dotted curves* measurements for an excitation in the *opposite* volume. *Solid line* in the phase graph illustrates the phase difference between the two volumes, which, at the resonant frequency (indicated by a *vertical line*) is equal to 140° .

which are approximately 60% lower, due to the significant acoustic losses induced by the membrane.

The resonance of the membrane completely overrides the Helmholtz resonance, due to its sensibly higher acoustic impedance, and therefore no evidence of mode coupling is observed. This is confirmed by the fact that, when tightening or loosening the membrane to reach higher or lower resonant frequencies, the Helmholtz resonance does not appear to be excited.

Resonant frequencies measured when exciting the same or the opposite volume with respect to the microphone are respectively 421 and 417 Hz with quality factors of 26 and 26.8, which confirm the presence of some asymmetries between the volumes. Hence the membrane induces a slight improvement in the quality factor, probably due to the fact that the membrane resonance shows a higher efficiency with respect to the resonance of the cell.

Phase behaviour at the resonance is similar to the configuration without membrane, and the observed phase shift reaches a value of 145° in the range between the two measured resonance frequencies.

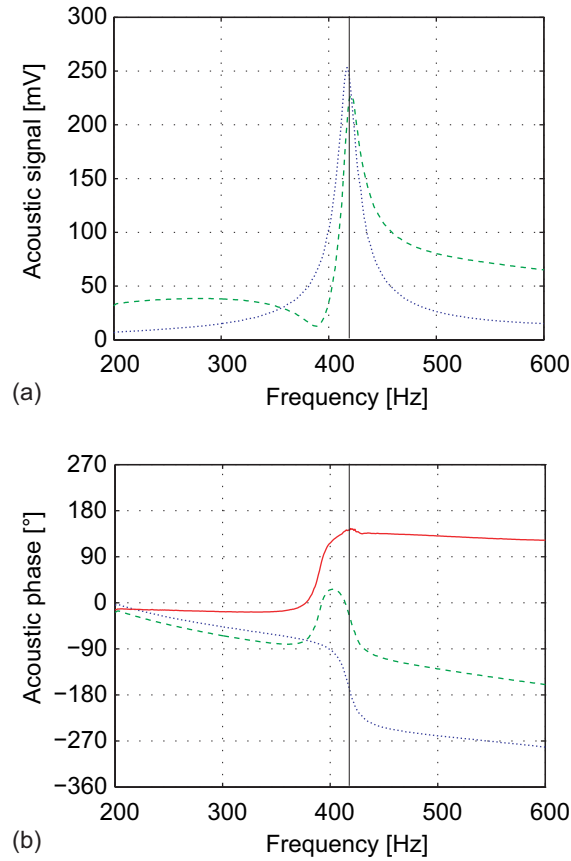


Figure 4.9: Measured frequency (a) and phase (b) behaviour of the differential cell with the tuned membrane in the case of an acoustic excitation. *Dashed curves* represent measurements for an excitation in the *same* volume as the detection, *dotted curves* measurements for an excitation in the *opposite* volume; resonant frequencies show a 4 Hz shift. *Solid line* in the phase graph illustrates the phase difference between the two volumes, which, at an average values between the two resonant frequencies (indicated by a *vertical line*) is equal to 145° .

4.3.3 Photoacoustic characterisation of the cell

As in the case of the first cell, photoacoustic characterisation of the differential cell has been performed using methane as a test gas, to benefit from stronger absorption coefficients (approximately 0.5 cm^{-1} at $1.65 \mu\text{m}$ for CH_4 , compared to $1 \cdot 10^{-3} \text{ cm}^{-1}$ at 760 nm for O_2), and from the availability of a relatively high power ($\sim 15 \text{ mW}$) DFB laser emitting at the desired wavelength, as detailed in § 4.4.1.

The laser beam is collimated and passes through a suitable beam splitter, and the resulting two arms are injected in the cell through the apposite windows (see Fig. 4.1).

Frequency and phase behaviour of the cell has been measured by filling both volumes with a methane concentration of 5000 ppm buffered in nitrogen, by scanning the laser modulation frequency between 200 and 600 Hz and by alternatively blocking one of the two beams to enter the cell, in order to obtain a separate characterisation curve for each volume. Results are illustrated in Fig. 4.10.

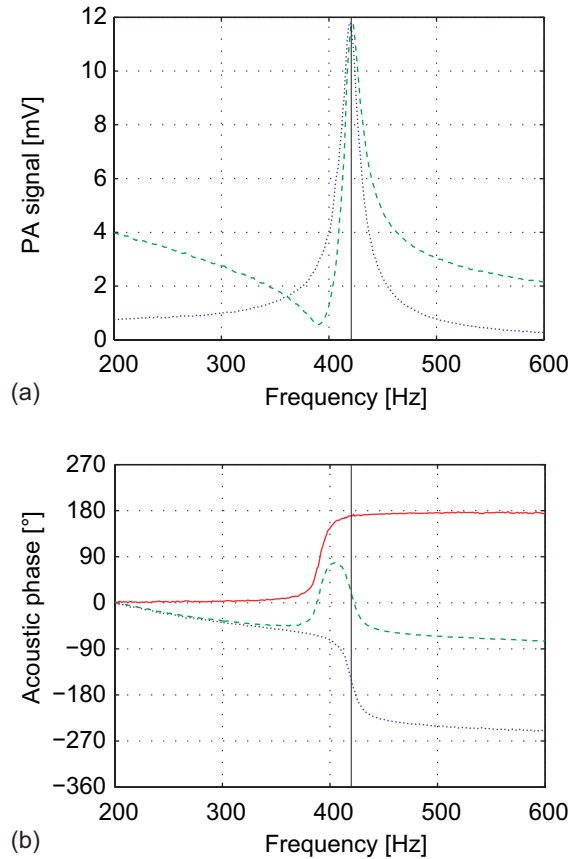


Figure 4.10: Measured frequency (a) and phase (b) behaviour of the differential cell with the tuned membrane in the case of a photoacoustic excitation. *Dashed curves* represent measurements for an excitation in the *same* volume as the detection, *dotted curves* measurements for an excitation in the *opposite* volume; resonant frequencies show a 3 Hz shift. *Solid line* in the phase graph illustrates the phase difference between the two volumes, which, at an average values between the two resonant frequencies (indicated by a *vertical line*) is equal to 169° .

Curves representing magnitudes are very similar to the ones obtained with a loudspeaker excitation, showing a small 3 Hz shift between resonant frequencies (422 and 419 Hz), and respective quality factors of 30.7 and 31.4 for an excitation in the same and in the opposite volume with respect to the microphone.

Results concerning the phase are better compared to the acoustic measurements, as a phase shift of 169° is obtained in the range between the two resonant frequencies.

Still, the non-achievement of a phase shift exactly equal to π will play a significant role when performing differential measurements, as it will be explained in detail in § 4.4.3.

4.3.4 Noise level

As already illustrated in the previous chapter, noise level is a parameter of the utmost importance when photoacoustic spectroscopy is considered, as it directly influences the detection limit of the sensor.

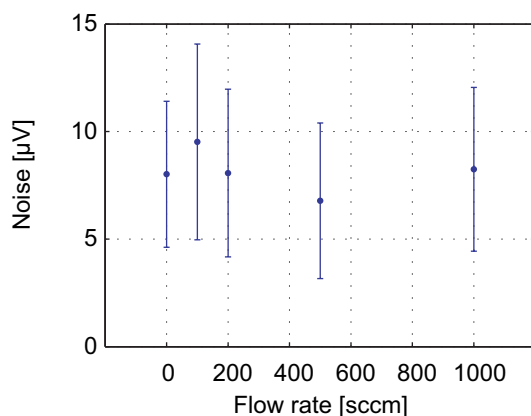


Figure 4.11: Acoustic noise as a function of flow rate. *Circles* represent the measured noise value averaged over 10 minutes with 10 s integration time, *errorbars* correspond to standard deviation of measured signal. Flow rates up to 1000 sccm have been tested without major effects on the overall noise.

Noise level has been measured as a function of the gas flow passing through the cell, and results are depicted in Fig. 4.11. Measurements have been performed at the resonant frequency, by placing the cell in the isolating wooden box described in § 3.3.2, and by recording the noise signals with an integration time of 10 s. Results illustrate a noise level between 7 and 9 μV with a standard deviation around 4 μV , whereas gas flow shows no influence on the observed values; these values, obtained with the same type of microphone and preamplifier as the first Helmholtz cell, are approximately 3 times higher for both average and standard deviation, which is explained by the much lower operating frequency of the differential cell.

4.4 Differential measurements

4.4.1 Characterisation of the laser sources

Two different laser sources have been utilised in conjunction with the differential cell. The first one is a 760 nm vertical-cavity surface-emitting laser (VCSEL), used to perform oxygen measurements; the second is a DFB laser emitting at 1650 nm, and has been implemented to detect methane.

4.4.1.1 VCSEL for oxygen detection

Oxygen sensing is extensively used in several biochemical and medical applications [8, 9], as well as in the industrial [10] and the environmental [11] fields.

Intensity of oxygen absorption lines is very low. In fact, as already introduced in § 2.2, O_2 is a homonuclear molecule, so that its vibrational and rotational transitions are forbidden. Hence, only electronic transitions are active, and give rise to a weak absorption band ($b^1\Sigma_g^+ \leftarrow X^3\Sigma_g^-$) located in the 760 - 770 nm region, whose corresponding absorption coefficients at ambient temperature and pressure are in the order of 10^{-3} cm^{-1} [12].

Nonetheless, despite the weak absorption lines, oxygen optical detection

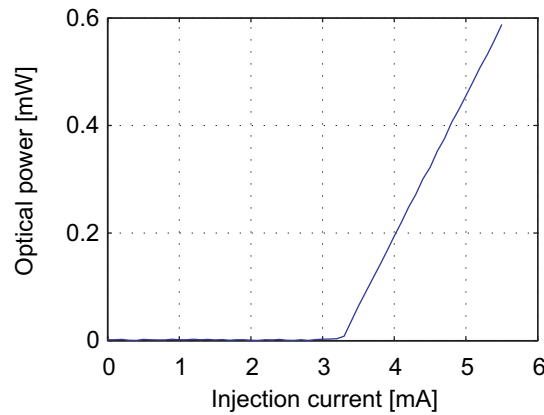


Figure 4.12: Output power of the VCSEL as a function of injection current for $T = 25^\circ\text{C}$. Threshold current is approximately 3.3 mA, whereas highest measured power is slightly less than 0.6 mW.

techniques have been investigated since the 80s [13], generally using DFB lasers [14, 15] or VCSELs [15, 16, 17, 18] though the use of other sources has also been reported [19, 20]. Photoacoustic spectroscopy of oxygen using both DFB and VCSEL sources has been demonstrated as well [21].

In this application, the selected source to perform oxygen sensing is a commercially available VCSEL emitting at 760 nm. Thanks to their simple manufacturing technology, VCSELs offer a very competitive cost with respect to other available sources emitting in the same spectral region, such as DFB and external-cavity diode lasers (ECDL), whose price is more than 10 times higher. On the other hand, they deliver an optical power in the order of 1 mW, which is considerably lower compared to the few tens (DFB) or even few hundreds (ECDL) of milliwatts supplied by other sources.

Fig. 4.12 illustrates the VCSEL output power observed for a laser temperature of 25°C ; optical power was measured using an optical powermeter mounted directly in front of the source; injection current values are much lower compared to standard DFB lasers, ranging from a threshold of 3.3 mA to a maximum allowed current of 5.5 mA, beyond which the laser is no longer guaranteed to provide a single-mode emission. The highest measured power is slightly below 0.6 mW.

Another significant difference with respect to DFB lasers is the relation between laser temperature and output power. In a DFB laser, power is inversely proportional to temperature in the whole operating range of the device. When VCSELs are considered, this rule is only valid down to a certain temperature value; for lower temperatures, output power begins to decrease, as shown in Fig. 4.13 for the selected VCSEL. This atypical behaviour is due to the fact that VCSELs present a very short optical cavity, resulting in a mismatch between gain curve and cavity mode when temperature variations are important.

Due to their low operating current, VCSELs are very low power-consuming devices; on the other hand, their wavelength is much more sensible to injection current than compared to standard DFB laser, so that few microamperes of current noise are sufficient to induce a significant wavelength instability. In this purpose, two laser drivers have been tested, showing respective current

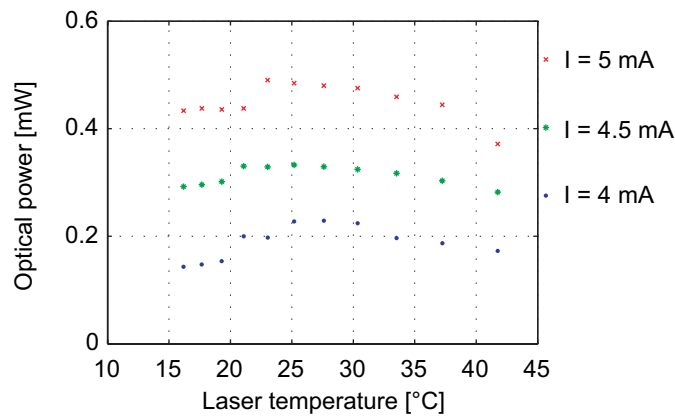


Figure 4.13: Dependence of the VCSEL power on the temperature. Output power increases till temperature goes down to a limit value, then decreases again.

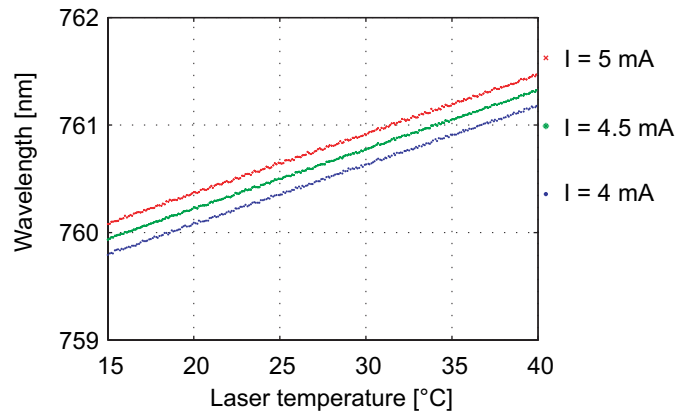


Figure 4.14: Wavelength tuneability of the VCSEL as a function of temperature, measured for injection currents between 4 and 5 mA with a 0.5 mA step.

noises of 5 and $1.5 \mu\text{A}$. Fig. 4.14 illustrates the wavelength tuneability of the VCSEL for injection currents between 4 and 5 mA, measured using the second driver; the current noise effect is clearly visible. A very good linearity is obtained both over temperature and over current, with respective tuning coefficients of 0.28 nm/mA (-148 GHz/mA) and $0.056 \text{ nm/}^\circ\text{C}$ ($-28.9 \text{ GHz/}^\circ\text{C}$), but the three observed curves are slightly noisy. In fact, due to the very high current tuning coefficient, the resulting uncertainty on the VCSEL wavelength is approximately 0.42 pm (220 MHz); when the first driver is used, this value reaches as much as 1.4 pm (740 MHz), thus becoming comparable to the typical HWHM linewidth of an absorption line ($\sim 1.5 \text{ GHz}$).

Fig. 4.15 depicts the spectrum of pure oxygen saturated with water vapour (2.3% at room temperature), obtained by scanning the laser temperature between 15°C and 40°C , and by intensity-modulating the injection current with a square signal of 3 mA around a 4 mA operating setpoint, compared with the spectrum calculated from the HITRAN database. There is a good agreement between experimental and theoretical values, but the observed photoacoustic signal is in the order of magnitude of only $100 \mu\text{V}$.

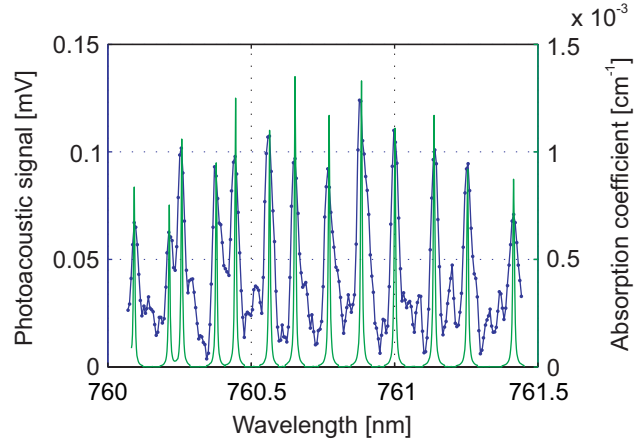


Figure 4.15: Oxygen spectrum measured with the selected VCSEL, using a square current modulation (4 ± 1.5 mA, *solid curve with dots*), for temperatures between 15°C and 40°C , along with calculated spectrum from HITRAN database (*solid curve*).

4.4.1.2 DFB laser for methane detection

An example of methane detection, along with a description of its spectroscopic properties, has already been discussed in the previous chapter (§ 3.3.3 and 3.4.3). In that case, the investigated lines were located within the $\tilde{\nu}_1 + \tilde{\nu}_4$ band, matching the $2.37\ \mu\text{m}$ emission of the antimonide laser diode.

In this application, the $2\tilde{\nu}_3$ band, located in the $1.65\ \mu\text{m}$ region, has been selected, taking benefit from a commercially available DFB laser emitting at this wavelength and supplied with a fibre-coupled output. A standard current and temperature driver, with respective resolutions of $0.01\ \text{mA}$ and 0.1°C has been used to control the laser parameters.

Fig. 4.16 illustrates the output power of the DFB laser, measured connecting the laser fibre output to an optical powermeter. As expected, after a threshold located between 10 and $20\ \text{mA}$, the optical power is linearly proportional to the injection current and inversely proportional to the temperature, with a maximum measured power of approximately $20\ \text{mW}$ (@ $T = 10^\circ\text{C}$ and $I = 140\ \text{mA}$).

Wavelength and tuneability of the laser are depicted in Fig. 4.17. A nice continuous tuneability over more than $3\ \text{nm}$ is observed when injection current and temperature are modified. Corresponding tuning coefficients are $-0.81\ \text{GHz/mA}$ ($0.0073\ \text{nm/mA}$) and $-12.6\ \text{GHz}/^\circ\text{C}$ ($0.11\ \text{nm}/^\circ\text{C}$).

The probed methane absorption line is illustrated in Fig. 4.18; the cell is filled with $5000\ \text{ppm}$ of CH_4 , the laser temperature is scanned between 15°C and 30°C , and the injection current is intensity-modulated with a square signal of $140\ \text{mA}$ around a $70\ \text{mA}$ operating setpoint; the measured line is in good agreement with the theoretical calculations from HITRAN.

Main characteristics of both sources are summarised in Table 4.2. It is interesting to notice the opposite behaviour of the lasers when temperature- and current-tuning are considered. Dependence of the VCSEL wavelength on injection current is 5 times stronger with respect to the temperature, whereas the temperature-tuning coefficient of the DFB laser is more than 10 times

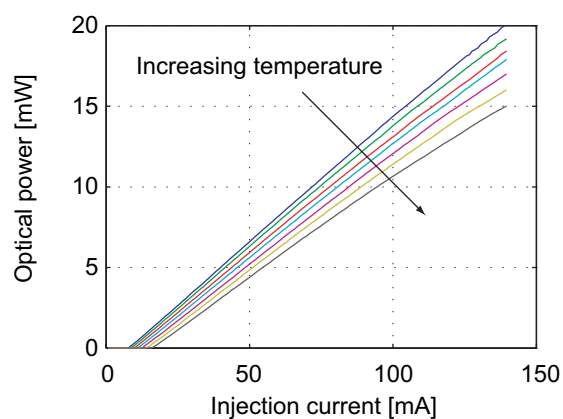


Figure 4.16: Output power of the DFB laser as a function of injection current, measured at temperatures between 10°C and 40°C with a 5°C step.

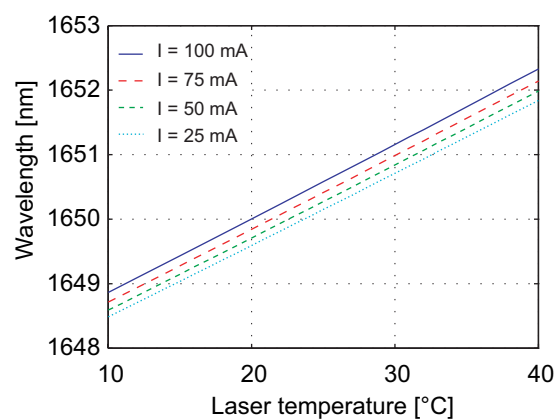


Figure 4.17: Wavelength tuneability of the DFB laser as a function of temperature, measured for injection currents between 25 and 100 mA with a 25 mA step.

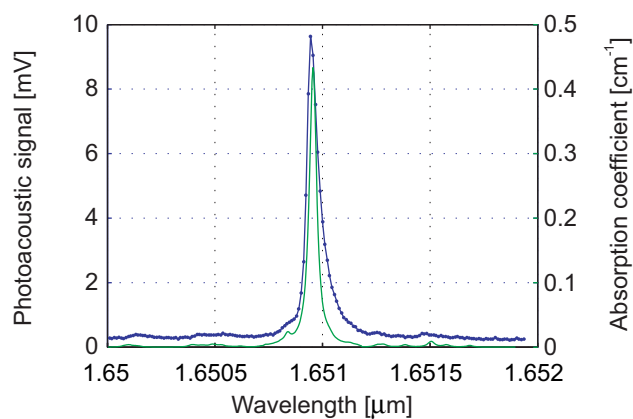


Figure 4.18: Methane absorption line measured with the selected DFB laser, using a square current modulation (70 ± 70 mA, *solid curve with dots*), for temperatures between 15 °C and 35 °C, along with calculated spectrum from HITRAN database (*solid curve*).

Gas	O ₂	CH ₄
Source	VCSEL	DFB
Operating wavelength [nm]	760.9	1651.0
Spectral range [nm]	759.8 - 761.5	1648.5 - 1652.2
Temp. tuning [nm/°C]	0.056	0.11
Current tuning [nm/mA]	0.28	0.0073
T _{set} [°C]	22.9	26.1
I _{set} [mA]	4.0	130.3
Average power [mW]	0.2	15

Table 4.2: Main characteristics of the VCSEL and of the DFB laser used with the differential cell. T_{set} and I_{set} are the temperature and current operating point of the corresponding laser, respectively. The average power is obtained for the operating conditions at T_{set} and I_{set}.

larger than the current-tuning.

4.4.2 Description of the experimental setup

The setup used to perform differential measurements is similar to the one described in the case of the first cell, in § 3.4.2, with the exception of some bulk optics elements needed to collimate and align the laser beam.

When performing methane measurements, the DFB laser diode is connected to an optical collimator, which provides the desired parallel beam. In the case of oxygen detection, an 8 mm focal lens is mounted on a 3-axes micro-displacement stage and positioned in front of the VCSEL, so that the beam is efficiently collimated.

The laser beam is aligned perpendicularly with respect to the cell volumes; a beam splitter cube deviates part of the light into the first volume, whereas the remaining light is reflected by a suitable mirror and fed into the second volume. Intensities of transmitted and reflected light are approximately the same in the case of the VCSEL, whereas intensity of the reflected light is sensibly higher with respect to the transmitted light when the DFB laser is considered, due to the uneven behaviour of the beam splitter at the DFB wavelength. The resulting unbalanced power distribution has to be compensated by a suitable alignment of the bulk optics element. This alignment proves to be very critical, and micro-adjustment systems have to be used on both steering elements in order to optimise and balance the photoacoustic signals generated inside the cell volumes.

Fig. 4.19 shows a picture of the sensor. The setup is completed with a laser driver, a lock-in amplifier to detect the microphone signal, and a system of mass-flow controllers and certified gas cylinders to provide the desired gas concentrations. An H₂O saturator is implemented between the O₂ cylinder and the sensor, in order to add to the gas compound a certain percentage of water vapour, playing the role of enhancing deactivation of oxygen molecules to catalyse the relaxation process (see Fig. 4.20).

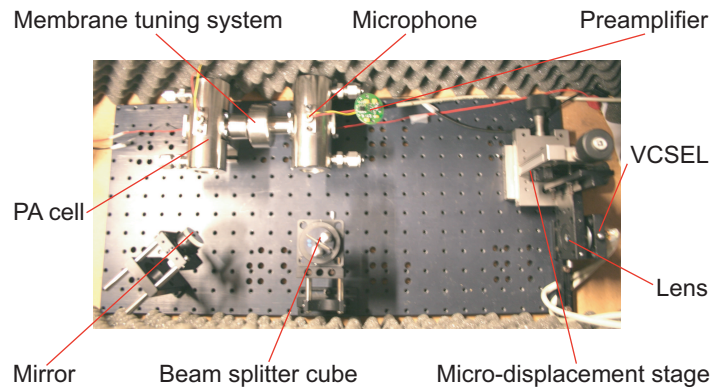


Figure 4.19: Picture of the experimental setup with the VCSEL. Bulk optics elements are visible at the bottom of the picture, whereas the photoacoustic cell is in the upper part.

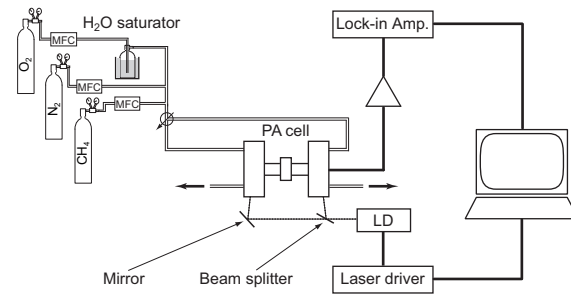


Figure 4.20: Scheme of the experimental setup. Oxygen concentration is determined by certified gas cylinders connected to mass-flow controllers (MFC). An H_2O saturator adds a certain percentage of water vapour to the gas compound. Laser diode (LD) is temperature- and current-controlled through a laser driver. Beam splitter and mirror direct the light beams into the cell volumes with an optimised incidence angle. Microphone signal is preamplified and detected with a lock-in amplifier.

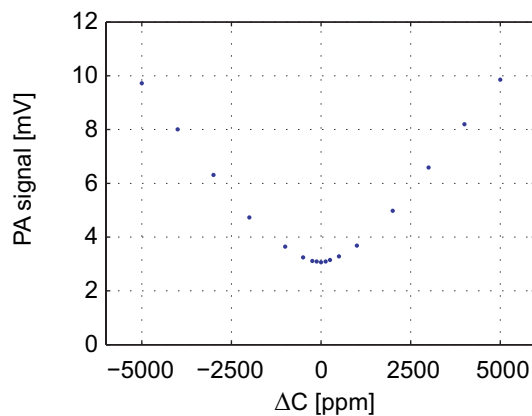


Figure 4.21: Photoacoustic signal as a function of the difference between CH_4 concentrations in the volumes. When the concentrations values are closer, the signal is no longer linear with respect to ΔC , resulting in a non-zero value when concentrations are identical.

4.4.3 $R - \theta$ and $x - y$ detection schemes

Fig. 4.21 reports the observed microphone signal as a function of the difference ΔC between methane concentrations in the two volumes of the cell. One volume is filled with a fixed concentration of 5000 ppm, whereas the concentration in the other volume is gradually increased from 0 to 5000 ppm. The procedure is then repeated by inverting the concentrations in the volumes. The DFB laser is wavelength-modulated with an optimised modulation depth of ± 6.3 mA, while the operating point is set by an injection current of 130.3 mA and a temperature of 26.1°C.

As long as the concentration difference is higher than 1000 ppm, the corresponding PA signal follows an expected linear trend proportional to ΔC . Nevertheless, when the concentration values become comparable and their difference gets closer to zero, the PA signal is no longer linear with respect to ΔC , eventually resulting in a residual non-zero signal when the concentrations inside the volumes are identical.

Both the non linearity and the presence of a residual signal are a direct consequence of the non achievement of the desired π phase shift between the volumes, as it will be demonstrated in the appendix A.1.

The described effects are more important when the difference between concentrations is small, which is definitely the most interesting range when performing differential measurements; hence, measuring only the magnitude of the obtained differential photoacoustic signal is not an efficient way to determine the sought concentration difference.

A sensitive improvement is obtained when exploiting a different detection scheme provided by the lock-in amplifier, which allows to measure separately the in-phase (x) and the quadrature (y) components of a signal, differently from the standard detection scheme supplying magnitude (R) and phase (θ). The proposed solution consists in reducing to zero the x component of the residual PA signal observed when gas concentrations are identical, which can be achieved by setting the lock-in internal phase to a proper value. Theoretical calculations, detailed in the appendix A.2, show that in this way the x component of the PA signal becomes linear with respect to ΔC .

Fig. 4.22 shows the observed x component of the PA signal as a function of the difference between CH_4 concentrations in the volumes. In the whole concentration difference range of ± 500 ppm, the in-phase component shows a very good linearity (correlation factor $R^2 = 0.997$) with respect to the concentration difference ΔC , thus providing a more accurate and efficient way to determine it.

When trying to apply the same detection scheme to perform oxygen detection, several problems are experienced. As shown by the measured O_2 spectrum (Fig. 4.15), the observed photoacoustic signal for an oxygen concentration of 100% is approximately 100 μV ; when comparing this value to the noise level, evaluated at few microvolts, the resulting SNR is very poor. Origin of these extremely low values is multiple: first of all the probed absorption lines, resulting from electronic transitions, show a very small intensity, so that corresponding absorption coefficients at ambient pressure and temperature are in the 10^{-3} cm^{-1} range; the available VCSEL power is very low as well, providing an average value of only 0.2 mW; moreover, the very low SNR does not concretely allow a fine alignment of the two arms of the laser beam,

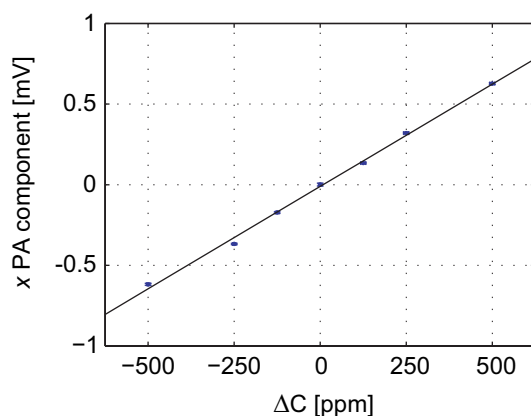


Figure 4.22: x component of the photoacoustic signal as a function of the difference between CH_4 concentrations in the volumes. *Dots* are measured values, *errorbars* correspond to uncertainties on the signal (*vertical axis*) and on the concentration difference (*horizontal axis*), *solid line* is a linear fit. A good linearity is observed between measured signal and concentration difference.

so that the PA signal cannot be properly optimised.

The resulting situation makes oxygen detection very difficult. An example is illustrated in Fig. 4.23; both volumes are filled with pure oxygen saturated with 1.15% of water vapour, and the reported signal is obtained by letting both arms of the split beam enter the cell (from 0 to ~ 10 minutes) or by alternatively blocking one of the arms (respectively from ~ 10 to ~ 25 minutes and from ~ 25 minutes to the end). Intensities of the resulting average signals are lower than $50 \mu\text{V}$, which makes any kind of measurement concretely impossible.

4.4.4 Performances of the sensor

The achieved results, illustrated in the previous section, demonstrate the possibility to successfully perform differential photoacoustic spectroscopy using the developed sensor.

The smallest detectable methane concentration difference, corresponding to three times the standard variation of the noise signal σ_N , is approximately 20 ppm (corresponding to 0.4% of the absolute concentrations), which, as summarised in Table 4.3, leads to an ultimate detection sensitivity of $8.54 \cdot 10^{-7} \text{ W} \cdot \text{cm}^{-1} \text{ Hz}^{-1/2}$.

This value is more than 2 orders of magnitude higher when compared to the sensor described in the previous chapter, which is due to several factors. First of all, the implementation of a rubber membrane, though thinner than 1 mm, induces a severe loss on acoustic signals, as already shown in § 4.3.2. Furthermore, the utilised beam splitter shows a strongly asymmetrical behaviour at the operating wavelength, resulting in a disproportioned distribution of the transmitted (approximately 10%) and the reflected (the remaining 90%) optical powers. As a consequence, the reflected beam has to be misaligned with respect to its optimum incidence angle and position, in order to balance the photoacoustic signals separately generated in the volumes for the same methane concentration, and this reduces the available signals. Finally, due to

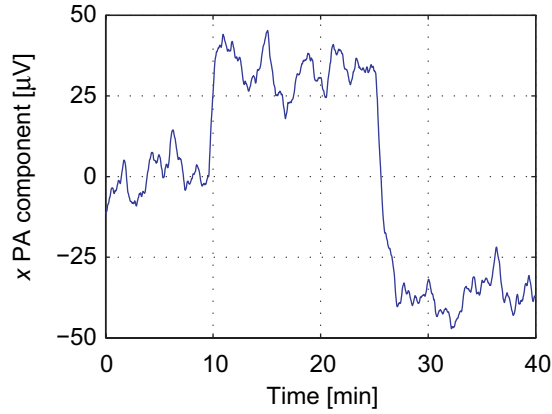


Figure 4.23: Evolution of the x component of the oxygen photoacoustic signal as a function of time. Both volumes are filled with pure oxygen saturated with water vapour. From 0 to ~ 10 minutes both volumes are illuminated, from ~ 10 to ~ 25 minutes only one volume is illuminated, while from ~ 25 minutes on, only the opposite volume is illuminated.

Photoacoustic sensor performances	
α_0 [cm^{-1}]	0.45
P_0 [W]	$15 \cdot 10^{-3}$
τ_{int} [s]	10
$3\sigma_N$ [μV]	16.5
ΔC_{lim} [ppm]	20
D [$\text{W} \cdot \text{cm}^{-1} \text{Hz}^{-1/2}$]	$8.54 \cdot 10^{-7}$

Table 4.3: Summary of the differential photoacoustic sensor performances.

the low selected resonant frequency, the observed noise level is higher, leading to a further decrease of the signal-to-noise ratio.

As far as oxygen detection is concerned, the selected VCSEL does not supply a sufficiently high optical power to perform efficient measurements. Taking into account the calculated sensitivity, to achieve a typical detection limit of 1% using this sensor, an optical power of 10 mW is required.

Bibliography

- [1] J. Uotila, V. Koskinen, and J. Kauppinen, “Selective differential photoacoustic method for trace gas analysis,” *Vib. Spectrosc.* **38**(1-2), 3–9 (2005).
- [2] J. M. Rey and M. W. Sigrist, “Differential mode excitation photoacoustic spectroscopy: a new photoacoustic detection scheme,” *Rev. Sci. Instrum.* **78**(6), 5 (2007).
- [3] G. Busse and D. Herboeck, “Differential Helmholtz resonator as an optoacoustic detector,” *Appl. Opt.* **18**(23), 3959–3961 (1979).
- [4] M. G. Da Silva, H. Vargas, A. Miklós, and P. Hess, “Photoacoustic detection of ozone using a quantum cascade laser,” *Appl. Phys. B* **78**(6), 677–680 (2004).
- [5] V. Zéninari, V. A. Kapitanov, D. Courtois, and Y. N. Ponomarev, “Design and characteristics of a differential Helmholtz resonant photoacoustic cell for infrared gas detection,” *Infrared Phys. Technol.* **40**(1), 1–23 (1999).
- [6] H. E. Bass and H. J. Bauer, “Kinetic model for thermal blooming in atmosphere,” *Appl. Opt.* **12**(7), 1506–1510 (1973).
- [7] M. Rossi, *Electroacoustique*, Traité d’électricité (Presses polytechniques romandes, Lausanne, 1986).
- [8] P. Poulet, D. Cahen, and S. Malkin, “Photoacoustic detection of photosynthetic oxygen evolution from leaves. Quantitative analysis by phase and amplitude measurements,” *Biochim. Biophys. Acta* **724**(3), 433–446 (1983).
- [9] J. I. Peterson, R. V. Fitzgerald, and D. K. Buckhold, “Fiber-optic probe for in vivo measurement of oxygen partial pressure,” *Anal. Chem.* **56**(1), 62–67 (1984).
- [10] I. Linnerud, P. Kaspersen, and T. Jaeger, “Gas monitoring in the process industry using diode laser spectroscopy,” *Appl. Phys. B* **67**(3), 297–305 (1998).
- [11] R. M. A. Kocache, J. Swan, and D. F. Holman, “A miniature rugged and accurate solid electrolyte oxygen sensor,” *J. Phys. E: Sci. Instrum.* **17**(6), 477–482 (1984).
- [12] L. S. Rothman, D. Jacquemart, A. Barbe, D. C. Benner, M. Birk, L. R. Brown, M. R. Carleer, C. Chackerian, K. Chance, L. H. Coudert, V. Dana, V. M. Devi, J. M. Flaud, R. R. Gamache, A. Goldman, J. M. Hartmann, K. W. Jucks, A. G. Maki, J. Y. Mandin, S. T. Massie, J. Orphal, A. Perrin, C. P. Rinsland, M. A. H. Smith, J. Tennyson, R. N. Tolchenov, R. A. Toth, J. Vander Auwera, P. Varanasi, and G. Wagner, “The HITRAN 2004 molecular spectroscopic database,” *J. Quant. Spectrosc. Radiat. Transf.* **96**(2), 139–204 (2005).

-
- [13] M. Kroll, J. A. McClintock, and O. Ollinger, "Measurement of gaseous oxygen using diode laser spectroscopy," *Appl. Phys. Lett.* **51**(18), 1465–1467 (1987).
- [14] C. Corsi, M. Gabrysch, and M. Inguscio, "Detection of molecular oxygen at high temperature using a DFB-diode-laser at 761 nm," *Optics Communications* **128**(1-3), 35–40 (1996).
- [15] V. Weldon, J. Ogorman, J. J. Pérez-Camacho, D. McDonald, J. Hegarty, J. C. Connolly, N. A. Morris, R. U. Martinelli, and J. H. Abeles, "Laser diode based oxygen sensing: A comparison of VCSEL and DFB laser diodes emitting in the 762 nm region," *Infrared Phys. Technol.* **38**(6), 325–329 (1997).
- [16] H. P. Zappe, M. Hess, M. Moser, R. Hövel, K. Gulden, H. P. Gauggel, and F. M. di Sopra, "Narrow-linewidth vertical-cavity surface-emitting lasers for oxygen detection," *Applied Optics* **39**(15), 2475–2479 (2000).
- [17] P. Vogel and V. Ebert, "Near shot noise detection of oxygen in the A-band with vertical-cavity surface-emitting lasers," *Appl. Phys. B* **72**(1), 127–135 (2001).
- [18] J. Wang, S. T. Sanders, J. B. Jeffries, and R. K. Hanson, "Oxygen measurements at high pressures with vertical cavity surface-emitting lasers," *Appl. Phys. B* **72**(7), 865–872 (2001).
- [19] D. M. Bruce and D. T. Cassidy, "Detection of oxygen using short external cavity GaAs semiconductor diode lasers," *Appl. Opt.* **29**(9), 1327–1332 (1990).
- [20] Q. V. Nguyen, R. W. Dibble, and T. Day, "High-resolution oxygen absorption spectrum obtained with an external-cavity continuously tunable diode laser," *Opt. Lett.* **19**(24), 2134–2136 (1994).
- [21] H. Cattaneo, T. Laurila, and R. Hernberg, "Photoacoustic detection of oxygen using cantilever enhanced technique," *Appl. Phys. B* **85**(2-3), 337–341 (2006).

Chapter 5

Conclusion

The purpose of the present thesis has been to demonstrate the good performances of Helmholtz acoustic resonators applied to photoacoustic spectroscopy. Two fully novel different Helmholtz-based photoacoustic cells have been developed, and their design, characterisation and spectroscopic performances have been described into details in separate chapters.

The development of the two cells has been carried out with the support of several mathematical simulations, taking benefit from the theory of acoustic resonators, as much as from some models based on well-established analogies between acoustic and electrical domains. The different technical constraints, imposed by the characteristic properties of the selected laser sources, or by the required external elements to perform the measurements, have also played a fundamental role within the final design of the cells.

The first sensor has been designed to suit the peculiar properties of some recently developed antimonide-based DFB lasers emitting in the region between 2 and 2.7 μm . The supplied highly divergent emission has been injected into the cell without any collecting optics, and the multiple reflections of the laser beam inside the excitation volume have been positively exploited to increase the interaction path between light and gas. A meticulous optimisation effort to enhance the photoacoustic signal, through a suitable gold coating on the internal cell walls, a fine adjustment of the cell dimensions and an accurate choice of the modulation scheme, as well as the reduction of external noise thanks to the use of silencers and of an isolating chamber, has led to the achievement of a sub-ppm detection limit for ammonia sensing, performed with a laser emitting few milliwatts of optical power. The described sensor proves to be compact and easy of use, as the overall dimensions of the cell are smaller than 10 cm and no precise alignment of the laser source is needed.

The second sensor has been developed for a particular application, which consists in delivering a measurement of the difference between two concentrations of the same gas. The theoretical π phase shift existing between the two volumes of a Helmholtz resonator has been exploited to obtain a photoacoustic signal proportional to the sought concentration difference, each volume being illuminated by a fraction of the same laser beam. The actual phase shift being slightly lower than π , an $x - y$ detection scheme has been implemented instead of the common $R - \theta$ scheme, in order to obtain a linear and zero-background relation between the photoacoustic signal and the gas concentrations difference. The requirement for a collimated laser beam and for a balanced optical power distribution between the two cell volumes has led to the utilisation

of some external bulk optics elements. Though more complex and less performing with respect to the first sensor, this intrinsically differential sensor offers the concrete possibility to perform, with a single instrument, a type of measurement which would normally require two separate sensing devices.

Perspectives

To conclude this thesis, some interesting applications or future developments of the described sensors are given.

The experimental results illustrated within this work have been obtained in laboratory facilities. An implementation of the developed sensors for *in situ* measurements, not yet performed, would provide a more complete analysis of their performances and of their concrete possibility of application in any measurement field.

The first sensor, which offers the possibility to positively exploit the divergence of a laser beam and makes no use of any bulk optics, can find very favourable applications in conjunction with the newly developed quantum cascade lasers, which are step-by-step taking over the role of reference source for spectroscopy when mid infrared range is considered. The availability of high optical powers and of stronger absorption lines than in the telecoms range may sensibly improve the detection limit achieved within this work. In the purpose to perform *in situ* measurements, the integration of a reference cell to stabilise the laser wavelength, as well as the implementation of a technique to normalise the PA signal by the optical power (for instance, using both $1f$ and $2f$ detections and monitoring the wall noise, directly proportional to the power) should be considered as well.

Concerning the second sensor, beside the implementation of a more powerful source in order to efficiently perform oxygen detection, the availability of two separate volumes may prove very helpful in isotope monitoring applications; in this case, one volume would be filled with a reference substance whose isotopic ratio is known, while the other would contain the same substance, but showing a different isotopic ratio, the resulting signal being proportional to the difference of the two.

Appendix A

Differential photoacoustic signal

This appendix is meant to illustrate some theoretical calculations concerning the photoacoustic signal generated in the differential sensor described in chapter 4.

Two sections will be included; the first one will concern the quantitative influence of the phase shift between the volumes on the differential signal; the second section will be dedicated to demonstrate the linearity of the x component of the signal with respect to the concentration difference ΔC when the internal phase of the lock-in amplifier used to perform the detection is set to a proper value.

A.1 Influence of the phase shift

The photoacoustic signal detected by the microphone in the differential photoacoustic cell can be expressed as the sum of the contributions p_1 and p_2 generated in the two volumes:

$$p_{diff} = p_1 e^{j\varphi_1} + p_2 e^{j(\varphi_1 + \Delta\varphi)} \quad [\text{Pa}] \quad (\text{A.1})$$

where φ_1 is the phase of the signal generated in the first volume and $\Delta\varphi$ the phase shift between the volumes. When assuming that the gas concentrations and the optical power in the volumes, and therefore the respective photoacoustic signals, are identical, eq. (A.1) becomes:

$$p_{diff} = p_1 e^{j\varphi_1} (1 + e^{j\Delta\varphi}) \quad [\text{Pa}] \quad (\text{A.2})$$

If $\Delta\varphi$ is equal to π , the two terms within brackets compensate reciprocally and the resulting signal is null, which corresponds to the ideal case.

On the contrary, if $\Delta\varphi$ is even slightly different from π , magnitude of p_{diff} increases rapidly, as reported in Fig. A.1; as an example, when the phase shift is 174° , hardly 6° lower than π , the resulting photoacoustic signal reaches a value as high as 10% of p_1 .

A second direct consequence of the non-achievement of a π phase shift is the no longer linear dependence of the differential photoacoustic signal p_{diff} on the difference between the magnitudes of the two volumes contributions $\Delta p = p_1 - p_2$. Fig. A.2 illustrates the theoretical evolution of this relation for

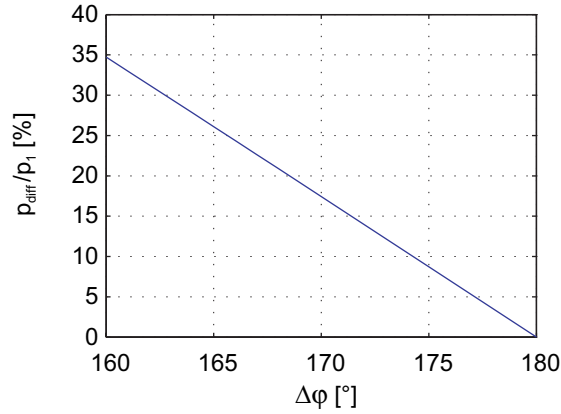


Figure A.1: Theoretical dependence of the differential photoacoustic signal resulting from two identical gas concentrations as a function of the phase shift. Magnitude of the differential signal reaches 10% of a single volume signal for a 174° phase shift.

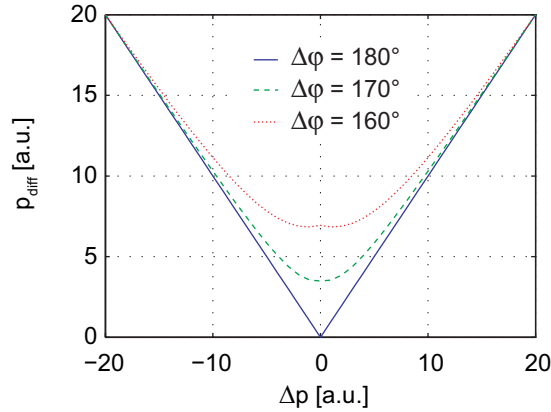


Figure A.2: Theoretical dependence of the differential photoacoustic signal as a function of the two volumes contributions, calculated for phase shifts of 180° (*solid line*), 170° (*dashed line*) and 160° (*dotted line*).

three different phase shift values: 180°, 170° and 160°. As long as the phase shift decreases, the linearity is respected only for large signal differences.

The observed PA signal as a function of methane concentration, reported in Fig. 4.21, follows a very similar trend to the dashed curve, calculated for a phase shift of 170°, which is the actual value of the observed phase shift between the volumes (see § 4.3.3).

A.2 In-phase and quadrature components

An efficient method to obtain a linear measurement with respect to the difference between the two volumes contributions, and therefore between the gas concentrations, is proposed in § 4.4.3, and takes benefit from the x - y detection scheme provided by the lock-in amplifier. This method concretely consists in setting the internal phase of the lock-in amplifier to a suitable value, so that the resulting in-phase component x_{diff} of the PA signal corresponding to a zero concentration difference is null. A theoretical demonstration of the

linearity of this method is presented hereafter.

The in-phase component of the PA signal can be written by taking the real part of eq. (A.1):

$$x_{diff} = \text{Re}[p_{diff}] = p_1 \cos(\varphi_1) + p_2 \cos(\varphi_1 + \Delta\varphi) \quad [\text{Pa}] \quad (\text{A.3})$$

Assuming that magnitudes of the two contributions are identical, this equation becomes:

$$x_{diff} = p_1 [\cos(\varphi_1) + \cos(\varphi_1 + \Delta\varphi)] \quad [\text{Pa}] \quad (\text{A.4})$$

When the internal phase of the lock-in amplifier is set to have x_{diff} equal to zero, the term within brackets fulfills the following condition:

$$\cos(\varphi_1) = -\cos(\varphi_1 + \Delta\varphi) \quad [-] \quad (\text{A.5})$$

which is obtained when:

$$\varphi_1 + \Delta\varphi = \pi - \varphi_1 \quad \Rightarrow \quad \varphi_1 = \frac{\pi - \Delta\varphi}{2} \quad [\text{rad}] \quad (\text{A.6})$$

Merging eq. (A.6) into eq. (A.3) the dependence of x_{diff} on the two contributions can be expressed as:

$$x_{diff} = p_1 \cos\left(\frac{\pi - \Delta\varphi}{2}\right) + p_2 \cos\left(\frac{\pi + \Delta\varphi}{2}\right) \quad [\text{Pa}] \quad (\text{A.7})$$

Finally, taking advantage of some well known trigonometric relations, the following expression is obtained:

$$\begin{aligned} x_{diff} &= p_1 \sin\left(\frac{\Delta\varphi}{2}\right) - p_2 \sin\left(\frac{\Delta\varphi}{2}\right) = \\ &= \sin\left(\frac{\Delta\varphi}{2}\right) (p_1 - p_2) \quad [\text{Pa}] \quad (\text{A.8}) \end{aligned}$$

which demonstrates the linear dependence of the in-phase component of the photoacoustic signal on the difference between the two contributions p_1 and p_2 , and hence on the concentration difference ΔC , as illustrated experimentally in chapter 4 in the case of methane measurements (Fig. 4.22).

Furthermore, as long as the phase shift higher than 160° , the term $\sin\left(\frac{\Delta\varphi}{2}\right)$ is very close to 1, so that the resulting signal loss is lower than 2%.

Publications

- [1] S. Schilt, A. Vicet, R. Werner, M. Mattiello, L. Thévenaz, A. Salhi, Y. Rouillard, and J. Koeth, “Application of antimonide diode lasers in photoacoustic spectroscopy,” *Spectrochim. Acta A* **60**(14), 3431–3436 (2004).
- [2] M. Mattiello, M. Niklès, S. Schilt, L. Thévenaz, D. Barat, A. Salhi, A. Vicet, R. Werner, and J. Koeth, “Novel Helmholtz-based photoacoustic sensor for trace gas detection at ppm level using GaInAsSb/GaAlAsSb DFB lasers,” in *5th International Conference on Tunable Diode Laser Spectroscopy* (Florence, 2005).
- [3] M. Mattiello, M. Niklès, S. Schilt, L. Thévenaz, A. Salhi, D. Barat, A. Vicet, Y. Rouillard, R. Werner, and J. Koeth, “Novel Helmholtz-based photoacoustic sensor for trace gas detection at ppm level using GaInAsSb/GaAlAsSb DFB lasers,” *Spectrochim. Acta A* **63**(5), 952–958 (2006). Sp. Iss. SI.
- [4] M. Mattiello, L. Thévenaz, and M. Gyger, “Differential Helmholtz-based photoacoustic sensor operating in the 760 nm range for oxygen detection,” in *6th International Conference on Tunable Diode Laser Spectroscopy* (Reims, 2007).
- [5] M. Gyger, M. Mattiello, J. P. Besson, and L. Thévenaz, “The use of laser photoacoustic spectroscopy for tracer gas analyses of individually ventilated cage system,” *Submitted for publication to Laboratory Animals* (2007).

Nomenclature

List of symbols

$\alpha(\tilde{\nu})$	Absorption coefficient of a molecule
α_0	Normalized absorption coefficient of a molecule
β_T	Coefficient of thermal expansion
$\Delta\omega_n$	Broadening of the n^{th} acoustic mode
$\Delta\varphi$	Phase shift between the volumes of a Helmholtz resonator
ΔC	Difference between gas concentrations
ΔC_{lim}	Lowest detectable difference between gas concentrations
ΔE	Broadening of an energy level
Δf	Equivalent noise bandwidth
Δp	Difference between the magnitudes of the two volumes contributions to the differential photoacoustic signal
$\Delta\tilde{\nu}$	Broadening of an absorption line
$\Delta\tilde{\nu}_D$	Doppler broadening of an absorption line
$\Delta\tilde{\nu}_L$	Characteristic width of a lorentzian profile
$\Delta\tilde{\nu}_V$	Characteristic width of a Voigt profile
$\Delta\tilde{\nu}_{coll}$	Collisional broadening of an absorption line
$\Delta\tilde{\nu}_{nat}$	Natural broadening of an absorption line
ϵ	Thickness of a membrane
η	Coefficient of sheer viscosity
η_b	Coefficient of bulk viscosity
γ	Ratio of specific heats at constant pressure and volume
γ_{mn}	n^{th} extremum of first order Bessel function J_m
κ_T	Isothermal compressibility
Λ	Acoustic wavelength

λ	Optical wavelength
μ	Poisson's ratio of a material
ν	Frequency of the lightwave (in Hertz)
ω	Angular frequency
ω_0	Resonant angular frequency of an ideal lossless resonator
ω_n	Resonant angular frequency of the n^{th} acoustic mode
ω_{res}	Resonant angular frequency
ϕ	Incident photon flux
ϕ_0	Average incident photon flux
ρ	Density
ρ_0	Steady state density
ρ_a	Density variation
$\sigma(\tilde{\nu})$	Absorption cross section of a molecule
σ_N	Noise standard deviation
σ_{peak}	Cross section peak value
τ_{int}	Integration time
$\tau_{M_j-M_k}^{-1}$	Relaxation rate of molecule M_j through collisions with molecule M_k
τ_{oth}^{-1}	Relaxation rate of molecule M_j through collisions with all other molecules
τ_m	Global lifetime of an excited level
τ_{coll}	Mean time between collisions of a molecule
τ_{mnr}	Non-radiative lifetime of an excited level
τ_{mr}	Radiative lifetime of an excited level
τ_{sp}	Characteristic lifetime of an energy level
$\tilde{\nu}$	Frequency of the lightwave (in cm^{-1})
$\tilde{\nu}_0$	Transition frequency in a stationary molecule
$\tilde{\nu}_{las}$	Laser frequency
φ	Arbitrary phase value
φ_1	Phase of the first volume contribution to the differential photoacoustic signal
D	Electrical dipolar momentum of a molecule

D_e	Electronic contribution to the electrical dipolar momentum
D_N	Nuclear contribution to the electrical dipolar momentum
R_{nm}	Matrix element of the electrical dipolar momentum
r	Spatial propagation vector
v_l	Longitudinal fluid velocity
v	Fluid velocity
\hbar	Reduced Planck constant
a	Radius of a duct or of a resonator
A_n	Amplitude of the n^{th} acoustic mode
A_{nm}	Einstein coefficient for spontaneous emission
B_{nm}	Einstein coefficient for absorption
c	Light velocity in vacuum
C_i	Acoustic compliance
C_j	Concentration of measured molecule M_j
C_k	Concentration of buffer gas molecules M_k
C_p	Specific heat at constant pressure
c_s	Sound velocity
C_v	Specific heat at constant volume
C_{cell}	Cell constant
C_{gas}	Gas concentration
C_{lim}	Lowest detectable concentration
C_{mic}	Cell constant including microphone characteristics
D	Detection sensitivity
d	Diameter of a membrane
D_v	Coefficient of viscosity
E	Energy of a molecule
E_e	Electronic energy of a molecule
E_m	Upper energy state of a molecule
E_N	Nuclear energy of a molecule
E_n	Lower energy state of a molecule
E_r	Rotational energy of a molecule

E_v	Vibrational energy of a molecule
E_Y	Young's modulus of a material
f	Frequency
f_0	Resonant frequency
F_n	Normalised overlap integral
f_{kmn}	Resonant frequencies of a cylindrical resonator
f_{m0}	Fundamental resonant frequency of a membrane
g	Broadening coefficient
$g(\mathbf{r})$	Normalised spatial distribution of the laser beam
$g(\tilde{\nu})$	Normalized shape of an absorption line
$g_D(\tilde{\nu})$	Normalized gaussian profile
$g_L(\tilde{\nu})$	Normalized lorentzian profile
G_m	Gain of the microphone preamplifier
g_n	Degeneracy of an energy state
$g_V(\tilde{\nu})$	Normalized Voigt profile
g_{air}	Air-broadening coefficient
g_{self}	Self-broadening coefficient
H	Heat production rate
h	Planck constant
H_0	Average heat production rate
h_1, h_2	Heights of the volumes of a Helmholtz resonator
I	Current (acoustic-electrical analogy)
$I_0(\tilde{\nu})$	Intensity of the incident light
$I_a(\tilde{\nu})$	Intensity of the absorbed light
I_{set}	Operating laser injection current
J_m	First order Bessel function
K	Acoustic wavenumber
k	Boltzmann constant
K_T	Thermal conductivity
L	Acoustic mass
l	Length of a duct or of a resonator

l'	Open-end corrected duct length of a Helmholtz resonator
L_C	Supplementary acoustic mass
l_{path}	Length of the interaction path between light and gas
l_{sil}	Length of the pipe and of the volume of a silencer
M	Molar mass of a gas
M_j	Measured molecule
M_k	Buffer gas molecules
M_m	Sensitivity of the microphone
N	Density of a gas
N_m	Population of the upper level of a molecule
N_n	Population of the lower level of a molecule
n_T	Temperature coefficient for collisional broadening
p	Pressure
P_0	Incident optical power
p_0	Steady state pressure
p_1, p_2	Volumes contributions to the differential photoacoustic signal
p_a	Pressure variation
p_n	Spatial distribution of the n^{th} acoustic mode
p_{diff}	Differential photoacoustic signal
p_{self}	Partial pressure of the excited molecule
Q	Quality factor
Q_n	Quality factor of the n^{th} acoustic mode
Q_{int}	Total internal partition function
R	Perfect gas constant
$R - \theta$	Magnitude and phase detection scheme
r_1, r_2	Radii of the volumes of a Helmholtz resonator
R_{ac}	Acoustic resistance
S	Intensity of an absorption line
T	Absolute temperature
t	Time
T_0	Reference temperature

T_a	Temperature variation
T_{set}	Operating laser temperature
$U(\mathbf{r}, \omega)$	Voltage (acoustic-electrical analogy)
v	Velocity of a molecule
V_i	Volume of a Helmholtz resonator
V_{res}	Volume of a resonator
$x - y$	In-phase and quadrature components detection scheme
x_{diff}	Phase component of the differential photoacoustic signal
$Z(\mathbf{r}, \omega)$	Acoustic impedance

List of acronyms

CRDS	Cavity ring-down spectroscopy
CW	Continuous wave
DFB	Distributed feedback
DFG	Difference frequency generation
ECDL	External cavity diode laser
FIR	Far infrared
FMS	Frequency modulation spectroscopy
FWHM	Half width at half maximum
IM	Intensity modulation
IR	Infrared
LD	Laser diode
LDP	Low density polyethylene
MFC	Mass-flow controller
MIR	Mid infrared
NBR	Nitrile butadiene rubber
NIR	Near infrared
NR/SBR	Natural rubber/Styrene butadiene rubber
OPO	Optical parametric oscillator
PA	Photoacoustic
PAS	Photoacoustic spectroscopy
ppb	Parts-per-billion

PPLN	Periodically poled lithium niobate
ppm	Parts-per-million
QCL	Quantum cascade lasers
QEPAS	Quartz-enhanced photoacoustic spectroscopy
sccm	Standard cubic centimetres per minute
SMSR	Side mode suppression ratio
SNR	Signal-to-noise ratio
UV	Ultraviolet
VCSEL	Vertical-cavity surface-emitting laser
WM	Wavelength modulation
WMS	Wavelength modulation spectroscopy

MATTIELLO Mario

Passage Belle-Rose 5
1005 Lausanne
Phone: 079 319 15 20
E-mail: Mario.Mattiello@epfl.ch

Italian
Date of birth: 23rd February 1979
Single

EDUCATION

2003-2007 **PhD student**
Swiss Federal Institute of Technology, Lausanne (EPFL)
Nanophotonics and Metrology Laboratory
Research domain: Laser spectroscopy

1997-2002 **Degree in Electrical Engineering**
Swiss Federal Institute of Technology, Lausanne (EPFL)
Diploma project :
- Video signal coding in broadcast quality

1992-1997 **Diploma di maturità scientifica**
Liceo italiano V. Pareto, Lausanne (VD), Switzerland

PROFESSIONAL EXPERIENCE

2002-2007 **Research Assistant:**
Swiss Federal Institute of Technology, Lausanne (EPFL)
- 2002-2003: Telecommunications Laboratory
Participation to COST 266 project "Advanced infrastructure for photonic networks", concerning the analysis and implementation of routing and wavelength assignment algorithms in all-optical networks
- 2003-2007: Nanophotonics and Metrology Laboratory
Participation to GLADIS ("Gas laser analysis by infrared spectroscopy") and COST B24 ("Laboratory animals science and welfare") projects, including the development of two photoacoustic sensors for gas measurements

Teaching Assistant:
Swiss Federal Institute of Technology, Lausanne (EPFL)
- Supervision of student exercises and labs, preparation of demos for teaching lectures

LANGUAGES

Italian	Mother tongue
French	Excellent knowledge (13 years of life spent in the French-speaking part of Switzerland)
English	Fluent in both oral and written communication

COMPUTER KNOWLEDGE

Software	MS Word, MS Excel, MS Power Point, Matlab, Labview, Latex, Adobe Illustrator
Environments	Windows, UNIX

NON PROFESSIONAL ACTIVITIES

Music	Guitar in a rock band, bass, piano
Sports	Soccer
Reading	Novels, thrillers